

# RELAXATION DYNAMICS OF SOLID HELIUM-4

A Dissertation

Presented to the Faculty of the Graduate School  
of Cornell University

in Partial Fulfillment of the Requirements for the Degree of  
Doctor of Philosophy

by

Benjamin Hunt

August 2009

© 2009 Benjamin Hunt  
ALL RIGHTS RESERVED

## RELAXATION DYNAMICS OF SOLID HELIUM-4

Benjamin Hunt, Ph.D.

Cornell University 2009

The torsional oscillator (TO) experiments of Kim and Chan have been principally interpreted as providing evidence that solid helium-4 ( $^4\text{He}$ ) undergoes a transition below 100 mK to the 'supersolid' state of matter, so called because of the coexistence of superfluid behavior and other properties usually attributed to the solid phase. In this dissertation, we report on experiments that were designed to study particular aspects of the behavior of solid  $^4\text{He}$  that were difficult to reconcile with the traditional picture of superfluidity. In the first set of experiments, motivated by a number of proposals that solid  $^4\text{He}$  could contain a component that behaves as a structural glass, we study the relaxation of a torsional oscillator containing solid  $^4\text{He}$ . We show that the relaxation time to thermal perturbations in both the resonant frequency  $f$  and the dissipation  $Q^{-1}$  lengthens as  $T \rightarrow 0$ . This lengthening of the relaxation time is unexpected for superfluids, but may be evidence for the presence of a glassy component. In the second set of experiments, we employ a new technique to map efficiently the temperature and velocity dependence of the TO frequency shift and dissipation. The motivation for these experiments was the surprising result that the 'critical velocity' of the supersolid  $^4\text{He}$  was of the order of  $10 \mu\text{m/s}$ , some three to six orders of magnitude smaller than typical critical velocities in *superfluid*  $^4\text{He}$ . We find a remarkable symmetry of both  $f$  and  $Q^{-1}$  along the temperature and velocity axes, and the dependence of the TO resonant frequency and dissipation on velocity was dissimilar to any known critical velocity behavior in superfluid  $^4\text{He}$ .

This leads us to propose that the same excitations of the  $^4\text{He}$  solid generated by temperature might also be generated by agitation of the solid.

## BIOGRAPHICAL SKETCH

Ben was born in 1979. He wisely chose to attend high school in downtown Toronto, at the University of Toronto Schools, where he was miraculously not too short to play on the basketball team and in whose environs delicious food was abundant. A trip with his father to Montreal convinced him of the merits of smoked brisket over peameal bacon, and he left Toronto for the colder pastures of McGill University in 1997. He intermittently worked in the scanning probe laboratory of Peter Grütter and on anomalous X-ray pulsars with Vicky Kaspi, and had such a good time there he took an extra year to graduate. Thereafter, he spent some time in Whistler, British Columbia, but convinced that there was more to life than snowboarding five days a week, he returned to physics and has since been in residence in Ithaca, New York, happily toiling in the basement of Clark Hall in the labs of Seamus Davis. His compass is currently pointed in the direction of Cambridge, Massachusetts, where he will soon begin a postdoctoral position in the lab of Ray Ashoori at MIT.

To Mom, Dad and Jono, with love.

## ACKNOWLEDGEMENTS

First and foremost, I would like to thank my advisor, Seamus Davis, for giving me the best thing I could hope for as a graduate student: years of support and freedom to pursue what I wanted. A special thank you goes to Ethan Pratt, my primary collaborator of the last two years and my good friend, without whom I would likely have plugged far more fill lines and wasted many more hours using Origin instead of Matlab. Thank you also to Minoru Yamashita and Joan Hoffmann, the two postdocs from whom I was privileged to have learned most of what I know about low-temperature physics. Thanks to my friends and labmates, present and past: Milan Allan, Jacob Alldredge, Ming Chuang, Kazu Fujita, Vikram Gadagkar, Mohammad Hamidian, Jinho Lee, Sourin Mukhopadhyay, Andy Schmidt, and Alfred Wang. Thanks to the faculty, at Cornell and beyond, from whom I have learned much: Neil Ashcroft, Ray Ashoori, Andy Mackenzie, Jeevak Parpia, John Reppy, Keith Schwab, and Mukund Vengalattore. I would also like to acknowledge Rod Bowman, Stan Carpenter, Chris Cowulich, Nate Ellis, Jeff Koski, Stan McFall, and Bob Tillotson in the pro machine shop, as well as Eric Smith, for helping the chaotic Clark Hall operations go as smoothly as possible.

To Mom, Jono, Dad and Pam: thank you for your unending support. Chris and Sandon, thanks for encouraging me to stick with it. To my great friends and roommates: it would have been a drag without you. And finally, thank you to Sarah, for constantly helping me to remember why it was all worth it.

## CONTENTS

Biographical Sketch . . . . .	iii
Dedication . . . . .	iv
Acknowledgements . . . . .	v
Contents . . . . .	vi
List of Tables . . . . .	ix
List of Figures . . . . .	x
<b>1 Introduction to Superfluid and Solid <math>^4\text{He}</math></b>	<b>1</b>
1.1 Basic Properties of Solid $^4\text{He}$ . . . . .	2
1.2 Basic Properties of Superfluid $^4\text{He}$ . . . . .	8
1.2.1 Two-Fluid Model and Condensate Wavefunction . . . . .	9
1.2.2 Potential Flow and Quantized Vortices . . . . .	13
1.2.3 Critical Velocities . . . . .	14
1.3 Introduction to Supersolid $^4\text{He}$ . . . . .	19
1.3.1 Theoretical Precursors . . . . .	19
1.3.2 Early Searches for the Supersolid State . . . . .	22
1.3.3 Kim and Chan Effect . . . . .	25
1.3.4 Suppression of Kim and Chan Effect at High Velocities . . . . .	27
1.3.5 Blocked Annulus and Other Restricted Geometries . . . . .	28
1.3.6 Interaction of $^4\text{He}$ with Container Walls . . . . .	32
1.4 Other Recent Experiments on Solid $^4\text{He}$ . . . . .	34
1.4.1 Effect of Annealing and Sample Preparation . . . . .	35
1.4.2 Effect of $^3\text{He}$ Impurities . . . . .	37
1.4.3 Shear Modulus Stiffening . . . . .	40
1.4.4 Heat Capacity . . . . .	43
1.4.5 DC Flow . . . . .	44
1.4.6 Other Evidence of Glassy Behavior . . . . .	46
1.4.7 X-ray Diffraction and Neutron Scattering . . . . .	49
1.5 Modern Theories of the Supersolid State . . . . .	51
1.5.1 Superglass Theories . . . . .	52
1.5.2 Stress-induced Supersolidity . . . . .	56
1.5.3 Vortex Fluid . . . . .	58
<b>2 Experimental Methods</b>	<b>61</b>
2.1 Dilution Refrigerator . . . . .	61
2.2 High-Q Torsional Oscillator . . . . .	68
2.2.1 Principles . . . . .	68
2.2.2 SQUID-based Detection Scheme . . . . .	73
2.2.3 Capacitor-based Detection Scheme . . . . .	77
2.2.4 Calibration of SQUID- and Capacitor-based Sensors . . . . .	78
2.3 Pressure Measurement . . . . .	81

<b>3</b>	<b>Linear Response of the Torsional Oscillator</b>	<b>83</b>
3.1	Linear Response Theory and Rotational Susceptibility . . . . .	83
3.1.1	Susceptibility Based on Superfluid Decoupling . . . . .	87
3.1.2	Debye Susceptibility . . . . .	87
3.1.3	Glassy Susceptibility . . . . .	90
3.1.4	Viscoelastic Susceptibility . . . . .	92
3.1.5	Two-Level Systems in a Real Glassy TO . . . . .	93
3.2	Fitting to the Various Models . . . . .	95
3.2.1	Debye Susceptibility . . . . .	95
3.2.2	Glassy Susceptibility . . . . .	99
3.3	Summary and Discussion . . . . .	102
<b>4</b>	<b>Glassy Dynamics of Solid <math>^4\text{He}</math></b>	<b>106</b>
4.1	Preliminaries . . . . .	108
4.2	Experiment #1: Step-Cooling of TO- $^4\text{He}$ . . . . .	109
4.2.1	Methods . . . . .	109
4.2.2	Results . . . . .	110
4.3	Experiment #2: Abrupt Warming of TO- $^4\text{He}$ . . . . .	114
4.3.1	Methods . . . . .	116
4.3.2	Results . . . . .	116
4.3.3	Davidson-Cole Plot . . . . .	120
4.4	Discussion of the Origin of the Long-Term Relaxation . . . . .	125
4.5	Summary and Discussion . . . . .	130
<b>5</b>	<b>Unified Dynamics of Solid <math>^4\text{He}</math></b>	<b>136</b>
5.1	Methods . . . . .	138
5.2	Results . . . . .	140
5.2.1	Scaling of Velocity and Temperature . . . . .	143
5.2.2	Temperature Dependence of Critical Velocity . . . . .	153
5.2.3	Velocity Hysteresis . . . . .	155
5.3	Summary and Discussion . . . . .	156
<b>6</b>	<b>Conclusions and Outlook</b>	<b>162</b>
6.1	Summary . . . . .	162
6.2	Perspectives . . . . .	163
6.3	Future Experiments . . . . .	167
6.3.1	Frequency Dependence of Rotational Susceptibility . . . . .	168
6.3.2	Simultaneous Determination of Rotational and Shear Susceptibility . . . . .	170
6.3.3	Mass Transport through Superfluid-Solid Junctions . . . . .	172
6.4	Conclusions . . . . .	174

<b>A</b>	<b>Operation of Dilution Refrigerator in Clark A17</b>	<b>178</b>
A.1	Common Problems . . . . .	178
A.2	Starting the Dilution Refrigerator . . . . .	179
A.3	Throughput Tests of the Condenser Impedance . . . . .	181
	<b>Bibliography</b>	<b>183</b>

## LIST OF TABLES

1.1	Some characteristics of the noble gases . . . . .	3
1.2	Comparison of measurements of shear modulus measurements by Day and Beamish and by Paalanen et al. . . . .	41
1.3	Stress-induced supersolidity in the bulk and in defects. . . . .	57
2.1	Thermometers on the cryostat. . . . .	66
2.2	Output voltage ranges of VCA. . . . .	72
2.3	Calibration quantities for SQUID-based TO. . . . .	80
5.1	Parameters for unified collapse. . . . .	151
A.1	Condenser impedance at various temperatures. . . . .	182

## LIST OF FIGURES

1.1	<b>Potential, zero-point and total internal energies of the liquid and solid phases of <math>^4\text{He}</math>.</b> . . . . .	5
1.2	<b>Phase diagram of <math>^4\text{He}</math>.</b> . . . . .	7
1.3	<b>Superfluid and normal fluid fraction in liquid <math>^4\text{He}</math>.</b> . . . . .	10
1.4	<b>Critical velocity of superflow through restricted geometry.</b> . . . . .	17
1.5	<b>Measurement of period shift and (relative) amplitude of motion by Kim and Chan.</b> . . . . .	25
1.6	<b>Measurement of frequency shift and dissipation peak by our group.</b> . . . . .	26
1.7	<b>TO experiments in various container geometries.</b> . . . . .	30
1.8	<b>Effect of adding <math>^3\text{He}</math> impurities on supersolid signal.</b> . . . . .	37
1.9	<b>Memory effects from thermal cycling.</b> . . . . .	47
1.10	<b>Comparison of classical Brownian hard-sphere phases and corresponding quantum many-body phases.</b> . . . . .	54
2.1	<b>The <math>^3\text{He}</math>-<math>^4\text{He}</math> phase diagram.</b> . . . . .	62
2.2	<b>Dilution refrigerator and two solid helium experiments.</b> . . . . .	64
2.3	<b>Schematic of DR gas panel.</b> . . . . .	67
2.4	<b>Principle of operation and images of our TO.</b> . . . . .	70
2.5	<b>Feedback circuit for self-resonant drive.</b> . . . . .	71
2.6	<b>Principle of dc-SQUID-based detection schemes.</b> . . . . .	75
2.7	<b>Flux jumps in the SmCo permanent-magnet displacement sensor.</b> . . . . .	76
2.8	<b>Thermodynamic path of the helium solidification.</b> . . . . .	82
3.1	<b>Frequency shift <math>(f - f_0)/f_0</math> and dissipation shift <math>Q^{-1} - Q_\infty^{-1}</math>.</b> . . . . .	90
3.2	<b>Fits to Debye susceptibility with Arrhenius activation.</b> . . . . .	96
3.3	<b>Two methods for obtaining <math>\tau(T)</math> from the experimental data.</b> . . . . .	98
3.4	<b>Real and imaginary parts of glassy susceptibility.</b> . . . . .	101
3.5	<b>Dependence of the ratio <math> \Delta Q^{-1}  / (\Delta f^{max} / f_0)</math> on hydrostatic pressure and molar volume.</b> . . . . .	104
4.1	<b>Temperature sweep rate-dependent traces <math>f(T)</math> and <math>Q^{-1}(T)</math>.</b> . . . . .	108
4.2	<b>Step-cooling experiment.</b> . . . . .	111
4.3	<b>Results of step-cooling experiment.</b> . . . . .	113
4.4	<b>Relaxation time for frequency and dissipation.</b> . . . . .	113
4.5	<b>Fraction of relaxation traces (<math>R_f</math> and <math>R_Q</math>) relaxing at slower rate.</b> . . . . .	115
4.6	<b>Schematic of abrupt-warming experiment.</b> . . . . .	117
4.7	<b>Non-equilibrium frequency and dissipation curves from the abrupt warming experiment.</b> . . . . .	118
4.8	<b><math>\Delta Q^{-1} / (2\Delta f / f_0)</math> for time dependent data.</b> . . . . .	119
4.9	<b>Time-dependent Davidson-Cole (D-C) plot.</b> . . . . .	122

4.10	Three models of time dependence of parameters in a glassy susceptibility. . . . .	124
4.11	Thermal relaxation study of torsional oscillator. . . . .	126
4.12	Comparison of resonant frequency $f$ of the empty TO and $f$ of the TO filled with solid helium. . . . .	128
4.13	Comparison of time-dependent D-C plots for thermalization dynamics and the observed dynamics. . . . .	130
4.14	Analogy between glass/vortex fluid transitions and Brownian hard-sphere transition. . . . .	133
5.1	Typical ringdown of the solid $^4\text{He}$ -filled TO at 47 mK. . . . .	139
5.2	Resonant frequency shift and dissipation as a function of ring-down velocity. . . . .	142
5.3	Temperature-velocity phase diagrams. . . . .	144
5.4	Linecuts of frequency shift and dissipation contours. . . . .	146
5.5	Comparison of $\tau_T$ and $\tau_v$ . . . . .	150
5.6	Unified collapse of $f(v, T)$ and $Q^{-1}(v, T)$ onto a single axis. . . . .	152
5.7	$v_c(T)$ as represented by a single contour. . . . .	154
5.8	Velocity hysteresis. . . . .	156
6.1	Frequency dependence of rotational susceptibility. . . . .	169
6.2	Proposed superfluid-solid junction experiment. . . . .	173

# CHAPTER 1

## INTRODUCTION TO SUPERFLUID AND SOLID $^4\text{He}$

Helium, in both of its stable isotopic forms, is remarkable because its low temperature behavior is unique among the elements. It is the only element that becomes a superfluid at atmospheric pressure and the only element that resists forming a solid at zero temperature, even under pressures up to 25 bar and compressions of up to 16%. In the century since the first liquefaction of helium in 1908 by Kamerlingh Onnes and the discovery of superfluidity in 1938 by Kapitza [68] and (independently) by Allen and Misener [2], we have repeatedly been astonished at new phenomena not observed anywhere else in nature - at least in the version of nature that we can reproduce in the laboratory. The subject of this dissertation is perhaps the most startling of the low-temperature properties of helium discovered in the last quarter-century, namely the possibility that superfluid flow can exist within the solid. This is the “supersolid” state of matter, first proposed some forty years ago [11] yet only reported to have been manifested experimentally in the past five years in spite of a long history of experimental searches.

This introductory chapter will review the dominant role of the quantum mechanics underlying the unique low-temperature behavior of  $^4\text{He}$ , the circumstances governing the appearances of the solid and superfluid phases, and a brief history of the proposals and searches for supersolidity. It will also review the pivotal experiments of Kim and Chan [72] that reignited interest in the field, the most important experiments that have since been undertaken, some modern theories of the supersolid state most relevant to this work, and the state of the field that led us to the experiments described in this dissertation.

## 1.1 Basic Properties of Solid $^4\text{He}$

Crystalline solids are conveniently described by atoms (or groups of atoms forming a basis) localized at the sites of a periodic lattice (the Bravais lattice), which are separated by a distance  $a$ , typically a few angstroms. Many of the properties of the solid can be understood in terms of the vibrations of the atoms around their idealized positions at the sites of the lattice. In particular, this idea lends itself nicely to the idea of the melting of a crystal. When the rms amplitude of the vibrations  $\Delta r_{rms} = \sqrt{\langle \Delta r^2 \rangle}$  becomes of the order of the lattice constant  $a$ , because, for example, the temperature of the solid has been raised at fixed pressure, it hardly makes sense to talk about the localization of the atoms and equivalently one can say that the solid has melted. The well-known Lindemann criterion for classical melting says that a solid should melt when  $\Delta r_{rms}/a \simeq 0.15$ . However, X-ray scattering has shown that vibrations in solid  $^4\text{He}$ , due to the quantum-mechanical zero-point motion (ZPM) of the atoms, can be up to 25% of the lattice spacing [30].

When quantum mechanics becomes important at low temperatures, the ZPM joins the variables temperature and pressure in determining the criteria under which a solid will form. A numerical measure of the importance of the ZPM for a particular element is the (dimensionless) de Boer parameter

$$\Lambda = \frac{h}{\sigma \sqrt{m\epsilon}}.$$

The quantity  $h/\sqrt{m\epsilon}$  is the de Broglie wavelength of a free particle of energy  $\epsilon$  and  $\sigma$  is the size of the particle or the range of interaction between two particles, both within factors of order unity. For the noble gases, a good approximation to the parameters  $\epsilon$  and  $\sigma$  come from the Lennard-Jones (L-J) potential between

Table 1.1: **Some characteristics of the noble gases**

element	$\epsilon$ (K)	$\sigma$ (angstrom)	$m$ (amu)	$\Lambda$
Xe	221	4.10	131.3	0.063
Kr	171	3.60	83.8	0.101
Ar	120	3.41	39.9	0.186
Ne	35.6	2.75	20.2	0.593
$^4\text{He}$	10.2	2.56	4.0	2.68
$^3\text{He}$	10.2	2.56	3.0	3.08

Data are from [121].

two particles separated by a distance  $r$ :

$$u_{LJ}(r) = 4\epsilon \left( \left[ \frac{\sigma}{r} \right]^{12} - \left[ \frac{\sigma}{r} \right]^6 \right). \quad (1.1)$$

Table 1.1 shows for a few of the noble gases the values of  $\epsilon$  and  $\sigma$  as calculated from the L-J potential<sup>1</sup>, their masses, and the de Boer parameter for each element. The helium isotopes are the most weakly interacting of the noble gases as well as the lightest, two factors that conspire to allow the largest ZPM and greatest degree of quantum effects. A striking consequence of the large zero-point motion of helium is the fact that it does not solidify under its own vapor pressure as  $T \rightarrow 0$ ; the following argument due to F. London, involving the competition between estimated potential energies (such as Eq. 1.1) and zero-point energies of the solid and liquid phases of helium, is a clear way to see why this is so and by what criterion helium will solidify if held under elevated pressures [82, 121].

London's estimates of the potential energies of the liquid and solid phases, based on a particular interaction potential from [124], are shown in Fig. 1.1(A) as a function of the molar volume  $V$  of the respective phase. His estimate for the zero-point energy is also shown, based on a simple interpolation formula given in Chapter 20 of [121]. The stable phase will be the one for which the (molar)

<sup>1</sup>These are determined, for example, from the temperature dependence of the second virial coefficient [121].

Gibbs free energy  $G = U - TS + PV$  is a minimum; at  $T = 0$  this reduces to the condition that the enthalpy  $H = U + PV$  be a minimum. For zero external pressure,  $P = 0$ , the condition is that the internal energy  $U$  is a minimum, where both the interatomic potential and zero-point energy contribute to  $U$ . In the absence of the zero-point energy, it is clear from Fig. 1.1(A) that the stable phase at  $T = 0$  would be a solid with a molar volume of about  $11 \text{ cm}^3$ . The addition of the zero-point energy, however, modifies the internal energy curves of the solid and liquid to those shown in Fig. 1.1(B), where now the stable phase is the liquid, of molar volume  $28 \text{ cm}^3$ , indicated by a filled circle on the liquid curve.

If we now increase the external pressure, we decrease the molar volume of the liquid (solid) to a new value  $V_\ell^*$  ( $V_s^*$ ), indicated by filled squares in Fig. 1.1(B), and the total internal energy  $U$  increases accordingly. Because  $P$  is no longer equal to zero, the condition for thermodynamic equilibrium is now that the ground state enthalpy  $U + PV$  be a minimum. At the new molar volumes  $V_\ell^*$  and  $V_s^*$ , the equations of the lines tangent to the  $U(V)$  curves at these points are

$$U - V \cdot \left( \frac{\partial U}{\partial V} \right)_{V_\ell^*} = k_\ell \quad (\text{liquid})$$

$$U - V \cdot \left( \frac{\partial U}{\partial V} \right)_{V_s^*} = k_s \quad (\text{solid})$$

where  $k_\ell$  and  $k_s$  are the intercepts of the two tangent lines with the line  $V = 0$  (the y-intercepts). Since  $(\partial U / \partial V)$  is equal to  $-P$ , the condition that  $U + PV$  be minimum results in a simple criterion for which of the phases will be the stable one under pressure: *the stable phase will be the liquid for  $k_\ell < k_s$  and the solid for  $k_s < k_\ell$* . This is true for  $P = 0$ , where the tangents to the minima of the  $U(V)$  curves are flat and the liquid is the stable phase (filled circles). As we increase the pressure (and decrease the molar volume) the slopes of the

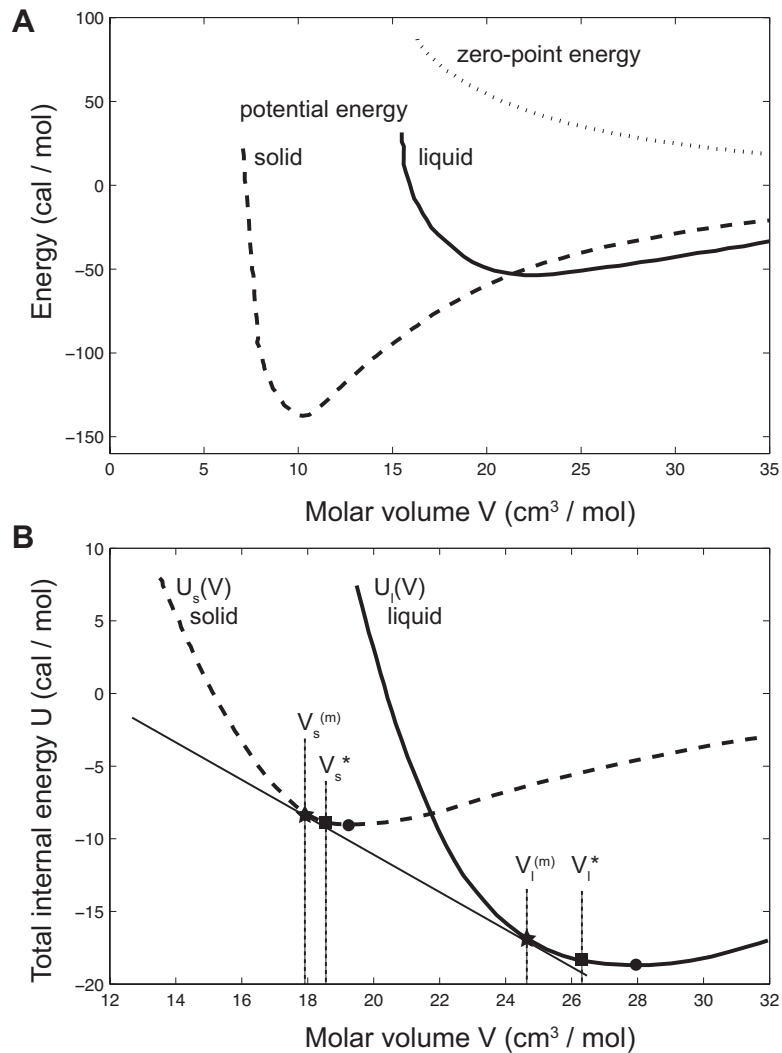


Figure 1.1: **Potential, zero-point and total internal energies of the liquid and solid phases of  $^4\text{He}$ .**

**(A)** Potential and zero-point (molar) energies as a function of the molar volume  $V$ , from a calculation by F. London. **(B)** Total internal energies  $U_\ell$  and  $U_s$  of the liquid and solid phases, obtained by adding the two energies from (A). The stable phase at  $P = 0$  is the liquid, as seen by comparing the minima of  $U_\ell$  and  $U_s$  (filled circles). Increasing the pressure decreases the molar volume of each phase through the intermediate volumes  $V_\ell^*$  and  $V_s^*$  and eventually to the values at the melting curve  $V_\ell^{(m)}$  and  $V_s^{(m)}$ , where the two curves share a common tangent (black straight line). Figure reproduced from [121].

two tangents increase, the slope of  $U_\ell(V)$  increasing more rapidly than that of  $U_s(V)$ . With increasing pressure, the molar volumes pass through  $V_\ell^*$  and  $V_s^*$  and eventually they reach the values indicated by the filled stars in Fig. 1.1(B), where the tangent lines have the same equation,  $k_\ell = k_s$ , and the solid and liquid phases are both stable. This occurs at the melting pressure, roughly 25 bar at  $T = 0$ , and the values  $V_\ell^{(m)} = 24.5 \text{ cm}^3$  and  $V_s^{(m)} = 18.0 \text{ cm}^3$ , which are close to the measured values  $23.3 \text{ cm}^3$  and  $21.2 \text{ cm}^3$ , respectively. For pressures higher than this,  $k_s < k_\ell$ , and the solid is the stable phase.

The large ZPM also means that there is a large overlap of the atomic wavefunctions centered on each lattice site and there is a corresponding larger probability of tunneling between sites. This idea will be of central importance when we discuss the motion of defects (vacancies and interstitials) within the helium crystal. It was the idea that lattice vacancies in  $^4\text{He}$ , themselves obeying Bose-Einstein statistics, could Bose condense at low enough temperatures and possess the property of superfluidity that was at the heart of the original proposals of the supersolid state. This will be discussed further in Sec. 1.3.1.

Helium-4 was first solidified in 1926 by W. H. Keesom at the famous Kamerlingh Onnes low-temperature physics laboratory at Leiden. The solid exists in three crystallographic phases, shown in the phase diagram of Fig. 1.2, forming the hcp phase for the majority of temperatures and pressures reported in this dissertation and the bcc phase for a narrow window close to the melting curve at relatively high temperatures. The third phase, the fcc phase (not shown in Fig. 1.2), occurs at extremely high pressures (above 1000 bar) and temperatures adjacent the melting curve.

Solid  $^4\text{He}$  has several other interesting properties because of the large contri-

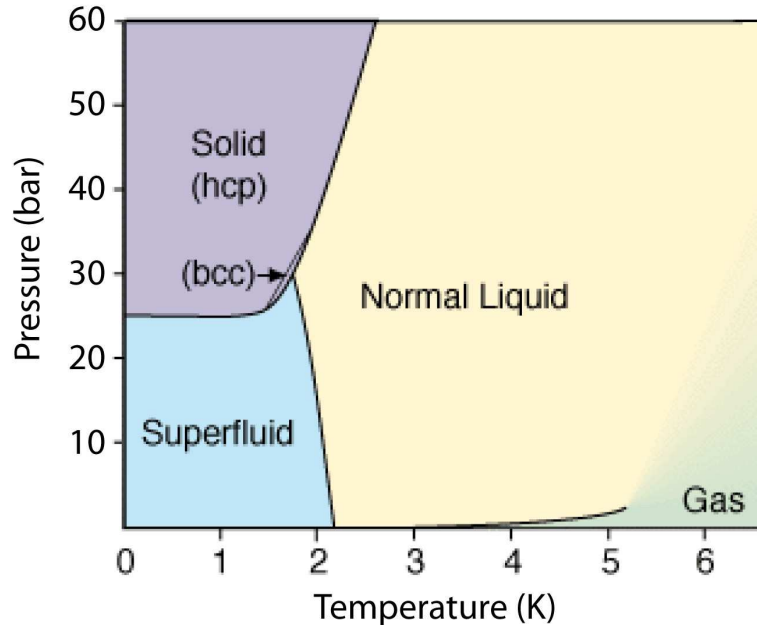


Figure 1.2: **Phase diagram of  $^4\text{He}$ .**

Two of the the three allotropic phases of solid  $^4\text{He}$  are shown (hcp and bcc); the fcc phase occurs at much higher pressures ( $>1000$  bar). The lambda temperature,  $T_\lambda(P)$ , divides the superfluid phase from the normal fluid.

tribution of the zero-point energy to its total internal energy. One is that the atoms continue to have large average vibrations around their equilibrium positions, up to 25% of the interatomic spacing [30]<sup>2</sup>. This is accompanied by a large molar volume and a very high compressibility, which makes it possible to study the solid at a range of densities. It has a correspondingly low shear modulus and low sound speeds, as well as a high thermal conductivity. Solid  $^4\text{He}$  readily forms very nice single crystals, which may be a reason that researchers were initially resistant to the idea that solid  $^4\text{He}$  could be incommensurate (i.e. that there could be a different number of atoms and lattice sites).

Liquid  $^4\text{He}$  also possesses a large zero-point energy, but its ZPE is in fact smaller than that of the solid, contrary to Fig. 1.1. Le Pair et al. suggested

<sup>2</sup>This should be compared to the classical Lindemann criterion for melting, which, as mentioned previously, says that a solid should melt when  $\Delta r_{rms}/a \simeq 0.15$

a simple reason why this might be so: the liquid is better approximated by a random close-packed (rcp) configuration, which has a coordination number of 8, in contrast to a coordination of 12 in the hcp arrangement of the solid. A  ${}^4\text{He}$  atom is correspondingly more tightly confined in the solid and has a higher ZPE. At external pressures less than 25 bar, the normal liquid undergoes a second-order phase transition to the superfluid state at a temperature  $T_\lambda$ , named for the  $\lambda$ -shape of the divergence in the specific heat. The temperature  $T_\lambda$  is weakly pressure dependent and goes from 2.17 K at zero pressure to 1.81 K where it meets the melting curve at 29 bar. The properties of this unique phase of matter will be discussed in the next section.

## 1.2 Basic Properties of Superfluid ${}^4\text{He}$

The phenomenology of superfluid  ${}^4\text{He}$  is incredibly rich and unique. Superfluid  ${}^4\text{He}$  exhibits persistent mass currents, the fountain effect, quantized vorticity, second, third and fourth sound, and the Josephson effect, among many others. Solid  ${}^4\text{He}$ , if it is indeed a supersolid, has yet to exhibit any of these phenomena. The discovery of behavior in the solid analogous to any one of these phenomena would constitute a dissertation project in its own right, and so in this introduction to superfluid  ${}^4\text{He}$  we shall be quite selective in our treatment and discuss only properties of the superfluid that have been addressed by the experiments on solid  ${}^4\text{He}$  in the last five years. For a comprehensive treatment of the properties of superfluid  ${}^4\text{He}$ , Wilks [121] or Tilley and Tilley [112] are good resources. A more basic, but more modern, treatment can be found in Annett [13].

## 1.2.1 Two-Fluid Model and Condensate Wavefunction

An appropriate place to start the discussion of superfluid  $^4\text{He}$  in this dissertation is the original torsional oscillator (TO) experiment of Andronikashvili [12]. His apparatus consisted of a stack of closely-spaced disks that could oscillate about the axis of a torsion fiber. He found that when immersed in superfluid helium, a fraction of the helium atoms were dragged along by the disks (the normal component of mass density  $\rho_n$ ) and a fraction were not (the superfluid component of mass density  $\rho_s$ )<sup>3</sup>. The result of this famous experiment is shown in Fig. 1.3. The separation of the behavior of superfluid  $^4\text{He}$  into the independent hydrodynamics of a viscous normal component and a viscosity-free superfluid component is a convenient (but not entirely accurate) description originally proposed by Tisza based on the ideas of London [83, 113], and this “two-fluid model” has inextricably informed the vocabulary of superfluid physics. It should be emphasized, however, that although the two-fluid model describes the behavior of superfluid  $^4\text{He}$  as if it were a mixture of two independent fluids, the normal and superfluid components cannot be physically separated into two independent fluids, even in principle.

For superfluid  $^4\text{He}$ , the temperature dependence of the superfluid fraction  $\rho_s/\rho$  is known experimentally in the limits  $T \rightarrow 0$  and  $T \rightarrow T_\lambda$ . It is found that

$$\rho_s(T)/\rho = 1 - AT^4$$

for  $T \rightarrow 0$ , where  $\rho$  is the total fluid density (roughly temperature independent between  $T = 0$  and  $T = T_\lambda$  [46]). The superfluid fraction approaches unity as  $T \rightarrow 0$ , and  $^4\text{He}$  is almost entirely superfluid by about 1 K. At the other extreme,

---

<sup>3</sup>This is because the spacing of the disks, about 210  $\mu\text{m}$ , is much smaller than the viscous penetration depth  $\sqrt{2\eta/\rho\omega}$  of the normal fluid for the operating frequency of the experiment (about  $[30\text{ s}]^{-1} = 0.03\text{ Hz}$ ).

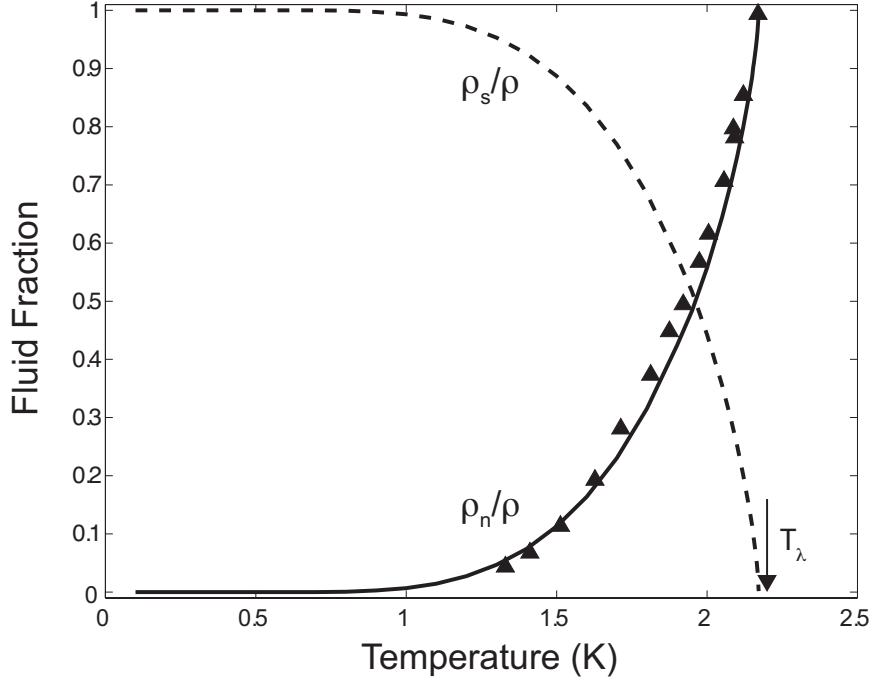


Figure 1.3: **Superfluid and normal fluid fraction in liquid  $^4\text{He}$ .** The dashed curve shows the superfluid fraction  $\rho_s/\rho$  and the solid curve shows the normal fraction  $\rho_n/\rho = 1 - \rho_s/\rho$ , reproduced from data in [46]. The triangles are the data from Andronikashvili's experiment, reproduced from [121].

as  $T \rightarrow T_\lambda$ , the superfluid fraction vanishes as a power law:

$$\rho_s(T)/\rho = \begin{cases} B (T_\lambda - T)^\nu, & T < T_\lambda \\ 0, & T > T_\lambda \end{cases}$$

where  $\nu \approx 0.67$ .

Superfluid  $^4\text{He}$  is a strongly interacting quantum fluid, so that a mean-field approach to the solution for its ground state is not appropriate, as it is for dilute (and weakly interacting) atomic gases, for which one can quite effectively employ the Gross-Pitaevskii equations. Nevertheless, superfluid  $^4\text{He}$  is believed to have a BEC in its ground state, an idea first proposed by F. London [83], and despite the fact that no exact analytic expression has been written down for the ground state of superfluid  $^4\text{He}$  due to the strong interactions, quantum Monte

Carlo simulations confirm the existence of a BEC [32].

The  $N$ -particle Hamiltonian appropriate to an interacting Bose system such as  $^4\text{He}$ , with no external potentials<sup>4</sup>, is

$$H = \sum_{i=1\dots N} -\frac{\hbar^2}{2m} \nabla_i^2 + \sum_{i,j=1\dots N, i \neq j} \frac{1}{2} u(\mathbf{r}_i - \mathbf{r}_j) \quad (1.2)$$

where  $u(r)$  is the interaction potential between two particles, given, e.g., by Eq. 1.1. Let us assume that we are at  $T = 0$  and therefore in the many-body ground state  $\Psi_0(\mathbf{r}_1, \mathbf{r}_2, \dots, \mathbf{r}_N)$ , which obeys the Schrödinger equation  $H\Psi_0 = E_0\Psi_0$ , where  $E_0$  is the ground-state energy. The bosonic nature of the particles is captured by the requirement of the proper symmetrization of  $\Psi_0$  with respect to the exchange of particle coordinates  $\mathbf{r}_i \leftrightarrow \mathbf{r}_j$ . For the non-interacting Bose gas in a volume  $V$  at  $T = 0$ , all of the  $N$  particles (of number density  $n = N/V$ ) occupy the same single-particle (zero-momentum) state  $\psi_0(\mathbf{r})$ , and we can write

$$\Psi_0(\mathbf{r}_1, \mathbf{r}_2, \dots, \mathbf{r}_N) = \psi_0(\mathbf{r}_1)\psi_0(\mathbf{r}_2) \dots \psi_0(\mathbf{r}_N) \quad (\text{non-interacting}) \quad (1.3)$$

For the interacting Bose system, this factorization cannot in general be performed. Moreover, not all of the particles, but rather a macroscopic fraction  $N_0/N$ , occupy the zero-momentum state  $\psi_0(\mathbf{r})$ . How is  $N_0$  (or the number density  $n_0 = N_0/V$ ) defined in the interacting case? Let us compare the more transparent results for the non-interacting case. It is useful to define the *one-particle density matrix*  $\rho_1$ ,

$$\rho_1(\mathbf{r}_1 - \mathbf{r}'_1) \equiv N \int \Psi_0^*(\mathbf{r}_1, \mathbf{r}_2, \dots, \mathbf{r}_N) \Psi_0(\mathbf{r}'_1, \mathbf{r}_2, \dots, \mathbf{r}_N) d\mathbf{r}_2 \dots d\mathbf{r}_N,$$

which is a correlation function of the many-body wavefunction obtained by averaging over all particle coordinates save  $\mathbf{r}_1$  and  $\mathbf{r}'_1$ . For the non-interacting case,

---

<sup>4</sup>It is, of course, the presence of external potentials that allows coupling between  $^4\text{He}$  and the walls of its container and therefore the transmission of torques from the torsional oscillator to the interior of the  $^4\text{He}$  sample. An example of such an interaction is given by Eq. 1.15.

with  $\Psi_0$  given by Eq. 1.3, the one-particle density matrix reduces to

$$\rho_1(\mathbf{r} - \mathbf{r}') = N\psi_0(\mathbf{r})\psi_0(\mathbf{r}') \quad (\text{non - interacting}) \quad (1.4)$$

(dropping the unnecessary particle label). Since for the non-interacting case  $\psi_0(\mathbf{r})$  is in general a plane-wave state [i.e.  $\psi_0(\mathbf{r}) = (1/\sqrt{V}) \exp(i\mathbf{k} \cdot \mathbf{r})$ ], this reduces to

$$\rho_1(\mathbf{r} - \mathbf{r}') = N/V = n \quad (\text{non - interacting})$$

for the zero-momentum state  $\mathbf{k} = 0$ . For the interacting system, this motivates the definition of the *condensate density*  $n_0$ ,

$$n_0 \equiv \lim_{|\mathbf{r}-\mathbf{r}'| \rightarrow \infty} \rho_1(\mathbf{r} - \mathbf{r}'),$$

and by analogy with Eq. 1.4, we define the *condensate wavefunction*  $\psi_0(\mathbf{r})$  via the one-particle density matrix  $\rho_1$ ,

$$\rho_1(\mathbf{r} - \mathbf{r}') \sim \psi_0^*(\mathbf{r})\psi_0(\mathbf{r}'), \quad (1.5)$$

with the normalization  $|\psi_0|^2 = n_0$ . The condensate wavefunction is the single-particle state shared by the  $N_0$  particles. Another way to write the condensate wavefunction is in terms of its phase, which as we will see in the next section determines the dynamical properties of the superfluid:

$$\psi_0(\mathbf{r}) = \sqrt{n_0} e^{i\phi(\mathbf{r})} \quad (1.6)$$

Because of the interactions, in liquid  $^4\text{He}$  the condensate density  $n_0 \approx 0.1n$  but the superfluid density  $n_s = n$ ; even though just 10% of the particles are condensed into the zero-momentum state given by Eq. 1.6, *all* of the particles participate in the superflow at  $T = 0$ . This is a subtle point that I will not address in detail; the interested reader should consult [13]. Whether  $n_0 = n_s = \rho_s/m$  (non-interacting Bose gas) or  $n_0 \ll n_s = \rho_s/m$  (strongly-interacting liquid  $^4\text{He}$ ),

the phenomena of Secs. 1.2.2 and 1.2.3 are qualitatively similar, and so I will take the normalization constant of Eq. 1.6  $\sqrt{n_0} \rightarrow \sqrt{n_s}$  for the discussion in the following sections. This form of the macroscopic wavefunction for superfluid  ${}^4\text{He}$ ,  $\psi_0(\mathbf{r}) = \sqrt{n_s}e^{i\phi(\mathbf{r})}$ , had originally been proposed by London in 1954 [82].

It should be noted that for *supersolid*  ${}^4\text{He}$ , whose supercomponent may be comprised of a Bose-condensed dilute gas of vacancies, a Gross-Pitaevskii treatment may be appropriate [9] and the results of this section for the non-interacting (or weakly interacting) Bose gas might be applicable.

## 1.2.2 Potential Flow and Quantized Vortices

If one uses the quantum-mechanical expression for the probability current density  $\mathbf{J} = (\hbar/2mi)(\psi_0^* \nabla \psi_0 - \psi_0 \nabla \psi_0^*)$  and for the superfluid velocity  $\mathbf{v}_s = (m/\rho_s)\mathbf{J}$ , one finds that the velocity is proportional to the gradient of the phase  $\phi$

$$\mathbf{v}_s = \frac{\hbar}{m} \nabla \phi. \quad (1.7)$$

This is known as potential flow because the velocity can be written as the gradient of a velocity potential  $\hbar\phi/m$ . It is also known as irrotational or curl-free flow because  $\nabla \times \mathbf{v}_s = 0$ . This fact has immediate consequences for the types of flow possible for a superfluid contained in torsional oscillators of various geometries (see, e.g., Section 1.3.5). A consequence of Eq. 1.7 (and the requirement of single-valuedness of 1.6) is that the *circulation*  $\kappa$ , defined as the line integral of the velocity around any closed contour, is quantized in units of  $\kappa_0 \equiv 2\pi\hbar/m$ , viz.,

$$\kappa \equiv \oint \mathbf{v}_s \cdot d\mathbf{l} = \frac{2\pi\hbar}{m}n, \quad |n| = 0, 1, 2, \dots \quad (1.8)$$

This means, for example, in an annular flow geometry of cross-sectional area  $\pi r^2$  and radius  $R$  ( $r \ll R$ ), the superflow velocity is limited to the quantized values  $v_s = (\kappa_0/2\pi R) n$ . For  ${}^4\text{He}$ ,  $\kappa_0$  is about  $10^{-7} \text{ m}^2/\text{s}$ .

### 1.2.3 Critical Velocities

Superfluids cannot undergo superflow at arbitrarily high velocities. For a superfluid confined to flow in a channel, there will be some minimum relative velocity of the walls of the container and the superflow at which it becomes possible to create elementary long-wavelength excitations of the fluid (for example, by scattering from roughness on the surface of the channel<sup>5</sup>). In the laboratory frame, a defect on the channel walls would appear as a perturbation  $V(\mathbf{r})$  in the Hamiltonian governing the behavior of the fluid helium (Eq. 1.2). In the rest frame of the fluid, it would appear as a time-dependent perturbation  $V(\mathbf{r}' - \mathbf{v}t)$ , where  $\mathbf{r}'$  is the coordinate in the superfluid rest frame. In order for the particles in the superfluid to be scattered into an excited state having momentum  $\mathbf{p}$  and energy  $\epsilon = \epsilon(\mathbf{p})$ , energy conservation requires that

$$\epsilon_f = \epsilon_i - (\mathbf{p}_i - \mathbf{p}_f) \cdot \mathbf{v}, \quad (1.9)$$

where  $i$  refers to the initial energy (and momentum) of the condensate,  $f$  to the final energy (and momentum) of the elementary excitation, and  $\mathbf{v}$  to the relative velocity between the wall and the condensate. Since  $\epsilon_i = 0$  and  $\mathbf{p}_i = 0$  for the condensate, this equation reduces to  $\epsilon(p) = \mathbf{p} \cdot \mathbf{v}$ . Landau introduced the idea of a critical velocity as the minimum velocity for which Eq. 1.9 is satisfied, that

---

<sup>5</sup>The scale of the roughness  $\ell$  should be about the de Broglie wavelength  $h/mv$ . For a  ${}^4\text{He}$  atom travelling at  $v = 1 - 10 \text{ m/s}$ , this comes out to be  $\ell = \kappa_0/v \sim 10 - 100 \text{ nm}$ .

is, the velocity  $v_c$  for which

$$v_c = \left[ \frac{\epsilon(\mathbf{p})}{|\mathbf{p}|} \right]_{min} . \quad (1.10)$$

He recognized that the experimental fact of superfluidity implied that the dispersion  $\epsilon(\mathbf{p})$  of the elementary excitations of the superfluid had to have a unique form. In normal flow, for which the excitations are those of single atoms and have the free-particle form  $\epsilon(\mathbf{p}) = p^2/2m$ , the Landau criterion is trivially satisfied for  $v_c = 0$ ; it is always possible to degrade the flow by creating excitations of single atoms. In superfluid  $^4\text{He}$ , however, the spectrum of elementary excitations is very different than this simple parabolic dispersion. It is usually divided into two branches, the *phonon branch*, valid close to  $p \rightarrow 0$ , where

$$\epsilon(\mathbf{p}) = c_1|\mathbf{p}|$$

and the *roton branch*, which has the empirical form

$$\epsilon(\mathbf{p}) = \Delta + \frac{(p - p_0)^2}{2\mu}$$

for momenta  $p \approx p_0$ . According to the Landau criterion (Eq. 1.10) the critical velocity for phonon creation is  $c_1$ , the velocity of first sound, and is 239 m/s. For roton creation the Landau criterion implies that it must be given by  $\Delta/p_0$  and is necessarily somewhat lower than  $c_1$ ; Landau deduced that it was 58 m/s [77].

In practice, observed values of the critical velocity in superfluid flow in channels and through apertures are much lower than this figure. In 1955, Feynman suggested that the onset of the creation of vortices might be responsible for the lower observed critical velocities. He made use of the Landau criterion but employed the appropriate parameters for a quantized vortex ring and predicted

that the critical velocity would be

$$v_c = \frac{\kappa_0}{2\pi d} \ln \left( \frac{d}{a_0} \right), \quad (1.11)$$

where  $d$  is the width of the channel and  $a_0 \sim 0.15$  nm is the size of the vortex core. This *temperature-independent, low-velocity* expression for the critical velocity is found to work well for flow in channels having widths larger than a few microns. For a channel diameter of  $100 \mu\text{m}$ , Eq. 1.11 predicts a critical velocity of about 2 mm/s, which is within a factor of 2 of the reported value [116].

Vinen elaborated on the process by which vortices could be produced. He suggested that vortices would be nucleated preferentially on sharp features of the walls of a channel, where the local superfluid velocity would be high, and could be pulled away from the wall by the flow itself. The subsequent movement of the vortex across the streamlines of the superfluid flow decrements the flow velocity by an amount  $\Delta v = \kappa_0/\ell$  and reduces the kinetic energy of the superflow ( $\ell$  is the effective hydrodynamic length of the channel). This is the mechanism of dissipation by “phase slippage” due to Anderson [6]. The rate  $\Gamma$  at which vortices are pulled away from the wall of the channel is given by a thermal activation law with a velocity-dependent energy barrier:  $\Gamma \propto \exp[-E_0(1 - v/v_0)/k_B T]$ , which can be shown to be consistent with a *temperature-dependent* expression for the critical velocity in this *high-velocity regime* [116]:

$$v_c = v_{c0} \left( 1 - \frac{T}{T_0} \right). \quad (1.12)$$

The parameters  $v_{c0}$  and  $T_0$  depend on the geometry of the channel or aperture, but the linear dependence is universal. Typical critical velocities in this regime are in the 1 m/s to 10 m/s range, and the parameter  $T_0$  tends to be higher than  $T_\lambda$  (in the case of  $^4\text{He}$ ) or  $T_c$  (in the case of  $^3\text{He}$ ), an experimental fact which is

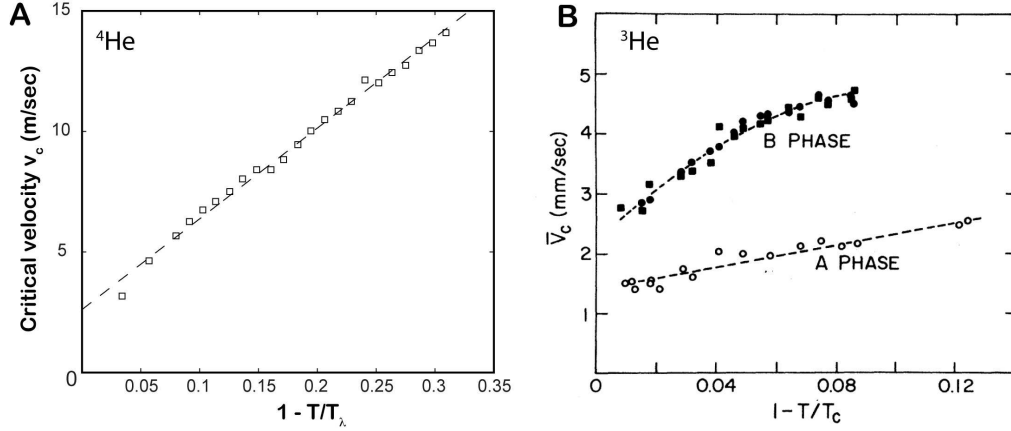


Figure 1.4: **Critical velocity of superflow through restricted geometry.** (A) Critical velocity of superfluid  $^4\text{He}$  flow through an aperture array. (B) Critical velocity of superfluid  $^3\text{He}$  flow through an  $18\ \mu\text{m}$ -wide circular aperture, as measured with a torsional oscillator. The flow of superfluid  $^4\text{He}$  was also measured with the TO and no evidence of a critical velocity was found up to  $100\ \text{cm/s}$ , the limit of the apparatus. Note that the vertical scale of (A) is roughly  $10^3$  times larger than that of (B).

manifested as a non-zero intercept in Fig. 1.4. In the  $T \rightarrow 0$  limit, the quantum tunneling of vortices becomes a significant mechanism and the low-temperature critical velocities are reduced from the values predicted by Eq. 1.12 [41, 116].

A measurement of the critical velocity of superflow through a parallel array of  $\sim 7000$  tiny apertures is shown in Fig. 1.4(A). The apertures are approximately  $15\ \text{nm} \times 15\ \text{nm}$  and form a regularly spaced array with a center-to-center distance of  $3000\ \text{nm}$ . These measurements are at relatively low frequencies, on the order of  $100\ \text{Hz}$  and less, and were carried out at Cornell by the author [64]. Independent measurements indicate that the mechanism for the destruction of superflow is phase slippage of the type discussed above. Fig. 1.4(B) shows the measurements of the temperature dependence of superfluid  $^3\text{He}$  by Parpia and Reppy [90]. These researchers used a torsional oscillator with an annular cavity for the helium flow (of cross-sectional area  $A = 1.25\ \text{mm} \times 0.25\ \text{mm}$ ), very similar to the oscillator used for the experiments in this dissertation (see Sec. 2.2).

They interrupted the tangential flow path with a partition containing a single  $18 \mu\text{m}$ -diameter aperture and measured the velocity of the oscillator at which the resonant frequency  $f$  and dissipation  $Q^{-1}$  began to deviate from their low temperature values  $f_0$  and  $Q_0^{-1}$ . They also measured the flow of superfluid  $^4\text{He}$  through the aperture and found no evidence of increased dissipation up to  $100 \text{ cm/s}$ . It is notable that the critical velocities in superfluid  $^3\text{He}$  and  $^4\text{He}$  are quite different; the higher value of the critical velocities in superfluid  $^4\text{He}$  are also confirmed by many other measurements (e.g. [61]). As we shall see, the critical velocity for proposed *supersolid* flow is reported to be of the order of  $10 \mu\text{m/s}$ , three to six orders of magnitude smaller than any measured critical velocities reported in the literature.

Vinen's description of the vortex nucleation process necessarily considered how the superflow was modified at the interface of the superfluid and the walls of its container. In the same vein, an important consideration in the TO experiments is the boundary condition between the moving container and the superfluid (or solid) contained within it, which can have a significant effect on the apparent superfluid decoupling from the container. Even for an incompressible superfluid undergoing potential flow, the hydrodynamic impedance presented by the flow path can directly couple the superfluid to the walls of the container and reduce the apparent superfluid fraction as would be measured by a shift of the TO resonant frequency. For example, in the TO experiment on superfluid  $^3\text{He}$  and  $^4\text{He}$  of Parpia and Reppy, in which the annular flow path of the superfluid is interrupted by a partition containing an  $18 \mu\text{m}$ -diameter aperture, the fraction  $x$  of the superfluid directly coupled to the TO because of the impedance of the aperture is given by ([90], endnote 2)

$$\frac{1-x}{x} = \frac{4\pi Rr}{A},$$

where  $R$  is the radius of the annulus,  $A$  is the cross-sectional area (given above), and  $r$  is the radius of the aperture ( $9 \mu\text{m}$ ). For this geometry, the fraction  $x$  of superfluid coupled to the TO was found to be 27%. A more extreme example of the effect of the boundary condition on potential flow is the “blocked annulus” experiment, described in Sec. 1.3.5. The boundary condition between the helium and the walls of the container is an important consideration for the TO experiments on *solid*  $^4\text{He}$  as well. How do we know that the supersolid signal cannot be explained simply by the solid slipping relative to the walls of the container, or perhaps a more sophisticated version of the same basic idea, such as crystalline grains slipping relative to one another and mimicking a superfluid decoupling? Section 1.3.5 will consider the role of modifying the solid  $^4\text{He}$ -container boundary condition by freezing the helium in a highly disordered geometry consisting of a large number of nanoscale pores, which increases the contact surface-to-volume ratio by roughly two to three orders of magnitude relative to an open container of the same dimensions. Section 1.3.6 will briefly address the microscopic interaction of the helium and the the inner surface of the walls of the TO container.

## 1.3 Introduction to Supersolid $^4\text{He}$

### 1.3.1 Theoretical Precursors

Starting in earnest around 1969-1970, researchers began to consider the possibility of ‘supersolidity’, whose precise definition is still a matter of important debate, but signifies, roughly, the coexistence of superfluid and solid behavior.

One definition of a solid is a substance possessing a shear modulus, a condition that is certainly satisfied by all of the samples studied in this dissertation and by the other experimenters in this field. Another definition, which by contrast may not be satisfied by a large class of samples of solid helium studied in this field, is a substance exhibiting long-ranged order in the diagonal components of its single-particle density matrix. A supersolid, using the latter definition of a solid, would then be a material exhibiting both diagonal long-ranged order (DLRO) and off-diagonal long-ranged order (ODLRO).

In 1969, Andreev and Lifshitz presented a physical argument for the mechanism of superfluidity in a crystalline solid [11]. They considered the behavior of defects, such as vacancies, in a quantum solid having large zero-point motion of its atoms. They reasoned that if a quantum crystal contained vacancies down to  $T = 0$  [zero-point vacancies (ZPVs)] that because of a higher probability of tunneling from site to site, the ZPVs could move practically freely through the crystal instead of their usual diffusive behavior when treated as classical, localized objects. Moreover, if the crystal lattice consisted of bosons, the vacancies themselves would obey Bose-Einstein statistics and could Bose condense at a sufficiently low temperature. Andreev and Lifshitz's idea about a possible mechanism of supersolidity has become the standard building-block for many contemporary ideas about the nature of the low-temperature state of solid  $^4\text{He}$ .

Chester, working from an earlier proof by Reatto [98], proved that a particular class of wavefunctions, which describe  $N$  interacting bosons, had a Bose-Einstein condensate (BEC) [34]. This class of wavefunctions was first written down by Jastrow [67] and has the form

$$\Psi_N \propto \exp \left[ -\frac{1}{2} \sum_{i \neq j} u(r_{ij}) \right], \quad (1.13)$$

where  $u(r)$  is (proportional to) the pair potential between two bosons separated by  $r$ . The theorem was proved for the following conditions:  $u(r)$  having a hard-core repulsion for  $r < a$ ,  $u(r) > 0$  for  $a < r < b$  and  $u(r)$  falling off faster than  $r^{-(3+\epsilon)}$  for  $r > b$ . It was also proved for the case  $u(r) \rightarrow u(r) + \chi(r)$ , where  $\chi$  is a function that accounts for the zero-point motion of the long-wavelength density waves. Since the probability distribution  $P_N = |\Psi_N|^2$  is identical to the classical Gibbs distribution for  $N$  particles at a temperature  $T_{eff}$  interacting via a pair potential  $\phi$  (if one identifies  $u$  with  $\phi/k_B T_{eff}$ ), Chester then conjectured that the states represented by Eq. 1.13 might also exhibit crystalline ordering at sufficiently high densities, for a wide class of potentials represented by  $\phi$  or  $u$  (e.g. Eq. 1.1). This was the essential realization of Chester's work; an earlier proof of Onsager and Penrose had held that a state with crystalline order could *not* have a Bose-Einstein condensate [91], but Chester pointed out that their proof failed if one or more of their assumptions were discarded. The most significant of these was their assumption that each site was occupied by a particle (i.e.  $N_{particles} = N_{sites}$ ), and in particular, if vacancies were included in the wavefunction, so that  $N_{particles} < N_{sites}$ , then a BEC could exist.

Leggett discussed the implications of rotating a solid with a BEC in analogy to the rotation of superfluid in a container [78]. He thus made a connection between the ideas of Chester and of Andreev and Lifshitz and what one might observe in the laboratory. He coined the term "non-classical rotational inertia" (NCRI) to describe the effect of the superfluid component decoupling from the rotating container (and normal fluid) and reducing the moment of inertia from its classical value by a factor  $\rho_s/\rho$ , the superfluid fraction. He made the remarkable prediction that whereas for the superfluid  $\rho_s/\rho \rightarrow 1$  as  $T \rightarrow 0$  (Fig. 1.3), for the solid with a BEC the superfluid fraction would be much less than unity,

even in the zero-temperature limit (his prediction is that  $\rho_s/\rho \lesssim 10^{-4}$ ). He also proposed that the presence of vacancies might not be a necessary condition for NCRI; exchange processes in a *commensurate* solid might give rise to a NCRI fraction of the order of  $10^{-4}$ .

The main problem with the Andreev-Lifshitz-Chester idea of the mechanism for supersolidity is that the energy for creation of (localized) vacancies  $\Delta_v$  is of the order of 10 K (Table 1.1) and so there would be a negligibly small probability of having vacancies at low temperatures; the low-temperature crystal would be commensurate and therefore not supersolid. We know now that the signature of the proposed supersolid has its onset at roughly 100 mK, where the probability of having thermally-generated vacancies is of the order of  $e^{-100}$ , and so several researchers have explored other mechanisms by which there could be gapless creation of vacancies in the helium solid (see Sec. 1.5.2).

### 1.3.2 Early Searches for the Supersolid State

These fascinating new ideas about the potential for a new phase of matter set off a flurry of experimental work from the 1970s right through to the mid-1990s. To discuss all of the results is beyond the scope of this dissertation (for a review, see [84] or [57]), but I will discuss one of note because it used high-Q torsional oscillators (TOs) to study solid helium at low temperatures. The torsional oscillator is an instrument that has been used with great success to study the superfluid transition in both  $^3\text{He}$  and  $^4\text{He}$  and many major developments were made at Cornell, primarily in the group of John Reppy. The TO consists of an inertial bob of moment  $I_{TO}$  plus a torsion rod providing a restoring force. The basic

idea is that the high-Q TO is an extremely sensitive probe of changes in the moment of inertia of the helium fluid  $I_{He}$  contained within the TO, which itself has a moment of inertia  $I_{TO}$ . The resonant frequency of the TO is

$$f = \frac{1}{2\pi} \sqrt{\frac{K}{I}}$$

and  $I = I_{TO} + I_{He}$  ( $K$  is the torsional spring constant providing the restoring force). If a fraction of the helium  $\rho_s/\rho$  decouples from the oscillator,  $I_{He}$  will decrease by a factor  $1 - \rho_s/\rho$ , the rigid-body moment of inertia  $I = I_{TO} + I_{He}$  will also decrease, and the resonant frequency of the TO-helium system will increase. This is, of course, the correct interpretation in many ground-breaking TO studies of helium, including the original measurement of the superfluid density by Andronikashvili and the first experimental verification of the Kosterlitz-Thouless transition by Bishop and Reppy [25]. It was natural, therefore, to see if an analogous effect occurred when solid helium was contained inside the TO.

In 1981, Bishop, Paalanen and Reppy used a TO with a spherical cavity to study solid hcp  $^4\text{He}$  [24]. They observed no abrupt change in the resonant period of the TO and concluded that if a supersolid phase did exist, that it would have a superfluid fraction less than  $5 \times 10^{-6}$ , a critical velocity less than  $5 \mu\text{m/s}$ , or a transition temperature less than 25 mK. We know now that the magnitude of the “supersolid” signal as reported by Kim and Chan [72] depends sensitively on annealing (e.g. the solid in [102] was held at a temperature 0.78 K below the melting temperature  $T_m = 2.35 \text{ K}$  for 12 h) and on the concentration of  $^3\text{He}$  impurities, and the methods and materials that they chose for their study (well-annealed crystals with a relatively high  $^3\text{He}$  concentration) constituted the likely explanation for why they did not observe the Kim and Chan signal. They did, however, find other changes in the resonant frequency as a function of temperature that they could attribute to other phenomena; one change was due to

an overall density increase in the helium solid because of  $^3\text{He}$ - $^4\text{He}$  phase separation and a second was due to a change in the shear modulus of the crystal in the torsion rod because of the enhanced motion of dislocations. This latter effect was studied in greater detail by Paalanen, Bishop and Dail [88].

In [88], Paalanen et al. used a cylindrical TO, essentially a torsion rod without the inertia bob, to study the shear modulus and internal friction of solid helium in the same temperature regime. They were able to deduce the shear modulus from empty- and full-cell measurements of the period, and the internal friction (dissipation) from the inverse quality factor ( $Q^{-1}$ ) of the oscillator. For a series of experiments, they found that the shear modulus increased (by as much as 40%) as the temperature was lowered and was accompanied by a broad peak in  $Q^{-1}$  centered at a temperature  $T^*$ , where the  $T^*$  was in the range 0.2-2 K and increased with decreasing maximum strain amplitude  $\epsilon$  (a quantity that was roughly fixed for each experiment). They concluded that the low temperature increase in the shear modulus was a natural consequence of the freezing of dislocation lines, which can be pinned by  $^3\text{He}$  impurities. This may seem surprising, given the light mass and high diffusivity of  $^3\text{He}$  impurities in solid  $^4\text{He}$  (even at low temperatures), but a pinning  $^3\text{He}$  atom has a lower elastic energy than in the bulk and can be well localized [66]. For more discussion on this issue, see Sec. 1.4.2.

I have included this last example in some detail particularly because it is not a widely cited paper in the contemporary discussion of solid helium, but is the first paper I know of that reports anomalous low temperature phenomena in solid  $^4\text{He}$  of the type discussed in this dissertation. The paper hints at the complications to come - in a torsional oscillator, the increase in the resonant

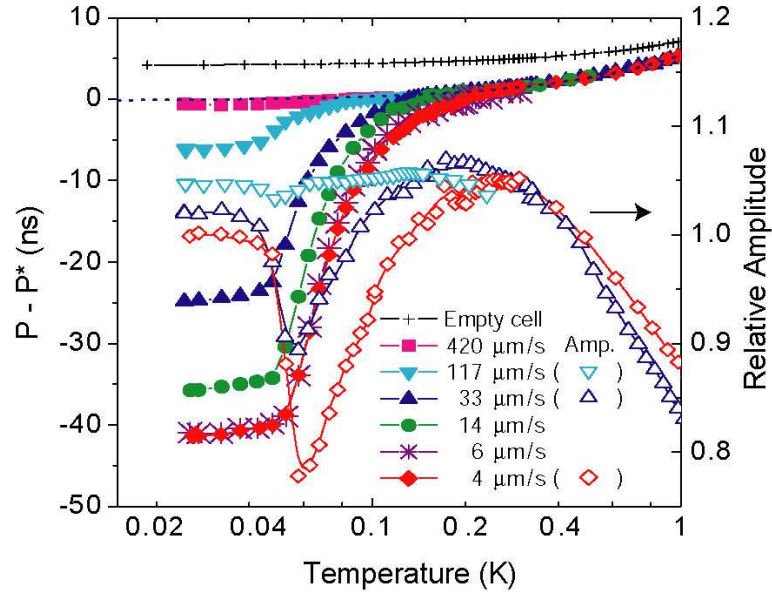


Figure 1.5: Measurement of period shift and (relative) amplitude of motion by Kim and Chan.

frequency is often indicative of the onset of superfluidity, but depending on whether the dominant effect of the shear stiffening of the  $^4\text{He}$  is in the torsion rod or in the bob, the resonant frequency can increase or decrease.

### 1.3.3 Kim and Chan Effect

In 2004 Kim and Chan presented the first evidence of the anomalous low temperature behavior of solid  $^4\text{He}$  [72], often called the “supersolid signal”, that renewed interest in the study of solid  $^4\text{He}$ . The central piece of evidence was the decrease in the resonant period (or increase in resonant frequency) of a torsional oscillator (TO) containing solid  $^4\text{He}$  when the TO was cooled below roughly 100 mK. In the context of superfluidity, this effect has a natural interpretation as the decoupling of a fraction of the mass of the helium entrained by its container, that is, the superfluid fraction.

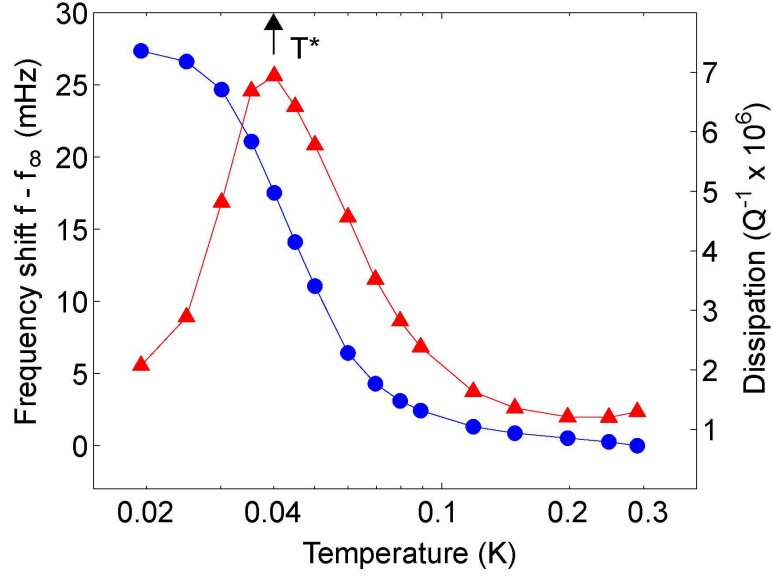


Figure 1.6: **Measurement of frequency shift and dissipation peak by our group.**

The temperature  $T^*$  at which the dissipation is maximum is indicated with a black arrow and is about 40 mK for this sample. This figure should be viewed as the inverse of Fig. 1.5 since the period shift is the inverse of the frequency shift and the minimum in the amplitude (proportional to  $Q$ ) is the inverse of the dissipation  $Q^{-1}$ .

The apparent superfluid fraction deduced from the frequency shift was anointed the “non-classical rotational inertia fraction” (NCRIf), a term originally due to Leggett [78]. Its definition is simply the change in the moment of inertia of the helium (due to decoupling) divided by the change in the moment of inertia of the TO due to adding the helium, and for small changes is just

$$NCRIf = \frac{P_{filled}(T \rightarrow \infty) - P_{filled}(T \rightarrow 0)}{P_{filled}(T \rightarrow \infty) - P_{empty}(T \rightarrow \infty)}. \quad (1.14)$$

Here,  $\infty$  is defined to be a temperature larger than the onset of the ‘supersolid’ signal, i.e.  $T \gtrsim 0.5$  K in Figs. 1.5 and 1.6. The NCRIf, or superfluid fraction, was found to be very small; at the time the fraction was of the order of 1% and today the 8 or so groups that have reproduced this result have found a range of fractions from the very small (0.01%) to as high as 20% in certain geometries and

with certain sample preparation. All of the groups also find that the frequency shift is accompanied by a peak in the dissipation  $Q^{-1}(T)$  of the TO-helium system, centered at a temperature  $T^*$  that coincides with the maximum change in the slope of the  $f(T)$ . An example of a typical frequency shift and dissipation peak that we measure in our laboratory is shown in Fig. 1.6.

Although the existence of a dissipation peak has been known since the early days of this field [71], its existence has not been satisfactorily explained in the context of superfluidity (with the exception of the vortex fluid model of Anderson, to be discussed in Sec. 1.5.3). For example, in the two-dimensional superfluid (Kosterlitz-Thouless) transition, the frequency shift that is the signature of the transition is accompanied by a dissipation peak, which is understood to be a consequence of the diffusive motion of two-dimensional vortices [25]; in the three-dimensional superfluid transition, including that in a highly disordered network of pores (Vycor glass) [21], the dissipation peak is absent. Explaining the nature of the dissipation peak is also one of the central aims of this dissertation.

The first two Kim and Chan papers presented two other effects that have been interpreted as evidence of supersolid behavior. These are also particularly important to the conclusions of this dissertation and merit extended discussions.

### **1.3.4 Suppression of Kim and Chan Effect at High Velocities**

In their very first paper on the subject [72], Kim and Chan presented data showing that the supersolid signal could be suppressed by increasing the velocity of

the oscillator above a critical value, which was about  $10 \mu\text{m/s}$ . The signal then continued to be suppressed for about 2 decades of increase in the velocity until it was completely extinguished. This value of  $10 \mu\text{m/s}$  was interpreted as the critical velocity  $v_c$  of flow the supercomponent and it was suggested that the mechanism for destruction of the superflow might be the creation of vortices, since in the geometry of their experiment (a thin annular cavity with a radius of  $R = 5 \text{ mm}$ ) the circulation quantization condition  $2\pi Rv_s = n\kappa_0$  (see Eq. 1.8) implied a superflow velocity of  $v_s = 3.6 \mu\text{m/s}$  for the appearance of one quantum of circulation ( $n = 1$ ). Thus, the suppression of the supersolid signal beginning at  $10 \mu\text{m/s}$  was associated with the appearance of a few quanta of circulation. However, in a later paper, Clark, Maynard and Chan note that for one sample they studied the observed critical velocity is about 3 or 4 times lower than can be explained by the appearance of a single vortex [35]. The interpretation in terms of vortex creation is also surprising in light of the mechanism for vortex nucleation in *superfluid*  $^4\text{He}$ . A number of experiments measuring the critical velocity for vortex creation [41, 64], including one experiment using a torsional oscillator [90], find that the  $v_c$  of superfluid  $^4\text{He}$  is at least  $100 \text{ cm/s}$ , and more typically in the range  $1 \text{ m/s}$  to  $10 \text{ m/s}$  (see Fig. 1.4), some six or seven orders of magnitude higher than measured for supersolid  $^4\text{He}$ .

### 1.3.5 Blocked Annulus and Other Restricted Geometries

The blocked annulus experiment was an ingenious control experiment first described in [71]. In that paper, Kim and Chan measured the resonant frequency of a helium-filled TO with an annular cavity geometry. They then repeated the experiment with a second torsional oscillator with similar dimensions to the

first, but with one significant change: the usual 'O' shaped path for the helium flow in an annular geometry was interrupted by a barrier, leaving the flow path in a 'C' shape instead<sup>6</sup>. What they observed was that the frequency shift found in the 'O' geometry was nearly completely extinguished in the 'C' geometry. In particular, it was reduced by about 98.5% of the expected block-free value. This near-total elimination of the frequency shift is hard to imagine if the explanation for the frequency shift in the 'O' geometry is simply due to the helium not following the acceleration of the TO (because of its finite shear modulus). If the frequency shift in the open channel were due only to the finite shear modulus of the helium, blocking the channel would only have a *local* effect, changing the displacement field and stress tensor of the helium solid in the vicinity of the block, and the reduction in frequency shift due to the block would be much less than 98.5 %.

The nature of the remaining 1.5% of the frequency shift that was not extinguished by the block is still a matter of debate. Superfluids undergo potential flow (Eq. 1.7) and so in any cavity of finite size there are irrotational flow paths that the superfluid can take, even in the case that these flow paths do not completely enclose the rotation axis of the TO. An example of such a flow path is shown in Fig. 1.7(A); a calculation at Cornell by Erich Mueller found that the apparent decoupling due to the irrotational flow in Fig. 1.7(A) was about 0.8% [71]. A repeat of the blocked annulus experiment with liquid helium found that, far from 100% decoupling at the lowest temperature, the observed fraction was closer to 1.7% for the irrotational flow of *superfluid* <sup>4</sup>He. Within the signal-to-noise limit of their measurement, no dissipation peak was found to accompany

---

<sup>6</sup>The dimensions of the TO with the block were larger than those of the barrier-free TO, which makes direct comparison somewhat difficult. However, a repeat of this blocked annulus experiment with a TO in which the flow path could be reversibly blocked and unblocked came to the same conclusions [103] (cont'd from previous page).

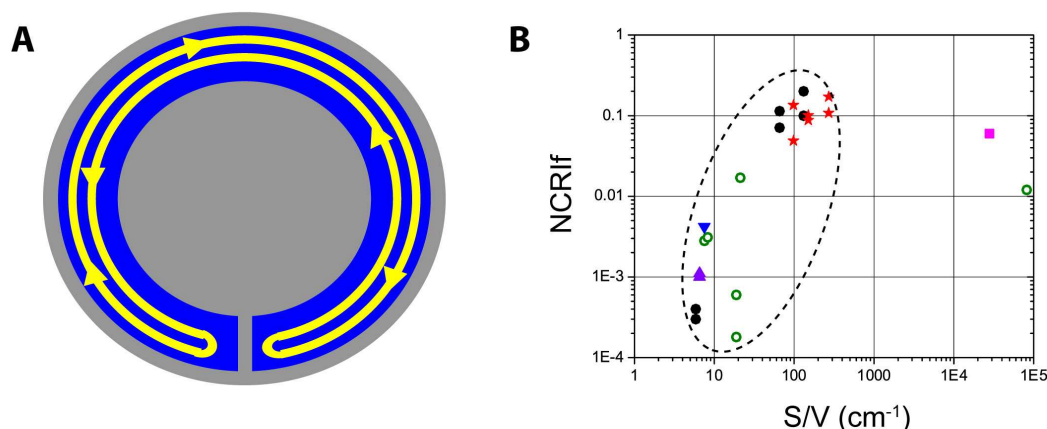


Figure 1.7: **TO experiments in various container geometries.**

(A) The 'blocked annulus' experiment: schematic of potential flow in a 'C' geometry. (B) NCRIf as a function of the surface-to-volume ratio ( $S/V$ ) of the TO container., reproduced from [103]. The data contained within the dashed ellipse are for 'bulk' geometries in which the solid samples are grown within a bulk cavity rather than inside porous media, and for these samples the NCRIf appears to increase with the surface-to-volume ratio. The two points to the right, lying outside of the dashed ellipse, are samples grown in a porous medium (porous gold), and do not seem to follow the general trend for sample grown in the bulk geometries. For an explanation of the meaning of the symbols, see [103].

the small frequency shift in the blocked cell.

The blocked annulus effect was also observed by Rittner and Reppy in a TO in which they could reversibly block and unblock the cell and were able to reproduce the results of Kim and Chan, observing at least a 20-fold reduction in the period change and perhaps even more (it is not obvious that within the range of their signal-to-noise that any frequency shift can be observed) [103].

The dependence of the TO frequency shift on the geometry of the container has also been studied, and these observations fit into two broad categories. The first category is that of solid samples grown in bulk geometries, cylinders and annuli. For this type of solid sample, Rittner and Reppy noticed that the maxi-

imum frequency shift ( $\propto \text{NCRIf}$ ) appeared to increase as the surface-to-volume ratio increased; the largest frequency shifts were observed for thin annuli and the smallest for large, open cylinders. They suggested one interpretation of this result could involve a network of dislocations in the bulk solid, some types of which have been shown to be superfluid along their cores (Sec. 1.5.2). Dislocations may form preferentially near cell walls in solid  $^4\text{He}$ , forming a layer of disorder. For maximal connectivity of the dislocation network (for a given dislocation density), and therefore the largest NCRIf, the disorder layer would be half of the wall-to-wall separation, which is consistent with the largest NCRIf observed in thin annular cells. This picture of superflow along the cores of a network of dislocations can explain lower values of NCRIf ( $\sim 0.1\%$ ) but the largest values of the observed NCRIf, up to 20% for some samples in [103], cannot be quite reconciled with typical values of observed dislocation densities.

The second category of container geometry involves solid samples grown in highly disordered, porous materials such as porous gold, Vycor glass and silica aerogel (also in cylindrical or annular shapes)[72, 73, 85]. Although the surface-to-volume ratio increases by two to three orders of magnitude relative to the bulk geometries, the TO frequency shift seems to be insensitive to this change. These experiments are commonly cited as evidence that the TO frequency shift cannot be completely explained by superflow along grain boundaries: enormous surface areas are required to support a superflow of just 1%, which would require crystallites that have average size of about 20 nm . In the most extreme case reported, the NCRIf was as high as 20%, and would require grains on the angstrom scale [103]. From X-ray studies, however, it is known that the crystallites are usually of the order of tens to hundreds of microns (see Section 1.4.7). In a joint X-ray-TO study of solid  $^4\text{He}$  grown in aerogel, it was shown that the

NCRIf of a sample with 100 nm grains displayed the same NCRIf as that of samples grown with techniques that reliably produce single-crystal specimens [36, 85]. In light of the behavior of solid  $^4\text{He}$  grown in porous media, it is also difficult to imagine that the TO frequency shift could be explained by a model wherein the grains slip relative to one another.

Although there appear to be flaws in the models of the supersolid signal as superflow along grain boundaries or along the cores of dislocations, there are several experiments that indicate that disorder plays a large role in the TO phenomena. These experiments will be discussed in Section 1.4.

### 1.3.6 Interaction of $^4\text{He}$ with Container Walls

I conclude this introduction the TO experiments on solid  $^4\text{He}$  with a brief discussion of the microscopic interaction of the helium and the the inner surface of the walls of the TO container. An important question for the TO experiments is how this boundary condition can affect the measured resonant frequency. If the helium slips relative to the walls of the container, this could mimic the effect of a certain amount of the mass of the helium decoupling from the walls of the container. However, in all of the explanations of the TO experiments, from the Andronikashvili experiment up to the contemporary discussion of the “supersolid” behavior, the discussion of the helium-surface boundary is largely absent. I hypothesize that the reason for this absence is that helium is thought to bind strongly to nearly all surfaces: it is considered a “universal wetting liquid” [76]<sup>7</sup> since the interatomic forces that bind the helium liquid together are generally weak compared to the attractive interaction between the helium and

---

<sup>7</sup>With one exception, to be discussed.

the surface to which it binds. Cheng et al. [33] have done the following calculation for the binding of  $^4\text{He}$  to various metal substrates: the alkali metals Li, Na, K, Rb and Cs and the alkaline earth metal Mg. Adsorbate-substrate interactions have the general form of (1) a short-ranged attractive potential of depth  $D$  between the adsorbate and the substrate plus (2) a long-ranged Van der Waals tail  $\sim C_3/z^3$ , where  $z$  is the distance from the substrate surface to the adsorbant atom. The very short-ranged repulsive interaction, due predominantly to the exchange energy from the overlap of the charges of the adatoms and substrate, has the effect of reducing the depth of  $D$ . The authors use a simple form of the total interaction potential  $V(z)$  that captures these features, the so-called “9-3” potential,

$$V(z) = \frac{4C_3^3/27D^2}{z^9} - \frac{C_3}{z^3}, \quad (1.15)$$

where  $C_3$  and  $D$  are interaction parameters characteristic of the particular surface-helium interaction. They add this term to a total energy which is a functional of the helium density and, using density functional theory, calculate adsorption properties such as the contact angle of a helium droplet with the substrate surface. Their calculations are at  $T = 0$ , so that all of the liquid  $^4\text{He}$  is expected to be superfluid. The general assertions of their work can be summarized as follows:

- $^4\text{He}$  binds strongly to surfaces, with one exception: the larger alkali metals Cs, Rb and K. They mention that their work is the first to provide theoretical evidence that superfluid  $^4\text{He}$  will fail to wet *all* substrates.
- Insulators generally have larger well depths  $D$  compared to metals with the same  $C_3$  value, and so  $^4\text{He}$  would be expected to bind even more strongly to these materials.

- For the alkaline earth metal Mg the first layer of helium on the surface is so strongly bound it is expected to be solid.

Indeed, third sound experiments on  $^4\text{He}$  films show that whereas superfluid  $^4\text{He}$  wets the surface of a glass slide because of the strong surface- $^4\text{He}$  interaction, it does not wet the surface when the slide is covered with cesium (for films less than a certain thickness) [70]. Torsional oscillator experiments designed to study the superfluid transition in  $^4\text{He}$  films also rely on the assumption that there is an adsorbed layer of helium, roughly 2 monolayers thick, that does not contribute to the mass decoupling at the transition [21].

All of the foregoing was intended to suggest a reason that the discussion of the surface-helium boundary effects have been absent from the discussion of the TO results, namely the general assumption that helium binds rather strongly to surfaces. It should certainly not be construed as *proof* that effects of slipping do not exist. For such a discussion, more detailed calculations of the type above would need to be performed for the interaction of  $^4\text{He}$ , at solid densities, with some of the specific substrate materials relevant to the TO experiments (such as BeCu, AgCu, or Stycast). Such calculations would also need to explain why the helium-surface interaction, if it were sufficiently weak to result in a slipping effect, would be temperature-dependent with a feature around 100 mK.

## 1.4 Other Recent Experiments on Solid $^4\text{He}$

There have been far more experiments performed on solid  $^4\text{He}$  at low temperatures than can be suitably addressed in this dissertation; for a recent review

please see [19]. I include here those results that are most often cited when discussing the results of the TO experiments or that are most relevant to the conclusions of this dissertation.

### **1.4.1 Effect of Annealing and Sample Preparation**

Soon after the first observation of NCRI by Kim and Chan, a few groups reported on the effect of annealing the solid  $^4\text{He}$  samples by holding the sample at temperature just below the melting curve. The most reproducible result was first reported by Rittner and Reppy [101]. They found that they could reduce the frequency shift and dissipation peak both partially and completely, depending on the annealing protocol. In a paper the following year [102], Rittner and Reppy showed that if the  $^4\text{He}$  solid was grown in an annular geometry, the size of the frequency shift was dependent on how rapidly the sample was cooled from the high pressure liquid through the melting curve. They prepared a sample by cooling to below 1 K over three hours, measured its frequency shift and dissipation peak, and then rapidly melted the sample and quench-cooled it to below 1 K in just 90 s. They found that the quench-cooled sample had a frequency shift that was about four times larger than the slowly cooled sample, with roughly the same ratio for the dissipation peak. Moreover, the quench-cooled sample had a much larger pressure (51 bar vs 41 bar for the slowly cooled sample). The implication of this experiment is that quench-cooling the sample introduces some type of disorder, such as grain boundaries or crystal dislocations, which can be annealed away. Since the magnitude of the NCRI is reduced upon annealing, the supersolid behavior is intimately tied to the disorder present in the solid. As we saw in Section 1.3.5, though, there are flaws in attributing the

entire TO frequency shift to superflow along grain boundaries or the cores of dislocations.

Clark, West and Chan also studied the effect of sample preparation on the supersolid signal [36]. They prepared samples both by the “blocked capillary” (BC) method (cooling the high pressure liquid along and then off of the melting curve at constant volume) and also by constant pressure (CP) / constant temperature (CT) methods, which produce less disorder<sup>8</sup>. They found that in the CP/CT samples, the supersolid signal was smaller and the transition region was sharper. The ability to reduce both the frequency shift and the dissipation peak was also reported in [36] and they also observed a simultaneous reduction in  $T^*$  (the location of the dissipation peak) as the height of dissipation peak was diminished. They observed that the ratio of the dissipation peak to the total frequency shift,  $|\Delta Q^{-1}| / (\Delta f^{max} / f_0)$ , evolved nonmonotonically with each stage of the cumulative annealing procedure. They claimed that they could not completely anneal the signal away, unlike the result from [101], and that the signals from most well-annealed samples approached those of the CP/CT samples.

These results convinced many workers of the essential role of disorder in determining the properties of the supersolid. The type of disorder playing that role - whether vacancies/interstitials, grain boundaries, dislocations or disclinations, or even glassy pockets of superfluid - would have to be determined by other experiments.

---

<sup>8</sup>This study did not specifically quantify the disorder, but the well-established CP/CT techniques have been shown, using in situ X-ray diffraction or optical birefringence, reliably to produce single-crystal or near-single-crystal samples [39, 54, 59, 118].

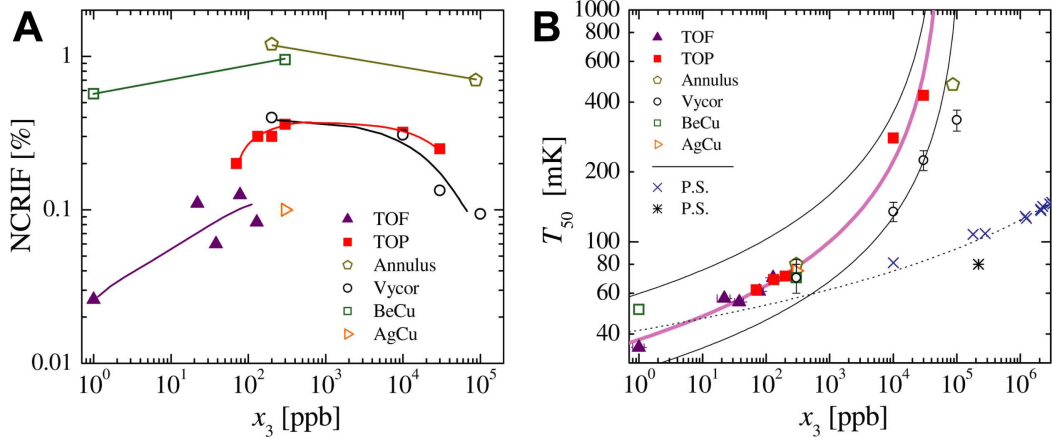


Figure 1.8: **Effect of adding  $^3\text{He}$  impurities on supersolid signal.** (A) Dependence of NCRIF on  $^3\text{He}$  concentration  $x_3$ . (B) Dependence of  $T^*$  on  $x_3$ . For a definition of the symbols used, see [75].

#### 1.4.2 Effect of $^3\text{He}$ Impurities

Another important early result was the effect of introducing small amounts of  $^3\text{He}$  impurities into the  $^4\text{He}$  solid, first reported in [72]. The effect was to both change the magnitude of the frequency shift as well as to push the  $T^*$  to higher temperatures. A more comprehensive study has been reported in [75]. In that paper, they find that as the  $^3\text{He}$  concentration  $x_3$  is varied, the NCRIF increases with  $x_3$  until it reaches a maximum at  $x_3 \sim 100$  ppb and then begins to decrease again [Fig. 1.8(A)]. Because of the sensitivity of the NCRIF to the sample preparation method as well as the geometry of the container, it is difficult to draw any serious conclusions from this dependence because the sample preparation and cell geometry are not well controlled.

A more interesting result from this work concerns the dependence of the characteristic temperature  $T^*$  of the supersolid signal on  $x_3$  [Fig. 1.8(B)]. There is a relationship between the pinning of dislocation lines and the presence of  $^3\text{He}$  impurities that has been well known for many years from ultrasound mea-

measurements [66] and the results from [75] seem to indicate another instance of disorder - this time a dislocation network - playing an important role in the characteristics of the supersolid. The argument goes as follows. In solid  $^4\text{He}$ , dislocations lines form a 3D network of immobile nodes connected by mobile segments (of typical length  $L_N$ ) that can bend in response to a stress field, producing a strain [53]. This dislocation motion can therefore reduce the shear modulus by up to  $\Delta\mu/\mu = -0.1 \times \Lambda L^2$ , where  $L$  is the average dislocation loop length and  $\Lambda$  is the total dislocation line density (line length per unit volume). For a well-defined network,  $\Lambda L^2 = \Lambda L_N^2$  is a constant (3 for a cubic network of dislocations), and so the shear modulus can be reduced by up to 30% from its intrinsic value  $\mu$ .

Helium-3 impurities can condense onto these dislocation lines and behave as additional pinning sites. The additional pinning sites reduce the motion of the dislocation segments in between the nodes, which tends to restore the intrinsic shear modulus of the crystal. One can identify a temperature  $T_{IP}$  at which this becomes significant; it is the temperature at which the (temperature-dependent) average length between condensed  $^3\text{He}$  impurities  $L_{IP}$  becomes comparable to  $L_N$  and is of the form

$$T_{IP}(x_3) = -2E_B \left( \ln \left[ \frac{L_{IP}^3 E_B}{4\mu b^6} x_3^2 \right] \right)^{-1} \quad (1.16)$$

where  $b$  is the magnitude of the dislocation's Burgers vector<sup>9</sup> and  $E_B$  is the binding energy of a  $^3\text{He}$  impurity, roughly 0.6 K according to [88]. Fig. 1.8(B) shows a plot of  $T^*$  vs.  $x_3$  for several samples compared to the prediction of Eq. 1.16. The data and the curve from the impurity-pinning theory are in good agreement, suggesting that the supersolid signal has something to do with the existence

---

<sup>9</sup>This calculation was done for edge dislocations, which move easily in the basal plane of the hcp crystal.

and mobility of a dislocation network within the  $^4\text{He}$  solid. Some theoretical ideas that relate dislocations and the presence of supersolidity will be discussed in Sec. 1.5.2.

A comment about the binding of  $^3\text{He}$  to dislocations is in order. It may seem surprising that  $^3\text{He}$  binds dislocations since it is lighter than  $^4\text{He}$  and therefore has more zero-point energy. It also has a high diffusivity in the bulk  $^4\text{He}$  lattice, even at low temperatures. However, the larger zero-point energy is also responsible for the larger effective volume of a  $^3\text{He}$  impurity atom relative to the  $^4\text{He}$  lattice and it is believed that  $^3\text{He}$  atoms can minimize their elastic energy (relative to the bulk) by moving to a region of lower strain. For edge dislocations, the type believed to be mobile in hcp  $^4\text{He}$ , there is a region of compression on one side of the dislocation and a region of expansion on the other side, and a larger atom such as  $^3\text{He}$  will minimize its energy by going to the side where the lattice is expanded and the strain fields are lower. This argument does not thoroughly take into account the quantum nature of the problem, but calculations by Alan Dorsey have suggested that an edge dislocation provides a  $1/r$  potential in which the  $^3\text{He}$  can sit [20]. Finally, another mechanism of the pinning was suggested in [66]. Nuclear magnetic resonance measurements of the exchange frequency  $J_{34}$  of a  $^3\text{He}$  with a neighboring  $^4\text{He}$  atom indicate that  $J_{34}/2\pi = 0.6$  MHz, so from the point of view of ultrasound measurements (at 10 MHz), the  $^3\text{He}$  appears to stay at a pinning site for several periods. However, at the relevant frequencies (kHz) of the torsional oscillator measurements (and the shear modulus measurement of the next section), the word “pinning” hardly makes sense. Perhaps a more accurate description of the effect of the  $^3\text{He}$  atoms condensed onto dislocation lines is that provide additional drag forces on the dislocation lines as they move back and forth at kHz frequencies.

### 1.4.3 Shear Modulus Stiffening

In [43], Day and Beamish reported the increase in the shear modulus  $\mu$  of a slab of  $^4\text{He}$  confined between two plates as the temperature was lowered below about 200 mK. This was done by embedding the solid helium between two piezoelectric crystal stacks, one for applying a known shear stress and the other for detecting the strain on the other side of the 180  $\mu\text{m}$ -thick sample. The increase in the shear modulus was about 11% ( $\Delta\mu \approx 16$  bar) from 200 mK to the lowest temperature. Their measurement had some of the same features as [88] but some were strikingly different. These properties are summarized in Table 1.2.

Day and Beamish also interpreted their results as a consequence of the existence of a network of dislocations. This certainly makes sense in light of the direction of the shear modulus change, the similar dependence of  $T^*$  on  $x_3$ , and the fact that annealing changed the high-temperature value of the shear modulus but left the low-temperature value unchanged. They also found that increasing the strain  $\epsilon$  above a critical value  $\epsilon_c$  ( $\approx 2.2 \times 10^{-8}$ ) resulted in a reduction of the shear modulus, an effect that appeared tantalizingly similar to the “critical velocity” effect reported in [72]. This also has a natural explanation in terms of the dislocation network: if a large enough stress is applied to the crystal, the dislocations segments can be torn away from the nodes and reduce the shear modulus, analogous to the evaporation of  $^3\text{He}$  impurities discussed in Sec. 1.4.2. This critical stress  $\sigma_c$  has been estimated to be 4 Pa for  $L_{IP} \approx 5 \mu\text{m}$ , corresponding to a critical strain  $\epsilon_c \approx 3 \times 10^{-8}$  (based on  $\sigma_c = \mu\epsilon_c$ , with the shear modulus of  $^4\text{He}$   $\mu \approx 100$  MPa), which is quite close to the observed value noted above. However, the inertial stress on the solid  $^4\text{He}$  inside (cylindrical)

Table 1.2: Comparison of measurements of shear modulus measurements by Day and Beamish and by Paalanen et al.

	Day and Beamish	Paalanen et al.
method	piezoelectric actuation	TO: standing torsion waves
$\Delta\mu > 0$ at low -T?	Y	Y
dissipation peak?	Y	Y
T range of $T^*$ (K)	0.04 - 0.15	0.25 - 1.75
effect of increasing $\epsilon$	reduce $ \Delta\mu $	lower $T^*$
effect of increasing $x_3$	higher $T^*$	higher $T^*$ , NO transition for ultrapure samples
effect of annealing	reduce $ \Delta\mu $ ; $\mu$ changes at high T	effect still present after "careful annealing"
effect of increasing $\omega$	higher $T^*$	N/A, fixed at 331 Hz

Symbols used:  $T^*$  is the temperature of the dissipation peak/maximum slope in  $\mu$ . The strain amplitude is  $\epsilon$ . The  $^3\text{He}$  concentration is  $x_3$ . The drive frequency is  $\omega$ .

torsional oscillators has been estimated as a function of the oscillator rim velocity as

$$\sigma \approx \pi \rho r^2 f v / 2$$

for a TO of radius  $r$  and resonant frequency  $f$  ( $\rho$  is the density of the helium)<sup>10</sup> [35]. The critical inertial stress implied by  $v_c \sim 10 \mu\text{m/s}$  is about two orders of magnitude smaller than the  $\sigma_c = 4 \text{ Pa}$  measured by the shear stiffening measurements. Moreover, an analysis in [35] concluded that the change in the resonant frequency of a TO due a change in the shear modulus  $\Delta\mu/\mu$  was about

$$\frac{\Delta f_0}{f_0} = (5 \times 10^{-7}) \frac{\Delta\mu}{\mu}.$$

The theoretical limit of  $\Delta\mu/\mu$  is around 30% in the Granato-Lücke theory of dislocations as explained above (roughly what is observed in [88]) and so the maximum frequency shift due to the change in the shear modulus could only be of the order of 0.1 ppm in the model of [35]. This is far smaller than the majority of observed frequency shifts by other groups. In our experiments, we observe a frequency shift typically of about 5 ppm, or 50 times higher than the theoretical limit. It is important to note, however, that this model of the effect of the change in the shear modulus only considers the change in the the magnitude of the modulus itself. A different model of the effect of containing a viscoelastic solid inside a TO was given in [125]; this will be treated in some detail in Chapter 3.

An important advantage of their experimental setup was the ability to probe the shear modulus anomaly at different frequencies; they report results for 20, 200 and 2000 Hz. They found that the characteristic temperature  $T^*$  shifted to higher values with increasing frequency, in agreement with the results of a study using a clever TO with two torsional modes (at 496 Hz and 1173 Hz) [14].

---

<sup>10</sup>There is a geometric correction for annular oscillators.

#### 1.4.4 Heat Capacity

The most recent heat capacity measurements of solid helium have also come from the group of Moses Chan. Using a special undoped-silicon calorimeter that significantly improved resolution below 100 mK, Lin, Clark and Chan measured the temperature dependence of the heat capacity of solid helium and found that if they subtracted the  $T^3$  phonon term (expected for a three-dimensional Debye solid) from the data that the heat capacity displayed a broad peak centered at  $\sim 75$  mK [80]. Since the authors believe that a supersolid description of the TO experiments is appropriate, they interpreted this peak as the thermodynamic signature of the supersolid. In a more recent study [81], the same group concluded that the temperature and height of this peak were independent of the  $^3\text{He}$  concentration, which is in stark contrast to the behavior of the frequency shift of TOs containing solid  $^4\text{He}$  with  $^3\text{He}$  impurities (Sec. 1.4.2). On the other hand, they compared the heat capacity peak in samples formed by blocked capillary (BC) and with constant pressure (CP) and found trend similar to the frequency shift: the height of the peak was reduced and it shifted to a lower temperature for the CP sample. Finally, they made the same measurement on a sample that consisted of 75% solid in coexistence with liquid and found that a peak existed for this sample as well. This is a fascinating result because a solid in coexistence with a liquid should be able to relieve internal stress and anneal away dislocations much more easily than a normal solid; measurements along the melting curve have shown dislocation densities four to seven orders of magnitude smaller than for solid crystals [114]. The authors suggest that its presence in an essentially stress-free sample implies that NCRI is intrinsic to solid helium and the role of stress and dislocations is only to enhance the effect.

Balatsky and coworkers reexamined an earlier version of the heat capacity data from Chan’s group and found that they could fit the low-temperature data better by adding a linear term to the  $T^3$ -phonon term<sup>11</sup>[18], a result that had been reported previously [50, 58]. A linear term in the specific heat is the hallmark of a (structural) glass, as shown by Zeller and Pohl for several amorphous solids [126]. They also calculated the excess entropy implied by the heat capacity peak and found that it was three orders of magnitude smaller than the entropy change of a Bose-Einstein condensate (representing a dilute gas of non-interacting vacancies) between  $T = 0$  and  $T = T_C$ , assuming a 1% condensate fraction. They proposed that the linear term in the specific heat could be explained by considering solid helium as a glass of dislocation loops. In their picture, the dislocation loops form an ensemble of tunneling systems (TSs) with a particular distribution of characteristic energies and tunneling amplitudes, and they play role analogous to that of two-level systems in structural glasses (such as amorphous  $\text{SiO}_2$ ) [10, 93], for which a linear term in the specific heat is predicted by a two-level system model of a glass.

### 1.4.5 DC Flow

The dc flow of a superfluid is related to that most amazing of properties, the dissipationless persistent current, and so not surprisingly a great deal of effort has been dedicated to searching for dc flow in solid  $^4\text{He}$ . Day and Beamish used a diaphragm in an attempt to push solid  $^4\text{He}$  through 36000 glass capillaries in parallel (each with a  $25\ \mu\text{m}$ -diameter and 3 mm long) [42]. Their measure-

---

<sup>11</sup>It is interesting to note that in Chapter 21 of [121], Wilks points out that earlier measurements of the heat capacity of solid  $^4\text{He}$  were also well fit by a Debye  $T^3$  plus a linear term [50, 58], and that the linear term was reduced by annealing, but that “this linear term has no obvious physical significance”.

ments indicated no flow down to 35 mK, despite the imposition of a chemical potential difference by compressing the solid on one side of the capillary array. This result was confirmed in a similar type of apparatus by Reppy's group, who extended the technique to low-frequency ac measurements as well [99]. Sasaki et al. showed that in a liquid-solid-liquid system, where the liquid reservoirs were held initially at different heights, superflow along grain boundaries (through the solid) caused the liquid levels to equilibrate [105]. Such equilibration did not happen in  $^4\text{He}$  crystals for which no grain boundaries were visible in their optical cryostat. Most recently, Ray and Hallock studied solid  $^4\text{He}$  in an experimental apparatus that allowed injection of  $^4\text{He}$  atoms directly from the superfluid into the solid [97]. Their superfluid-solid-superfluid system (in a Vycor-bulk-Vycor channel) was possible because the freezing pressure of the helium is increased (relative to the bulk) in the confined geometry of the Vycor pores [79, 123]. They observed flow through the solid and interpreted the dependence of the flow on the pressure difference across the solid as characteristic of critical superflow rather than that of a viscous liquid. They also can quantitatively account for the magnitude of the transport by calculating the flow along grain boundaries or along dislocations.

It seems that flow of superfluid  $^4\text{He}$  is possible along the grain boundaries of a solid sample. However, the absence of true dc superflow indicates that the state of solid  $^4\text{He}$  between about 20 mK and 100 mK might be best represented by a superfluid *above* its true transition temperature (i.e. in a "vortex liquid" regime as advocated by Anderson [8, 7]), or perhaps that there is a non-superfluid description of low-temperature solid  $^4\text{He}$ , such as the glass model of Balatsky et al. [18, 86]. In any case, the issue of dc flow would benefit from an experiment in which we can directly push on the superfluid component instead

of on the crystalline lattice. This possibility will be discussed in the context of future experiments in Chapter 6.

### 1.4.6 Other Evidence of Glassy Behavior

Clark, Maynard and Chan [35] observed several metastable low-temperature values of the frequency shift when they thermally cycled their TO-solid  $^4\text{He}$  system according to a particular protocol, shown schematically in Fig. 1.9. They initially prepared the system by cooling to their cryostat's base temperature ( $\sim 20$  mK) at a velocity  $v < v_c$  and then raising the velocity at base temperature to  $v \gtrsim v_c$ . The particular value of the lowest-temperature frequency shift depended on the highest temperature that the system had been at immediately before the cooling part of the cycle. The authors interpreted this "memory effect" in terms of the motion and pinning of vortices within the sample [7], but memory effects are also known in structural glasses as well [104]. Additionally, they observed extremely long relaxation times in the frequency after changing the temperature, similar to what we report in Chapter 4 and [62], but the similarity to the temperature dependence of the relaxation time is not obvious from [35].

Aoki, Keiderling and Kojima studied the relaxation of a solid  $^4\text{He}$ -filled TO after they abruptly changed the drive torque  $\Gamma$  [15]. They found that the relaxation of the dissipation (as measured by the displacement of the oscillator) had a complex relaxation profile which was not mirrored in the relaxation profile of the resonant frequency (nor in that of the displacement relaxation of the cell containing superfluid helium). The dissipation as a function of time could be

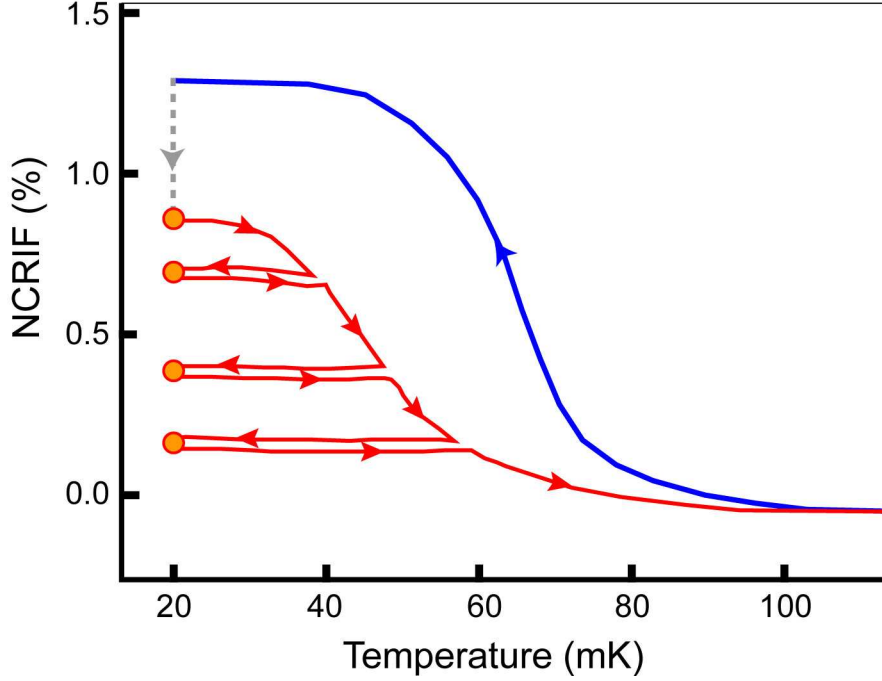


Figure 1.9: **Memory effects from thermal cycling.**

Shown here is a schematic of the results of experiment performed in [35]. The blue curve is the initial cooling, at  $v < v_c$ . The grey dashed line represents the increase of velocity at low temperature to  $v \gtrsim v_c$ . The red curve represents the thermal cycling protocol, with the direction of temperature change indicated by an arrow. The orange dots show the multivalued frequency shift at the lowest temperature, depending on the highest temperature the system had reached immediately before cooling back to base temperature. The vertical scale is approximate.

fitted by the sum of an exponential term with time constant  $\tau_1$  ( $\sim 10^3$  s) and a logarithmic term with a (much longer) time constant  $\tau_2$  ( $\sim 10^4$  s), and the time constant  $\tau_1$  increased as the temperature was lowered. They also reported “memory effects” (at 10 mK) to the extent that when they cycled the drive torque  $\Gamma_a \rightarrow \Gamma_b \rightarrow \Gamma_a$  the dissipation continued to follow its relaxation trajectory at the previous drive level. I believe, however, that the memory effects can be interpreted as a drive level-independent *temperature-induced* relaxation superimposed on the drive cycling, since immediately before initially changing the drive they cool their system within 20 minutes from 90 mK to 10 mK. We show

in Chapter 4 that there are additional relaxation processes associated with cooling the solid  ${}^4\text{He}$  into the supersolid state, and that the time constants for this relaxation are far longer than 20 minutes at 10 mK.

Grigor'ev et al. made careful measurements of the temperature dependence of the pressure of samples of solid  ${}^4\text{He}$  formed by the blocked capillary technique [56]. In the range 50 mK-500 mK they found that in addition to the usual Debye contribution to the pressure ( $\propto T^4$ ) there was a small term proportional to  $T^2$ . Since the pressure and heat capacity of the solid are related by the Mie-Grüneisen equation

$$\left(\frac{\partial P}{\partial T}\right)_V = \sum_i \frac{\gamma_i C_i}{V}$$

where  $V$  is the molar volume and  $\gamma_i$  and  $C_i$  are the Grüneisen parameter and heat capacity of the  $i^{\text{th}}$  subsystem, the  $T^4$  and  $T^2$  pressure terms correspond, respectively, to the  $T^3$  and  $T$  terms in the heat capacity, the latter being the signature of a structural glass (see Sec. 1.4.4 and [10, 93, 126]). Moreover, they found that the glassy term became dominant below 300 mK and that it could be reduced (and nearly eliminated) by annealing. As they annealed the sample by holding it at  $\sim 2$  K for 10 h, they observed an extremely slow relaxation in the pressure. They also found that as a result of the annealing process the total pressure of the sample was irreversibly reduced by 2 bar, a phenomenon also observed by Rittner and Reppy, who measured a pressure change of 7 bar during annealing [102]. This pressure change is far too high to be accounted for by the disappearance of dislocations or vacancies. They conjectured that the reduction in pressure might be due to recrystallization of glassy or metastable liquid pockets, whose volume fraction could be as high as 5%.

### 1.4.7 X-ray Diffraction and Neutron Scattering

The hcp structure of solid  $^4\text{He}$  was first determined by Keesom and Taconis, who studied a single-crystal sample by X-ray diffraction [69]. Schuch and Mills later showed that samples grown by the blocked capillary method resulted in the formation large crystallites of grain size  $> 0.1$  mm [107], and annealing was shown to increase this value [119]. X-ray diffraction studies have also been important in demonstrating the delocalized nature of the atoms in the helium solid; Burns and Isaacs have shown that vibrations due to the zero-point energy can be up to 25% of the lattice spacing [30].

In light of the new discoveries about solid helium and the apparent role of disorder in those phenomena, Burns et al. have recently revisited X-ray diffraction studies down to the relevant temperatures of the supersolid [31]. They grew their samples in a cylindrical volume<sup>12</sup> at a constant pressure of 60 bar, taking care to prevent blockage of the fill line during crystal growth by means of a heater, and looked for a signature of the “supersolid” signal down to the 45 mK base temperature of their dilution refrigerator. Such a signature might be manifested as a change in the average kinetic energy of the atoms or a modification of the interatomic potential; these effects would be detectable as a change in the lattice parameter or its slope as a function of temperature, or as a change in the integrated intensity of the scattered X-rays. They report no evidence of such a signature in either the measurement of the lattice parameter or the integrated intensity.

The “supersolid” signal is known to have a large dependence on the disor-

---

<sup>12</sup>The volume of their cell was  $0.13$  cm<sup>3</sup>, of the same order as the TO geometries. For a summary of the container volumes of 19 TO experiments, see [120].

der present in the system, including the possible role of grains, and so the authors also used an experimental setup that allowed them to observe small-angle grain boundaries. They observed a mosaic structure in the X-ray intensity, i.e. a number of distinguishable crystalline regions with sizes on the order of tens to hundreds of microns. What is perhaps more interesting for this dissertation was the fascinating observation that the peaks in the mosaic structure changed their positions from scan to scan over the course of two hours of measurement, well away from the melting curve. This shifting of the grains over long time scales may play a significant role in the observation of long relaxation times (sec. 1.4.6 and Chapter 4), although other studies have attempted to rule out superflow along grain boundaries as the complete explanation for the observed supersolid phenomena [36, 85]. In addition, they observed no evidence of any powder, liquid or amorphous component to the X-ray signature, in contrast to the idea of the previous section that the anomalously large pressure changes observed upon annealing might be due to the recrystallization of glassy pockets frozen within the solid helium.

Neutron scattering measures the momentum distribution  $n(\mathbf{k})$  of the constituents of a system, and so BEC will appear as an enhancement of  $n(\mathbf{k})$  close to  $k = 0$  as a macroscopic number of the constituents begin to occupy the  $k = 0$  state as the system is cooled through its BEC transition. The momentum distribution of a system undergoing BEC is

$$n(\mathbf{k}) = n_0\delta(\mathbf{k}) + (1 - n_0)n^*(\mathbf{k})$$

where  $n_0$  is the condensate fraction and  $n^*(\mathbf{k})$  is the momentum distribution of the atoms in states for which  $\mathbf{k} > 0$  (i.e. not in the condensate). Recent studies on crystals grown by the blocked capillary method did not find any evidence of a condensate fraction down to 80 mK, within the 1% error of their experiment

[45]. Additionally, they do not find any change in the shape of the momentum distribution, which could also be used to estimate  $n_0$ . Another experiment, which measured the average kinetic energy of the atoms, also found that there was no signature of BEC down to 70 mK, in both single-crystal and polycrystalline samples [1]. Neither of these experiments reported any observation of a liquid-like or amorphous component of the momentum distribution.

## 1.5 Modern Theories of the Supersolid State

The essential role of disorder has been suggested by the strong dependence of the torsional oscillator observables on sample preparation, crystal annealing and the behavior of  $^3\text{He}$  impurities, but importantly a definitive answer about the nature of the disorder is absent from structural measurements such as X-ray scattering<sup>13</sup>. As an answer to this, theoretical researchers have produced a great deal of important work attempting to reconcile the proposed existence of disorder with the possibility of superfluidity in solid  $^4\text{He}$ . This section will discuss several of these theories and how each has contributed to our understanding of that reconciliation. Sec. 1.5.1 will discuss ideas about how it is possible in principle to have disorder and superfluidity in a quantum system, Sec. 1.5.2 will discuss some details about the relationship between superfluidity and stress in a crystal, and Sec. 1.5.3, on the possibility that the supersolid we observe actually constitutes observation of a “vortex liquid” phase, is included because it makes an important connection to the well-understood behavior of vortices in 2-D superfluid helium studied with TOs.

---

<sup>13</sup>It might be argued that the X-ray experiments described in the last section have ruled out superflow along grain boundaries as the complete explanation for the TO frequency shift.

### 1.5.1 Superglass Theories

The notion that the behavior displayed by low-temperature solid  $^4\text{He}$  might be attributed to a glass was put forth by Balatsky and coworkers [18, 86]. Their idea was that the dislocation network in the solid might constitute an ensemble of tunnelling systems, in analogy to the two-level systems that tunnel between structural configurations in a well-known glass such as amorphous  $\text{SiO}_2$ . Other researchers have considered a natural extension of the idea of solid  $^4\text{He}$  as a structural glass to include the bosonic nature of the  $^4\text{He}$  atoms, and, using several independent methods, have concluded that solid  $^4\text{He}$  could be a *superglass*. This is a kind of solid in which it is possible simultaneously to observe a glassy component, usually structural in nature, and off-diagonal long-ranged order (ODLRO), which is a necessary condition for superfluidity.

Boninsegni, Svistunov and Prokof'ev studied condensed  $^4\text{He}$  numerically, using path-integral Monte Carlo (PIMC) methods, and reported the observation of a metastable disordered phase of solid  $^4\text{He}$  that also displayed ODLRO [29] in a system of  $N$   $^4\text{He}$  atoms ( $N = 216$  and  $800$  in two separate studies). They studied two different "samples" that differed only in their initial configurations and how they arrived at the low-temperature state. The first sample, which was initially configured as an ideal hcp crystal, was found to have long-ranged pair correlations and an exponential decay in the single-particle density matrix, i.e. no ODLRO. This study confirmed their earlier assertion that an ideal hcp crystal does not have a Bose condensate, an old idea due to Onsager and Penrose [91], and that supersolids must be generically incommensurate (i.e. that the number of atoms per unit cell is not an integer). The surprising thing they found was with the second sample, for which they designed a simulation protocol in-

tended to mimic the effect of quench-cooling the sample from a high-pressure liquid, the procedure by which the largest supersolid fraction is observed experimentally. In this sample, the phase that emerged displayed hcp crystalline order only at short distances (2-3 coordination spheres) and moreover exhibits ODLRO, with which they could calculate the spatial distribution of the condensate wavefunction. The important observation of their work was that the  $^4\text{He}$  could remain in the metastable superfluid state even at densities associated with the solid. These results held true even for the high-pressure sample they studied ( $P = 155$  bar, molar volume  $V = 17$  cm<sup>3</sup>), which represented a 27% increase in density from the liquid at 25 bar ( $V = 23.3$  cm<sup>3</sup>). This finding also opened up the possibility that other types of disorder (grain boundaries, dislocations, etc.) might also display superfluid behavior, an idea that led to a number of discoveries about the role of stress and elasticity in promoting superfluidity. This will be discussed in the next section.

Although the numerical simulations are quite convincing of the existence of a structural glass<sup>14</sup>, PIMC cannot address the real-time dynamics of the system. Biroli, Chamon and Zamponi contributed a complementary and very appealing analytical picture of how such a state might form by mapping a viscous classical system known to exhibit glassy dynamics (the Brownian hard-sphere problem) to a new quantum many-body system of bosons [22]. The Brownian hard-sphere system, a liquid at low (number) density  $n \equiv N/V$  (or, equivalently, the *packing fraction*  $\phi \equiv \pi n \sigma^3 / 6$ , where  $\sigma$  is the diameter of an atom), will crystallize into an ordered solid if the density is increased slowly enough, but if the density is increased too quickly the system will jam into a disordered glass

---

<sup>14</sup>The type of glass that these researchers find seems to be closer to the “glassy pocket” idea of Grigor’ev [56], rather than the tunneling dislocation model of Balatsky et al., although the two models likely have many similarities.

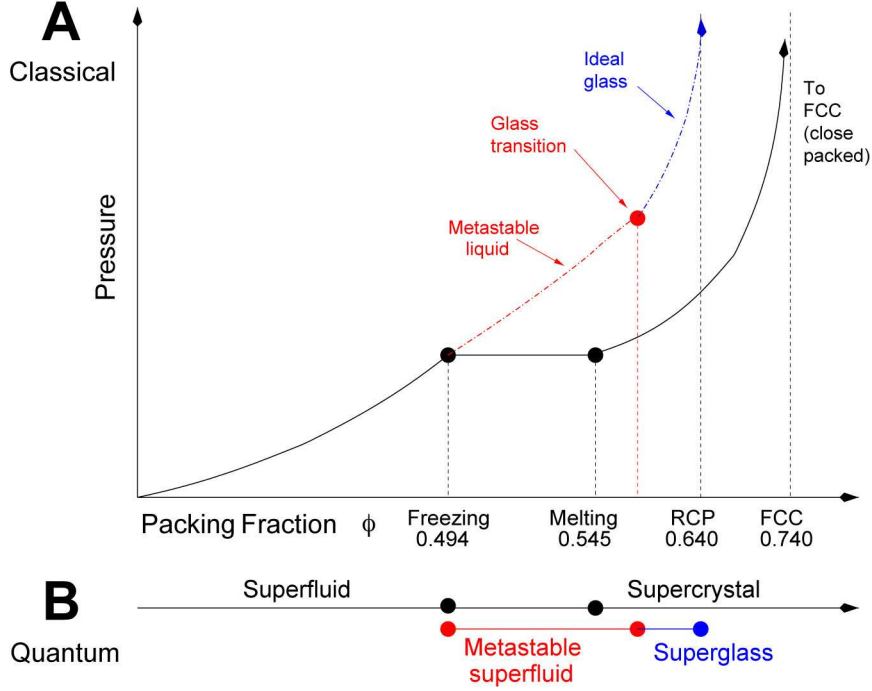


Figure 1.10: **Comparison of classical Brownian hard-sphere phases and corresponding quantum many-body phases.**

(A) Classical phases of the Brownian hard-sphere problem. The black trajectory is a simple freezing transition, obtained if the packing fraction  $\phi = \pi n \sigma^3 / 6$  is reduced suitably slowly. If  $\phi$  is reduced too rapidly, the system will follow the colored (red-blue) trajectory and jam into a dense amorphous glass. (B) Corresponding quantum phases of a system of interacting bosons obtained by the mapping described in the text.

[see Fig. 1.10(A)].

Their approach is as follows: they begin with the viscous dynamics of a system of  $N$  classical particles described by the Langevin equations

$$\gamma_i \frac{d\mathbf{x}_i}{dt} = -\frac{\partial}{\partial \mathbf{x}_i} U_N(\{\mathbf{x}\}) + \vec{\eta}_i(t)$$

where  $\gamma_i$  are friction coefficients and  $\vec{\eta}_i$  is a Gaussian white vector noise proportional to the thermal energy  $k_B T$ . The index  $i$  runs from 1 to  $N$ ,  $\{\mathbf{x}\} \equiv \{\mathbf{x}_1 \dots \mathbf{x}_N\}$ , and the total potential  $U_N$  is assumed to be a sum of symmetric pair potentials:  $U_N(\{\mathbf{x}\}) = (1/2) \sum_{i \neq j} V(\mathbf{x}_i - \mathbf{x}_j)$ . As is well-known, the evolution equation for the probability distribution of the  $N$  particle positions,  $P(\{\mathbf{x}\}, t)$ ,

can be written as a Schrödinger equation in imaginary time

$$\frac{\partial}{\partial t} P = -H_{FP} P$$

where  $H_{FP}$  is the so-called “Fokker-Planck” operator, given by

$$H_{FP} = - \sum_i \frac{1}{\gamma_i} \frac{\partial}{\partial \mathbf{x}_i} \left[ \nabla_i U_N + k_B T \frac{\partial}{\partial \mathbf{x}_i} \right].$$

The mapping to the quantum dynamics is achieved by a similarity transformation between the (Hermitian) quantum many-body Hamiltonian  $H$  and the classical (non-Hermitian) Fokker-Planck operator according to

$$H = e^{U_N/2k_B T} H_{FP} e^{-U_N/2k_B T}$$

( $\hbar = 1$  for simplicity). It turns out that the quantum Hamiltonian contains a effective potential  $V_{eff}$  that is a sum of two- and three-body interactions. The eigenfunctions of the Fokker-Planck operator and the new many-body Hamiltonian  $H$  are in a one-to-one correspondence, and moreover the ground-state wavefunction is of the Jastrow form [67]

$$\Psi_G \propto \exp \left[ -\frac{1}{4k_B T} \sum_{i \neq j} V(\mathbf{x}_i - \mathbf{x}_j) \right]. \quad (1.17)$$

With this mapping in hand, they considered a specific form of the two- and three-body potentials appearing in  $V_{eff}$  and were able to work out the properties of the corresponding quantum phases in Fig. 1.10(B). The important observation that they made is that there is a non-zero condensate fraction in each of the phases shown in Fig. 1.10(B).

## 1.5.2 Stress-induced Supersolidity

In the last section, we have seen two models in which it was possible to have simultaneous glassy disorder and superfluid order. In this section, we turn to a series of important numerical studies that reveal the details of how supersolidity might occur in the presence of specific types of disorder, namely along grain boundaries and the cores of dislocation lines, as well as potential mechanisms for supersolidity as a result of other structural characteristics of the solid. In Sec. 1.3.1, the Andreev-Lifshitz-Chester mechanism for supersolidity was described, whereby zero-point vacancies (or interstitials) in the  $^4\text{He}$  crystal, themselves bosons, could Bose condense and a current of vacancies could flow without dissipation through the helium solid. This argument is impossible on thermodynamic grounds because the energy for a creation of a vacancy,  $\Delta_v$ , is of the order of 10 K (even higher for interstitials), and so at 100 mK there is a negligibly small probability of having isolated vacancies in the crystal;  $^4\text{He}$  crystals are commensurate.

It is natural, then, to ask under what conditions could the energy for vacancy creation be driven to zero. Several researchers have speculated about the possibility of stress-induced supersolidity and have created phenomenological models describing possible scenarios [47, 109, 115]. Pollet and coworkers, some of whom worked on the PIMC study of the creation of a superglass [29], have investigated the idea of stress-induced supersolidity numerically, again using PIMC [96]. They considered several ways in which stress could be applied to the solid, both to the bulk and locally (e.g. by dislocations), and considered if any of the cases were experimentally feasible. These results are summarized in Table 1.3.

Table 1.3: **Stress-induced supersolidity in the bulk and in defects.**

type of stress	where	(critical) strain (%)	critical stress (bar)
(isotropic) hydrostatic decompression	bulk	13.5	25
(anisotropic) diagonal traceless strain	bulk	10-12	50
shear stress	bulk	15	35
screw dislocation	local	22	–
(split-core) edge dislocation	local	13	–

In the case of the bulk stress, the third column represents the critical strain for driving the vacancy creation energy  $\Delta_v$  to zero, and in the case of the local stresses (dislocations) the column represents the estimated strain at the core of the dislocation.

Moderate amounts of stress applied to the bulk can drive  $\Delta_v$  to zero, but in all three cases, the hcp crystal is unstable to this amount of stress (or in the case of decompression, it becomes a liquid). On the other hand, this work was a confirmation of their earlier observations of superfluidity along the cores of (stable) screw dislocations [28], along grain boundaries [95] and along certain types of edge dislocations [96] was feasible experimentally, since the strains calculated at the cores of the dislocations were as large as or larger than the bulk critical strains for  $\Delta_v \rightarrow 0$ .

This is a fascinating idea, but its relevance to the macroscopic behavior shown in the TO experiments is not clear. Perhaps the thermally fluctuating dislocation lines above  $T^*$  play some role in suppressing the global phase coherence necessary for superfluid flow, or perhaps the vacancies created in the cores of the dislocations have a way of tunneling into the bulk and participating in an Andreev-Lifshitz-Chester type of supersolid.

### 1.5.3 Vortex Fluid

In two papers [8, 7], Anderson discusses the possibility that the true supersolid transition occurs at a temperature  $T_c$  much lower than the typical  $T^*$  measured in the TO experiments and that the relevant physics of the temperature regime centered around  $T^*$  is that of a fluid of quantized vortices whose motion can dissipate energy via the mechanism of phase slippage [6]. He makes the analogy between the “nonlinear rotational susceptibility” (NLRS) measured by the TO experiments (see Section 3.1) and the nonlinear magnetic susceptibility in the “pseudogap” (phase-disordered) regime of the high-temperature supercon-

ductors [48], where there is significant evidence of the presence of vortices even when superconductivity is destroyed [117]. He argues that the phenomena measured by the TO experiments have their origin in the intrinsic properties of this vortex fluid (the vortices above  $T_c$  have a viscous drag coefficient  $\eta = \hbar n_v$  that depends on their density  $n_v$  [and in turn on the temperature]) and not to any critical behavior at a phase transition.

This treatment of the supersolid naturally explains the existence of the dissipation peak as the coincidence of the vortex damping rate and the probe frequency of the experiment (in this case, the resonant frequency of the TO), analogous to the existence of the dissipation peak in the Kosterlitz-Thouless transition [25]. According to Anderson, the  $^3\text{He}$  dependence of the  $T^*$  is explained in terms of additional drag on the vortices, which should slow their motion. However, since the vortices would be less strongly pinned by structural defects, the utility of this model to explain the annealing effects is less obvious. Finally, since the temperature regime of the TO experiments represents the phase-disordered regime where global phase coherence is destroyed, there may still be a finite superfluid density but an absence of true macroscopic dc supercurrents. The vortex fluid model has been used by some researchers to explain their observations qualitatively [35, 15], but the utility of this model to explain the majority of the TO, structural and thermodynamic data is limited by its lack of quantitative predictions.

In a follow-up paper [65], Huse and Khandker developed a phenomenological model for the TO response in the context of a vortex fluid, which model has a simple prediction for the relation between the magnitude of the dissipation peak  $|\Delta Q^{-1}|$  and the total shift in the resonance frequency  $\Delta f^{tot} / f_0$ . They

find that within their model,  $|\Delta Q^{-1}| / (\Delta f^{tot} / f_0) \sim 1$ , which is roughly consistent with the results from the TO Kosterlitz-Thouless studies. However, they point out that this ratio in the experiments in solid  $^4\text{He}$  has a large variation, from their value  $\sim 1$  [101] all the way down to 0.01 [74]. (Our experiments find roughly 0.1). The authors attribute this range in the size of the damping for a given frequency shift to inhomogeneous broadening of the dissipation peak due to a distribution of local decoupling transitions, which in turn is dependent on the degree of homogeneity with the particular sample of solid  $^4\text{He}$  studied. As far as I know, this is the first work to address the large disparity from experiment to experiment in the ratio  $|\Delta Q^{-1}| / (\Delta f^{max} / f_0)$ . The quantitative relation between  $\Delta Q^{-1}(T)$  and  $\Delta f(T) / f_0$  is an important theme to which we will return many times in this dissertation.

## CHAPTER 2

### EXPERIMENTAL METHODS

This chapter will describe the three components central to the operation of the experiments described in this dissertation: (1) the refrigeration techniques necessary to attain the low temperatures at which the supersolid signal appears, (2) the SQUID-based torsional oscillator, a new manifestation of a classic technique for studying superfluid helium, and (3) the creation and measurement of the extremely high pressures needed to form the  $^4\text{He}$  solid.

#### 2.1 Dilution Refrigerator

In order to achieve the sub-300 mK temperatures necessary to study the supersolid transition in  $^4\text{He}$ , for our purposes it is most useful to use a dilution refrigerator (DR) because of the relatively fast thermal time constants and high cooling power compared to other methods (e.g. adiabatic demagnetization of nuclear or electronic spins). The use of a SQUID-based displacement sensor, which is extremely sensitive to magnetic fields, and the temperature range of the experiments (10-500 mK) further indicate that a dilution refrigerator is the correct choice.

The apparatus contained within the vacuum can (VC), including the refrigerator and the experimental space, is shown in Fig. 2.2. The entire apparatus will often be referred to as the “cryostat”. The major components of the refrigeration part of the apparatus are labelled in blue type and are located above the dashed line. I will not describe the operation of a DR in much detail here; the interested reader is directed to the excellent descriptions in [94] and [100]. The DR is based

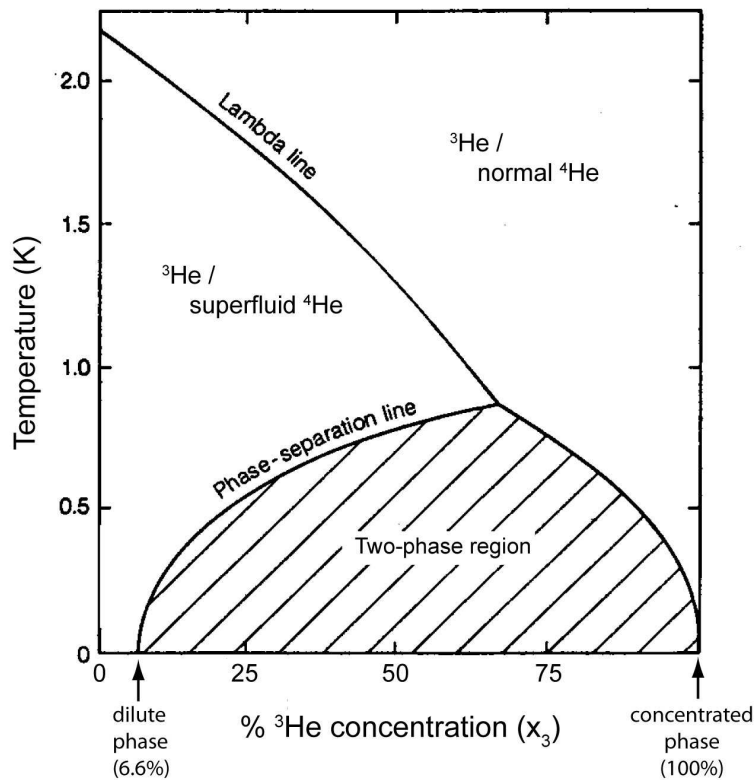


Figure 2.1: **The  $^3\text{He}$ - $^4\text{He}$  phase diagram.**

At  $T = 0$ , the mixture has separated into two phases, the “dilute” phase of 6.6%  $^3\text{He}$  in  $^4\text{He}$ , and the “concentrated” phase of 100%  $^3\text{He}$ . Concentrations of  $^3\text{He}$  in the hatched area are forbidden. Reproduced from [121].

on the circulation of a mixture of  $^3\text{He}$  and  $^4\text{He}$ , which can lower its enthalpy by separating into two phases in the mixing chamber, one light phase (the “concentrated phase” of nearly 100%  $^3\text{He}$ ) that sits on top of a heavier phase (the “dilute phase” of 6.6%  $^3\text{He}$  dissolved in  $^4\text{He}$ ). This phase separation occurs when the  $^3\text{He}/^4\text{He}$  mixture is at or below 0.87 K, depending on the initial concentration  $x_3$  of  $^3\text{He}$  in the mixture (Fig. 2.1). If one can then remove  $^3\text{He}$  atoms from the dilute side of the phase boundary they will be replenished by  $^3\text{He}$  atoms from the concentrated side; the process of replenishing requires energy, which is the source of the cooling power of a DR. In practice, this is achieved by pumping on the still, which is directly connected to the dilute side of the phase boundary.

I find it useful to imagine this process analogously to evaporative cooling: the dilute phase is a “gas” of  $^3\text{He}$  in an inert background of  $^4\text{He}$  and the concentrated phase is the “liquid”. Pumping on the still/dilute side evaporates  $^3\text{He}$  atoms from the “gas” ( $\sim 1000\times$  faster than  $^4\text{He}$  atoms), which are then replaced by atoms from the “liquid” that cross the phase boundary and provide cooling.

The other components of the DR shown in Fig. 2.2 are the 1K pot and the two types of heat exchangers. After the  $^3\text{He}$  is pumped away from the still/dilute phase, it is purified by passing it through a charcoal trap immersed in liquid nitrogen and then through a charcoal-free trap immersed in liquid  $^4\text{He}$  (not shown in Fig. 2.2). It is then recondensed by passing it through a wound copper tube in the bath of liquid  $^4\text{He}$  outside the VC and then through a high-impedance tube that is heat sunk to the 1K plate. The returning  $^3\text{He}$  is then a liquid at about 1.4 K, but it is not yet cold enough to undergo subsequent phase separation in the mixing chamber. This step is achieved by thermally linking the returning  $^3\text{He}$  to the still (at 0.6-0.8 K) by two stages of heat exchangers.

All components of our DR from the still down were purchased as a single unit from Janis Cryogenics<sup>1</sup>. The rest of the fridge, including the 1K pot and all of the pumping lines and vacuum can, was designed by Minoru Yamashita. The gas handling system was also designed and homebuilt by Dr. Yamashita, with the exception of the two parallel charcoal nitrogen traps, which were designed by Ethan Pratt. The pump used to circulate the  $^3\text{He}$  is a magnetically-coupled rotary vane pump<sup>2</sup> with an oil mist filter<sup>3</sup> at the output (return line) of the pump. We were able to run the fridge without warming above 4K for 6-8 months and for about 16 months including a single partial warmup to  $\sim 100$  K

---

<sup>1</sup>Janis, model JDR-100

<sup>2</sup>Pfeiffer, model DUO35M, pumping speed  $35\text{ m}^3/h$ .

<sup>3</sup>Balston, model CV-0118-371H

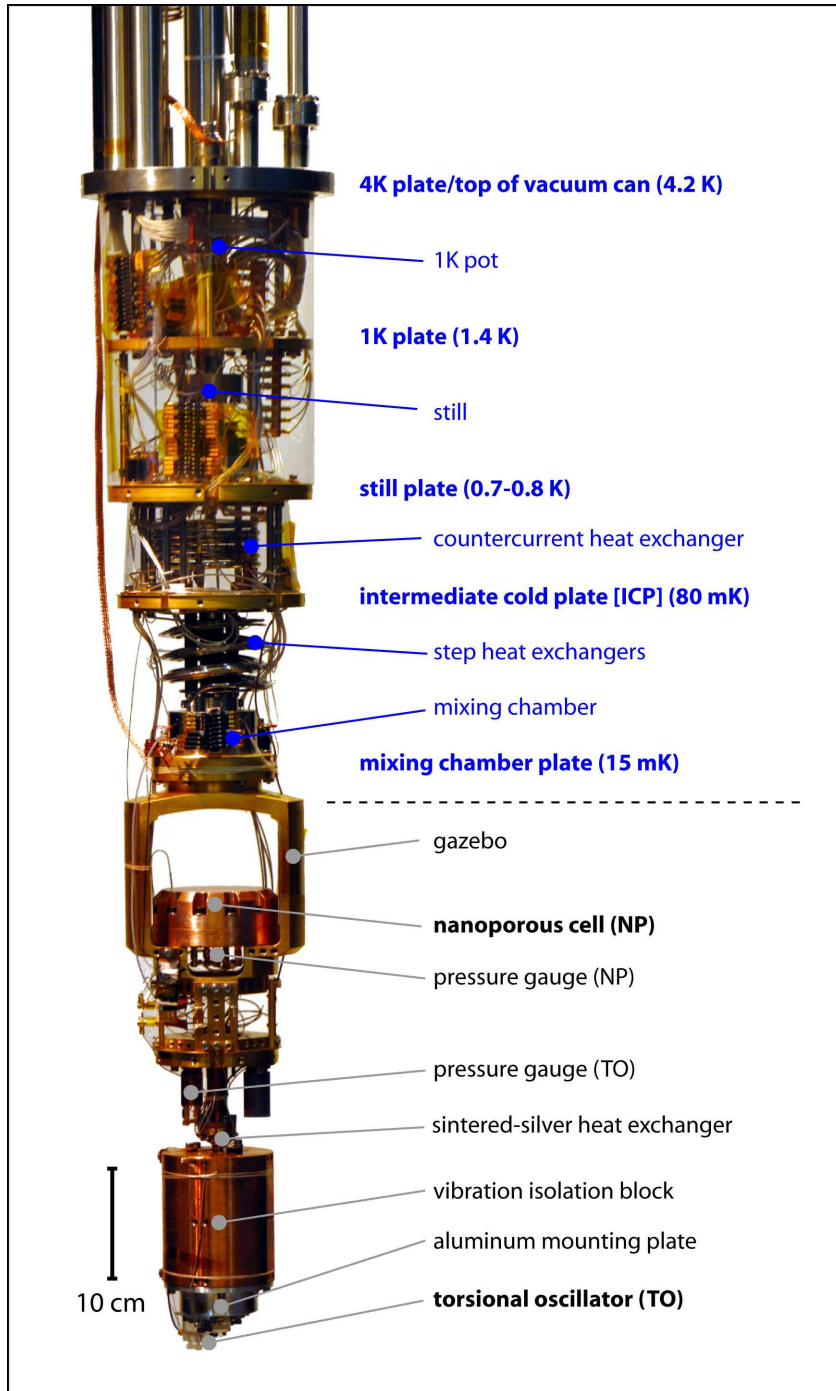


Figure 2.2: **Dilution refrigerator and two solid helium experiments.**

This figure shows the complete low-temperature apparatus contained inside the vacuum can (VC). The main components of the refrigerator are in blue (above the dashed line), with the major heat sink plates and their temperatures labelled in boldface. Below the mixing chamber plate (below the dashed line) are the two experiments labelled in boldface as well as a few of the physically most prominent objects in the experimental space.

(but not completely to room temperature). The reason for the partial warmup was to pump out the condenser line, which had become gradually blocked over the period of 16 months. We suspected that this block was caused by some oil from the pump getting completely through the traps or by cracked hydrogen from the pump oil; during continuous operation of the DR it was necessary to clean the nitrogen traps about once every 4-5 days of the oil that got through the oil mist filter at the pump output, and when we finally replaced the oil mist filter after the 16 months of operation the filter was completely saturated. Later, a second, homemade oil filter was added in series with the commercial oil mist filter. It consisted of a straight stainless steel tube (12" long  $\times$  3" in diameter) filled with glass wool. It did not improve the frequency at which we needed to clean the nitrogen traps (4-5 days). In the future, if the pump needs to be replaced, we might consider replacing the rotary vane pump with an oil-free pump such as a scroll pump<sup>4</sup> or a scroll pump-backed turbo.

Figure 2.3 shows a schematic of the DR gas panel located on the back wall of the inner acoustic room in A17 Clark. At a few locations in the circuit there are digital gauges<sup>5</sup>, labelled DG1 through DG4, that monitor some important pressures in the circuit. These pressures are

- the pressure in the return line before the nitrogen trap (DG1)
- the pressure in the return line after the nitrogen trap but before the helium trap (DG2)
- the pressure in one of the 29.5 L mixture storage kegs (DG3)
- the pressure in the other storage keg (DG4)

---

<sup>4</sup>Varian, model TriScroll 300/600, pumping speed 15/30  $m^3/h$

<sup>5</sup>SUNX, model DP-101ZA

Table 2.1: Thermometers on the cryostat.

number	location	type
1	1K plate	C-G
2	still plate	RuO <sub>2</sub>
3	ICP	M100Ω
4	mixing chamber plate	Ge
5	gazebo (MXC)	RuO <sub>2</sub>
6	vibration block (MXC)	RuO <sub>2</sub>

Symbols: C-G = carbon-glass, available from Lakeshore. RuO<sub>2</sub>=ruthenium oxide, available from Janis or from Lakeshore. M100Ω = Matsushita carbon resistor, roughly 100Ω, homebuilt and calibrated by M. Yamashita. Ge = germanium, available from Lakeshore. The numbers refer to their labels on the actual cryostat and in the control Labview program in Clark A19.

The output of these four gauges, along a capacitance diaphragm gauge<sup>6</sup> measuring the (room temperature) pot pressure and a Pirani gauge<sup>7</sup> measuring the (room temperature) still pressure, are continuously being tracked by a chart recorder running on the experiment control computer, so that we have a continuous record of the behavior of the six pressures in the DR. The gauge DG1 controls an emergency vent valve<sup>8</sup>, which opens to the kegs if the pressure at the back of the circulation pump gets too high (we usually set the trigger to be 1 bar).

Table 2.1 on page 66 lists the six thermometers in use on our cryostat. On the control computer, a chart recorder is running perpetually and recording the temperatures at the various locations on the cryostat, as for the six pressures discussed above. Temperatures 4, 5, and 6 are redundant and often 4 and 5 are not recorded. The combination of recording the six temperatures and six pressures of the cryostat at all times is an extremely useful way to run a DR and, again, we have Dr. Minoru Yamashita to thank for this paradigm.

---

<sup>6</sup>Pfeiffer, model CMR-261

<sup>7</sup>Leybold, model TR211

<sup>8</sup>ASCO, model 8262G22

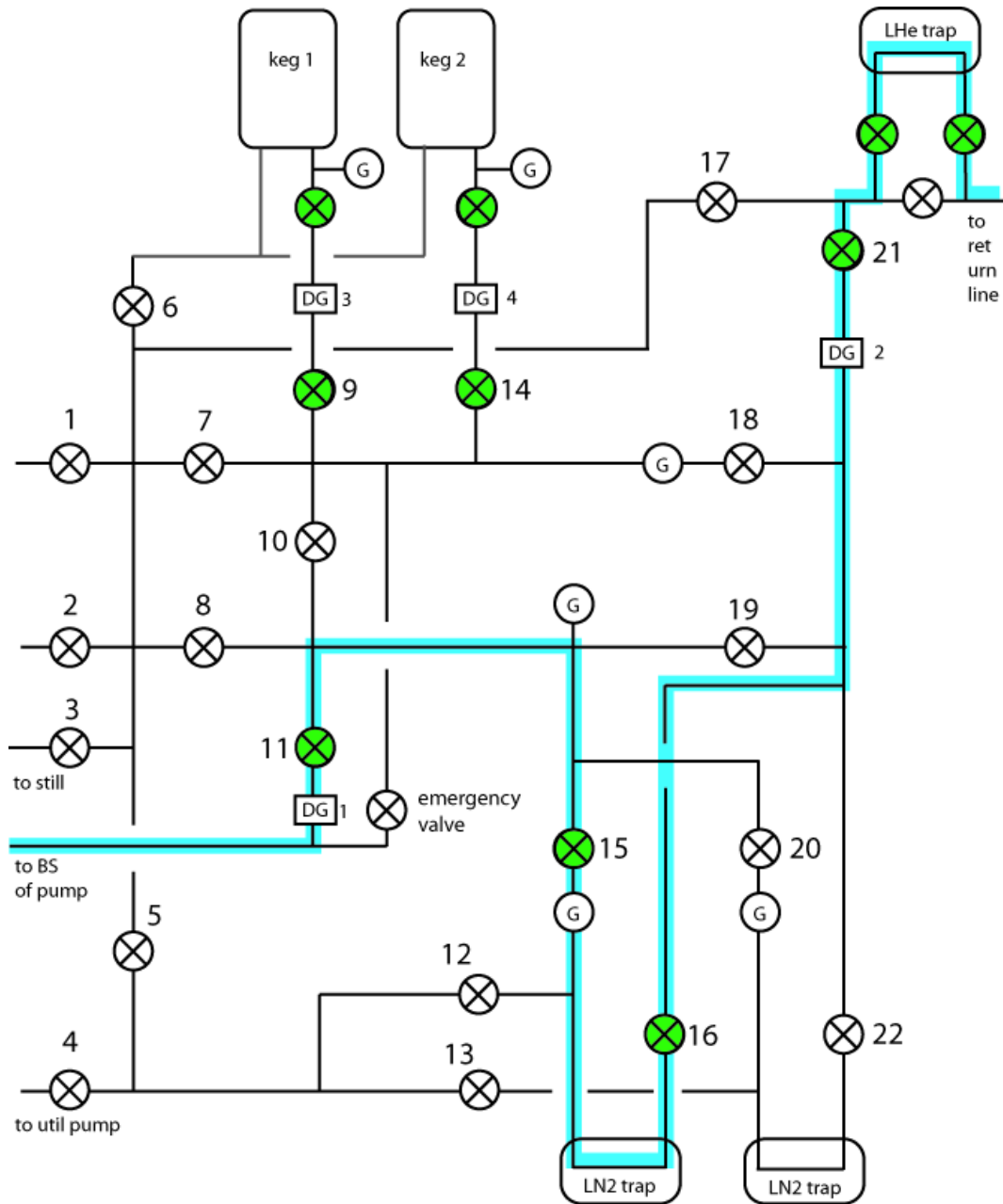


Figure 2.3: **Schematic of DR gas panel.**

The valves are numbered above as they are on the gas panel itself. In the usual operating configuration, the path in blue is the returning path of the  $^3\text{He}$  from the circulation pump to the return line/condenser; the open valves are indicated in green. The  $^3\text{He}$  returns from the pump at the left at the point labelled "to BS [backside] of pump", passes through the nitrogen trap and then the helium trap, and enters the refrigerator at the point labelled "to return line". The emergency valve is controlled by the gauge DG1; if the return pressure gets too high (>1 bar in our operation, but can be adjusted), the emergency valve opens and there is a path back to the kegs.

The refrigerator can be cooled from 4K to its base temperature (10-15 mK) in about a day; the method that we found works very well is described in Appendix A. The typical value for the cooling power of our DR is about  $60 \mu W$  at 100 mK. Information about tests of the condenser impedance are also included in Appendix A.

## 2.2 High-Q Torsional Oscillator

The high-Q torsional oscillator technique is well established and there are several features, both common and esoteric, that will not be discussed in this section. Rather, we will discuss the particular choices we made for our oscillators and some new techniques we developed. The reader interested in a broader treatment of the subject is directed to Gane Ka-Shu Wong's article in [100].

### 2.2.1 Principles

As discussed briefly in 1.3.2, the torsional oscillator (TO) is a very sensitive microbalance capable of measuring changes in the mass of a substance contained within it to about 1 part in  $10^6$ . The basic configuration is a torsion rod of torsion constant  $K$  attached to a container with moment of inertia  $I_{TO}$ . The TO (plus the sample contained within it) is often modelled as a simple harmonic oscillator with a very high Q-factor and so its resonant frequency is proportional to the inverse square root of the total moment of inertia  $I = I_{TO} + I_{sample}$

$$\omega_0 = \sqrt{\frac{K}{I}}$$

and the (angular) amplitude of its motion on resonance is proportional to  $Q$  and to the drive torque  $\Gamma_{ext}$

$$|A(\omega_0)| = \frac{\Gamma_{ext}Q}{I\omega_0^2}. \quad (2.1)$$

The  $Q$  of a typical TO at low temperature is of the order of  $10^6$ , so that very small changes in the mass (and therefore of the moment of inertia) of the sample can be resolved. This is because  $\delta\omega_0/\omega_0 \sim Q^{-1} \sim -2\delta I/I$ .

The drive is usually applied capacitively between a stationary plate and a parallel plate of equal area attached to the moving chassis of the TO. Most TOs used in the past have detected the motion of the TO using a second capacitor pair. Our TO also has a second pair of capacitor plates, which we use for calibration and for detection of motion at relatively high amplitudes of drive and of TO motion. However, our primary method for detecting the motion of the TO is a dc-SQUID-based displacement sensor. The dc-SQUID is an extremely sensitive detector of magnetic flux, and so we couple the motion of a magnet attached to the TO via a stationary pickup coil to the input coil of a dc-SQUID. Details of this scheme and about the calibration of the displacement sensor will be given in a subsequent section.

We operate the TO in a self-resonant drive circuit, in which a feedback circuit maintains the drive at precisely the resonant frequency of the oscillator (the amplitude of the drive is variable). Figure 2.5 shows a schematic of this circuit. The feedback circuit has four main elements. First, the actual signal from TO (either detected by the SQUID or by the capacitors) is filtered and amplified using a low- $Q$  ( $\sim 100$ ) **bandpass filter**<sup>9</sup>. We typically used a 4 Hz-wide frequency band when operating the feedback loop. Second, the filtered signal passes through an

---

<sup>9</sup>Stanford Research Systems, model SR650

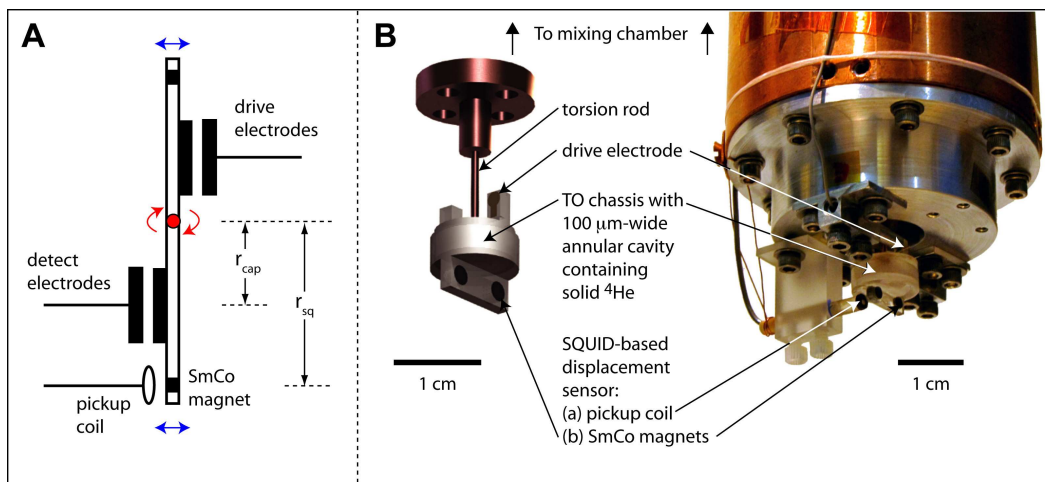


Figure 2.4: **Principle of operation and images of our TO.**

(A) Applying a voltage across the drive capacitor plates causes the TO to rotate about its torsion axis, shown in red perpendicular to the plane of the page, and the resultant linear displacement (shown in blue) can be detected either by a voltage induced on the detect capacitor plates (at a radius  $r_{cap}$ ) or by a magnetic flux induced in the pickup coil by the motion of the SmCo magnet (at a radius  $r_{sq}$ ). In reality,  $r_{sq} < r_{cap}$  (Table 2.3). (B) A schematic (left) and photograph *in situ* (right) of our TO.

analog **comparator** that sets the frequency of the drive by measuring the zero crossings of the TO signal. The output of the comparator is a 22-V peak-to-peak square wave. Third, a **phase shifter** adjusts the phase of the square wave (and therefore of the drive signal) to compensate for electronic phase differences in the circuit. The comparator and phase shifter are both components of a home-made box built by Minoru Yamashita, which we often refer to as the “MY box”. This box also has a dial-controlled analog output that can be used as the drive signal. However, as is more common for automatic control of the drive amplitude, the phase-shifted 22-V square wave is then fed into a **voltage-controlled amplifier (VCA)**, also homebuilt by Minoru Yamashita.

The VCA has four voltage ranges (parameters are shown in Table 2.2) which can be used to drive the oscillator over more than four decades of ac drive am-

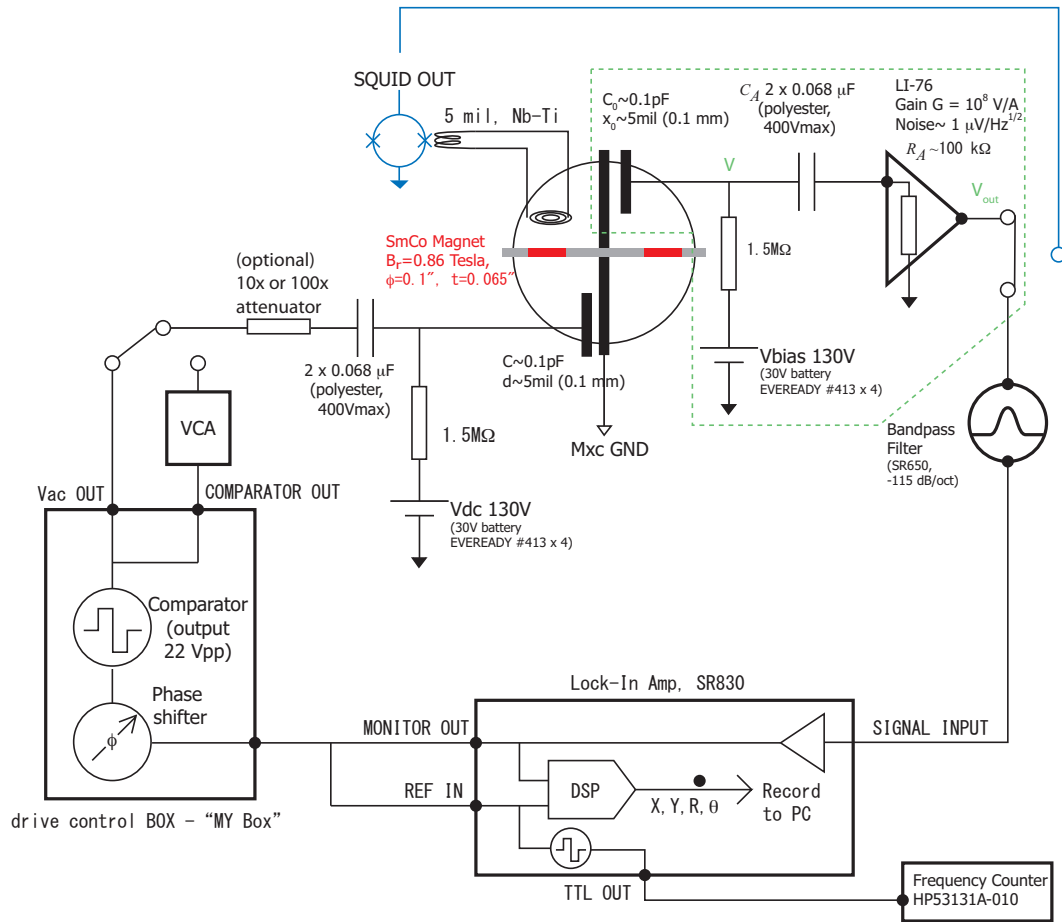


Figure 2.5: **Feedback circuit for self-resonant drive.**

The components contained within the (green) dashed line are the elements of the capacitive detection scheme, discussed in Section 2.2.3.

plitude (from  $V_{ac} = 0.1$  mV to 2.75 V). The drive is biased with a large **dc bias voltage**  $V_{dc}$  to linearize the drive torque in  $V_{ac}$  ( $\Gamma_{ext} \propto V_{ac}V_{dc}$ ), so this also corresponds to four decades of drive torque. However, because of the instability of the lowest drive setting (the signal-to-noise can be 1:1) when driving with the lowest drive torques we often use a higher range and then attenuate the signal with a  $10\times$  or  $100\times$  attenuator at the top of the cryostat. The analog output of the MY box can also be used for the drive signal  $V_{ac}$  from roughly  $\sim 0.1$  mV<sub>pp</sub> to 1 V<sub>pp</sub> ( $V_{pp} \equiv$  peak-to-peak voltage), but has the obvious disadvantage of non-automatic control.

Table 2.2: **Output voltage ranges of VCA.**

output range (mV <sub>pp</sub> )	noise (mV)
26-2750	1
1-577	0.25
0.1-19.5	0.1
0.1-1.1	0.1

(V<sub>pp</sub> ≡ peak-to-peak voltage)

A **lock-in amplifier**<sup>10</sup> is used to measure the signal from the TO, which is a voltage from the SQUID or from the capacitors proportional to the amplitude of oscillation on resonance (Eq. 2.1). Several different signals in the feedback loop can be used as the external reference trigger: the MONITOR OUT (sine-wave) or TTL OUT (0-5V square-wave) signals from the back of the lock-in amplifier, the square wave from the comparator or from the VCA out, or even the signal directly after the bandpass filter. We found that the best choice for the reference, at least for the ringdown experiments of Chapter 5, was the MONITOR OUT signal. Using this signal introduced a constant 2° phase shift between the input TO signal and the reference.

To record the resonant frequency of the oscillator, we measured the TTL OUT from the back of the lock-in amplifier with a high-precision **frequency counter**<sup>11</sup>. The resonant frequency as measured during a free decay did not differ by more than 1 mHz from the value measured while the TO was in the self-resonant drive loop described above.

<sup>10</sup>Stanford Research Systems, model SR830

<sup>11</sup>Agilent, model 53131A

## 2.2.2 SQUID-based Detection Scheme

The main improvement in our torsional oscillator over other TOs was the introduction of a superconducting quantum interference device (SQUID)-based displacement sensor. Such sensors have been used with great success to study aspects of superfluid helium too sensitive to be otherwise detected, such as phase slippage and the Josephson effect in  $^3\text{He}$  and  $^4\text{He}$  [60, 92]. In our experiments, we detect the motion of permanent samarium cobalt (SmCo) magnets attached to the bottom of the TO by sensing the change in magnetic flux through a nearby stationary pickup coil. The pickup coil is in series with an input coil inductively coupled to the loop of a dc-SQUID; the two coils and the wire connecting them form a superconducting loop. When a moving magnet attached to the TO changes the magnetic flux through the pickup coil, a current is generated in the superconducting loop and therefore in the input coil as well. The resultant magnetic flux is detected by the dc-SQUID. The dc-SQUID is operated in a flux-locked loop [37] and therefore generates an output voltage  $V_{sq}$  proportional to the change in flux  $\Delta\phi_{sq}$  in the SQUID loop. In the dc-SQUID we use<sup>12</sup>, there are three ranges of total  $\Delta\phi_{sq}$  that can be tolerated by the feedback loop before it resets: ranges 5, 50 and 500. The numbers refer to the total dynamic range in flux quanta (one flux quantum  $\phi_0 = 2 \times 10^{-15}$  Wb).

When properly shielded from outside sources of magnetic flux, the changes in flux that can be detected by the SQUID are extraordinarily small. The flux sensitivity of the dc-SQUID is of the order of  $10 \mu\phi_0/\sqrt{\text{Hz}}$ . The displacement  $\delta x$  of the magnet is proportional to the output voltage of the dc-SQUID and the

---

<sup>12</sup>Quantum Designs, model 550

proportionality constant is usually called the “sensitivity”  $\eta_{sq}$ :

$$V_{sq} = \eta_{sq} \delta x. \quad (2.2)$$

The sensitivity is a function of both the dc-SQUID circuitry and also the particulars of the coupling between the magnet and the pickup coil. It is determined by the calibration procedure outlined in the next section. A typical value on the most sensitive setting of the dc-SQUID feedback loop (range 5) is  $\eta_{sq}(5) = 1$  V/nm. In the TO experiments, we usually operate using the intermediate setting (range 50) in order to strike a balance between the required displacement sensitivity and the dynamic range of the sensor; a typical value of the sensitivity is  $\eta_{sq}(50) = 0.1$  V/nm. On the most sensitive setting, the displacement noise corresponding to the flux noise quoted above is about  $10^{-14} \text{ m} / \sqrt{\text{Hz}}$ . It is 10 times less sensitive than this on the range 50 setting and 100 times less sensitive on the range 500 setting.

The type of SQUID-based sensor used in the earlier studies noted above also used a superconducting circuit to couple flux changes generated by a moving element into a dc-SQUID loop, but the moving element was not a permanent magnet (Fig. 2.6[B]). In that case, the moving element was a superconducting plane (a few hundreds of nm thick disk of sputtered lead or niobium) that modified the inductance  $L$  of a nearby pickup coil in a (primary) superconducting loop containing a persistent current  $I$ . Since  $\Delta\Phi = 0$  in a superconducting loop, a change in the inductance due to the moving superconducting plane generated a change in the persistent current  $I_1 \rightarrow I_1 + \delta I_1$ , which could be coupled (via a secondary superconducting loop and a secondary persistent current  $I_2$ ) into the dc-SQUID. For more details about this detection scheme, see [89].

Our (permanent magnet) method had advantages over the older (persistent

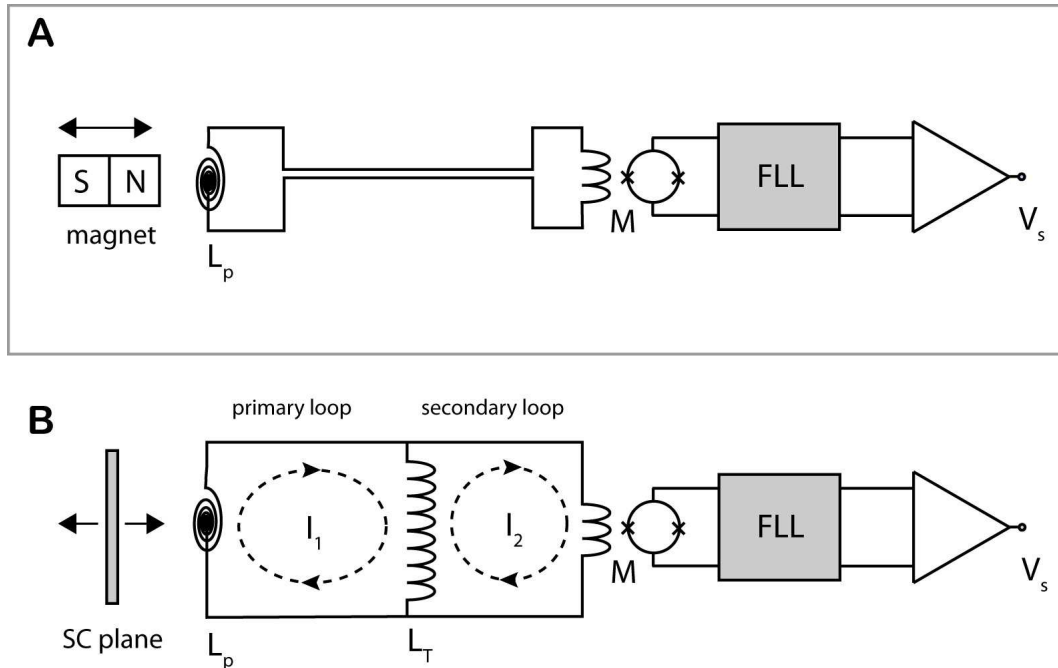


Figure 2.6: **Principle of dc-SQUID-based detection schemes.** (A) Permanent magnet-based scheme. This is the method used for the experiments in this dissertation. (B) Persistent current-based scheme. The flux-locked loop (FLL) is shown schematically.

current) method, but also some notable disadvantages. The advantages are related primarily to the simplicity of our circuit. First, the probability of success of either detection scheme is related to the number of superconducting joints that need to be made between the various superconducting elements in the two circuits. Our scheme has 6, whereas the older scheme has 9, including two 3-way SC joints. Additionally, the SC joints determine the critical current of the primary superconducting loop  $I_c$  and therefore the maximum persistent current  $I_{max} = I_c$  that can be injected into the loop. Since the displacement sensitivity  $\eta$  of the circuit is directly proportional to the injected current, the sensitivity of the displacement sensor can be limited by a single bad joint. The permanent magnet-scheme is much more reliable in this regard with no loss in sensitivity. Second, the injection of the persistent current can be a delicate matter, involv-

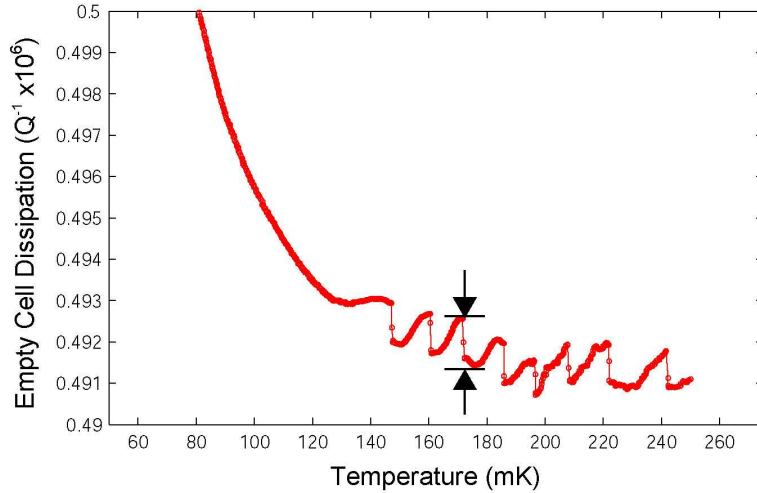


Figure 2.7: **Flux jumps in the SmCo permanent-magnet displacement sensor.** The jumps are shown with  $Q^{-1}$  on the vertical axis for comparison with the scale of the full-cell data, e.g. Fig. 1.6. The full scale in this figure is  $0.01 \times 10^{-6}$  whereas the height of the dissipation peak is roughly  $7 \times 10^{-6}$ . The jumps are extremely small; the equivalent displacement of the change in flux shown between the arrows is  $0.3 \times 10^{-12} m$ . The increase in the empty-cell dissipation as  $T \rightarrow 0$  is minute compared with the size of the dissipation peak.

ing instantaneous decoupling of the 4K superconducting circuit and the 300 K current-injection source via a long movable conduit. Any number of confounding problems can result from moving parts in a bath of helium; the permanent magnet scheme is also free of such complications.

The major disadvantage of our permanent-magnet based scheme is due to a particular and unforeseen property of SmCo magnets at sub-1 K temperatures. Between approximately 150 mK and an unknown upper limit (probably around 1 K) the magnetic field of the permanent magnets is periodically varying in the temperature and hysteretic. This property is shown in Fig. 2.7.

The variations in the field have the character of flux jumps, i.e. sudden changes in the magnetic field of the SmCo magnet that are extremely small. In terms of the displacement sensor, they look like picometer ( $10^{-12} m$ ) changes

in the motion of the torsional oscillator. Another property of the flux jumps was that the period (in temperature) of the flux jumps appeared to decrease with increased velocity of the torsional oscillator. we verified that the jumps did not have to do with the self-resonant circuit by driving the TO off resonance above and below  $f_0$  by  $\pm 50$  Hz. This was the extent of our study of the flux jumps; we have not identified the exact physical nature of this phenomenon.

We were fortunate because most of the phenomena we investigated in solid  $^4\text{He}$  were below 100 mK and were therefore not affected by these flux jumps. The take-home message here is: do not use the SmCo-based magnet scheme if you wish to investigate motion on the picometer scale between 100 mK and 1 K.

### 2.2.3 Capacitor-based Detection Scheme

The classic method of detecting the motion of a torsional oscillator is by using a capacitor pair, one plate fixed and the other attached to the moving TO. The components of this scheme are depicted in Fig. 2.5 enclosed within the dashed green line. A large **dc bias**  $V_{bias}$  is applied across the capacitor and any change in the capacitance (due primarily to the motion of one plate relative to the other) is measured as an ac current by a **current preamplifier**<sup>13</sup>. The input impedance of the current preamplifier should be zero (relative to the large **bias resistor**,  $1.5\text{ M}\Omega$ ) and so when the capacitance changes  $C \rightarrow C + \delta C$  the plates can draw charge with essential no charging time, maintaining the voltage  $V$  at  $V_{bias}$ . This condition, i.e. that  $dV/dt = 0$ , and the assumption that the relative displacement of the plates is  $x(t) = x_0 + \delta x e^{i\omega t}$  leads to an expression for the current

---

<sup>13</sup>NF, model LI-76

$$I = dQ/dt,$$

$$I = CV(\delta x/x_0)\omega e^{i(\omega t + \pi/2)}, \quad (2.3)$$

and therefore for the (amplitude of the) output voltage of the preamplifier:

$$\begin{aligned} V_{out} &= |I(t)| G \\ &\approx C_0 V_{bias} (\delta x/x_0) \omega G. \end{aligned}$$

Here, we have written the capacitance  $C \approx C_0 = \epsilon_0 A x_0^{-1}$ ; this is justified since  $C = \epsilon_0 A x^{-1} = C_0 [1 + (\delta x/x_0) e^{i\omega t}]$  and  $\delta x/x_0 \sim 10^{-5}$ . The gain  $G$  of the preamplifier is  $10^8 \text{ V/A}$ . Although the capacitance  $C_0$  is extremely small (0.16 pF) and is in parallel with a large cable capacitance ( $C_{cable} \sim 200 \text{ pF}$ ), the output of the *current* preamplifier is independent of the cable capacitance (the output of a voltage preamplifier, which has an input impedance  $Z \rightarrow \infty$ , would be degraded by the ratio  $C_0/[C_0 + C_{cable}]$ ). We can compensate for the  $\pi/2$  phase shift (Eq. 2.3) by adjusting the relative phases of the signal and trigger in the lock-in amplifier.

## 2.2.4 Calibration of SQUID- and Capacitor-based Sensors

We know that the angular displacement  $\delta\theta$  of the TO, when driven on resonance, should be proportional to  $Q$  and to the drive torque  $\Gamma_{ext}$  (see Eq. 2.1). This is related to the linear displacement  $\delta x$  of the TO at the distance of the capacitor plates  $r_{cap}$  from the axis of rotation (Fig. 2.4) via  $\delta x \approx r_{cap} \delta\theta$ , since  $r_{cap} \gg \delta x_{cap}$ .

Thus, we have that

$$\begin{aligned}
\delta x &= r_{cap} \frac{Q}{I\omega_0^2} \Gamma_{ext} \\
&= \frac{Q}{I\omega_0^2} r_{cap}^2 F_{ext} \\
&= \frac{Q}{I\omega_0^2} r_{cap}^2 \left( \frac{C_{drive}}{x_{drive}} \right) V_{dc} V_{ac}, \tag{2.4}
\end{aligned}$$

where the external torque was the external force  $F_{ext} = C_{drive} V^2 / 2x_{drive} \approx F_0 + C_{drive} V_{dc} V_{ac} / x_{drive}$  applied at  $r_{cap}$ . The static restoring force  $F_0 = C_{drive} V_{dc}^2 / 2x_{drive}$  contributes a very small change to the spring constant of the torsion rod, of the order of 1 part in  $10^5$ , and so we disregard it in calculations. From the previous section, we found that the output of the capacitive sensor due to a displacement  $\delta x$  at the frequency  $\omega_0$  was

$$V_{out} = \eta_{cap} \delta x. \tag{2.5}$$

$$\eta_{cap} \equiv G\omega_0 \left( \frac{C_0}{x_0} \right) V_{bias}. \tag{2.6}$$

We see that the capacitor output  $V_{out}$  is proportional to the displacement, which is in turn proportional to the ac drive voltage  $V_{ac}$ . We make one more assumption, which is that  $C_{drive}/x_{drive} = C_0/x_0$ ; this is reasonable since the overlap areas of the drive and detect pairs are nearly the same and the capacitors gaps  $x_{drive}$  and  $x_0$  are set carefully and chosen to be the same. Substitution of Eq.2.4 into 2.5 then gives

$$V_{out} = \left[ G \left( \frac{C_0}{x_0} \right)^2 V_{bias} V_{dc} \frac{r_{cap}^2 Q}{I\omega_0} \right] V_{ac}. \tag{2.7}$$

We measure  $V_{out}$  as a function of  $V_{ac}$  and determine the slope  $M$ , which is in square brackets in Eq. 2.7. The quantities that compose  $M$  are shown in Table 2.3 along with how they are determined and typical values for our experiments. We independently measure  $Q$  via a ringdown of the empty TO; the only unknown

Table 2.3: Calibration quantities for SQUID-based TO.

quantity	(typical) value	how determined
$G$	$10^8 \text{ V/A}$	measured
$C_0$	$0.16 \text{ pF}$	Eq. 2.7
$x_0$	$160 \mu\text{m}$	Eq. 2.7
$V_{bias}$	$169 \text{ V}$	measured
$V_{dc}$	$160 \text{ V}$	measured
$I$	$18.9 \text{ g} \cdot \text{mm}^2$	calculated*
$Q$	$10^6$	measured
$r_{cap}$	$4.0 \text{ mm}$	measured
$r_{sq}$	$3.5 \text{ mm}$	measured
$r_{fl}$	$4.5 \text{ mm}$	measured
$\eta_{cap}$	$6 \times 10^{-5} \text{ V/nm}$	Eq. 2.5
$\eta_{sq}(50)$	$0.1 \text{ V/nm}$	calib. against $\eta_{cap}$

These parameters are relevant to all of the experiments reported in this dissertation. \* We use the program SolidWorks to model our torsional oscillators.

quantities are  $C_0$  and  $x_0$ . The quantity  $C_0/x_0$  is determined from  $M$ , and from  $C_0 = \epsilon_0 A x_0^{-1}$  we can determine  $C_0$  and  $x_0$  independently. Substitution of  $C_0/x_0$  into Eq. 2.5 allows us to determine the capacitor sensitivity  $\eta_{cap}$ ; it turns out to be about  $6 \times 10^{-5} \text{ V/nm}$ .

There is a narrow overlap where we can measure both a signal from the capacitors and also from the SQUID; this is how we calibrate the SQUID sensitivity  $\eta_{sq}$  (i.e. output voltage per unit displacement). To estimate the value of  $\eta_{sq}$  in a manner analogous to Eq. 2.6 is difficult. The model of the behavior of the capacitor plates is more accurate and so a simultaneous determination of  $\eta_{cap}$  and  $\eta_{sq}$  is a better method for calibration of the SQUID. Because of their different distances from the axis of rotation (Fig. 2.4), the displacements  $\delta x_{sq}$  of the SQUID sensor and the  $\delta x_{cap}$  of the capacitive sensor are related by a geometric factor, i.e.,  $\delta x_{sq} = (r_{sq}/r_{cap})\delta x_{cap}$ . A similar geometric factor needs to be taken into account when calculating the displacement or velocity of the helium, since it is confined to an annular cavity at a radius  $r_{fl}$  from the axis of rotation. For

the values of  $r_{cap}$ ,  $r_{sq}$  and  $r_{fl}$  see Table 2.3.

## 2.3 Pressure Measurement

We formed all of the helium samples studied in this dissertation using the *blocked capillary* technique. The solid is formed by first creating a high pressure liquid (typically 75 bar) at a temperature greater than the melting temperature  $T_m$  and then cooling the sample down at constant volume. At the first point in the column of helium where  $T < T_m$ , a solid plug forms, likely at the 1K plate where the fill line is heat sunk. The volume of helium below this plug then follows the solid-liquid coexistence (melting) curve and the pressure of the solid volume drops accordingly. When the pressure reaches its final value, the thermodynamic path leaves the melting curve and the solid continues to cool approximately isobarically until it reaches its lowest temperature. A typical thermodynamic path for this procedure is shown in Fig. 2.8. In all of the studies reported in this dissertation, the samples were all formed at pressures above the hcp-bcc triple point to avoid possible complications due to the bcc phase.

We measured the high pressure in the helium gas/liquid/solid manifold with two **high-pressure gauges**. One gauge, the “SETRA”<sup>14</sup>, was at room temperature and monitored the pressure on the high-temperature side of the plug (which remained approximately at the initial liquid pressure of 75 bar) and the other gauge was a home-built capacitance gauge of the Straty-Adams type [111] that measured the pressure of the helium solid directly. Its location on the cryostat is shown in Fig. 2.2; it is thermally at the same location as the helium frozen

---

<sup>14</sup>SETRA, model 206

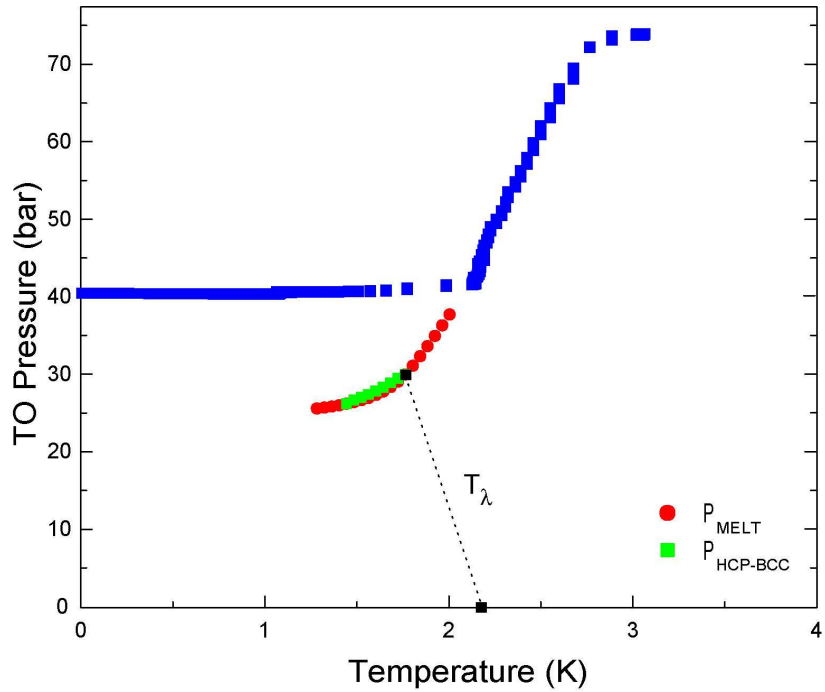


Figure 2.8: **Thermodynamic path of the helium solidification.**

inside the TO. This gauge typically should be retrained each cooldown by applying and then removing a large pressure several times until the effect is reproducible and relatively well-calibrated to the SETRA. The capacitance is measured with an **ac capacitance bridge**<sup>15</sup> and the pressure was initially calibrated to the SETRA gauge.

We found that there was a tendency to melt the plug during transfers and the pressure would drop from its low temperature value (~40 bar) down to the melting curve (25 bar). The remedy for this problem was to install a large ballast volume (75 cc vs ~few cc for the volume available to the helium in the fill line and TO) at room temperature and to form the solid by the procedure above, maintaining 75 bar of gas pressure on the high-temperature side of the plug.

<sup>15</sup>Homebuilt using a ratio transformer (variable inductor), a reference capacitor and a lock-in amplifier. A commercial bridge (such as an Andeen-Hagerling) would work well too.

## CHAPTER 3

### LINEAR RESPONSE OF THE TORSIONAL OSCILLATOR

This chapter will discuss a new formalism for understanding and analyzing the response of the TO to an external torque. The existence of a dissipation peak accompanying the TO frequency shift is difficult to understand in the context of conventional 3D superfluidity and no satisfactory quantitative description of the dissipation peak existed before the work of Nussinov et al. [86], on which much of this chapter is based.

#### 3.1 Linear Response Theory and Rotational Susceptibility

As many authors have pointed out [8, 86, 125], what is measured in the torsional oscillator measurements is not the moment of inertia of the TO-helium system but rather its susceptibility to an external torque  $\Gamma_{ext}$ . In the time domain, the angular displacement of the TO is

$$\left( I_{TO} \frac{d^2}{dt^2} + \gamma_{TO} \frac{d}{dt} + K \right) \theta(t) = \Gamma_{ext}(t) + M(t) \quad (3.1)$$

$$M(t) \equiv \int g(t-t') \theta(t') dt' \quad (3.2)$$

for a linear system invariant under time translation. In this familiar equation,  $I_{TO}$ ,  $\gamma_{TO}$  and  $K$  are the moment of inertia, dissipation and torsion constant, respectively, of the empty TO. For simplicity, we will consider these terms to be temperature-independent for the rest of the discussion in this chapter. The second term on the right-hand side of Eq. 3.1 is sometimes called the “back-action” of the helium on the TO chassis: due to its finite shear modulus the helium exerts a moment  $M(t)$  on the TO. Defining the moment as  $M(t) =$

$\int g(t - t')\theta(t')dt'$  is the most general way within linear response theory of writing this back-action; the exact form of the function  $g$  will depend on how the back-action of the helium is modelled. Formulating the dynamical problem in this way allows the entire temperature dependence of the susceptibility to be included in the back-action term. At this point, it would be prudent to address the validity of using a classical equation of motion to describe the dynamics of a system that is putatively dominated by quantum effects. I will defer discussion of this issue to the end of this section.

Taking the Fourier transform of Eq. 3.1, we find that we can write the angular displacement  $\theta(\omega) = \Gamma_{ext}(\omega)\chi(\omega)$ , where

$$\chi^{-1}(\omega, T) = -I_{TO}\omega^2 - i\gamma_{TO}\omega + K - g(\omega, T), \quad (3.3)$$

and

$$\chi_0^{-1}(\omega) = -I_{TO}\omega^2 - i\gamma_{TO}\omega + K \quad (3.4)$$

is the (temperature-independent) rotational susceptibility of the empty TO, a damped simple harmonic oscillator. In Eq. 3.3, the term describing the helium  $g(\omega, T)$  has a temperature-independent part  $I_{He}\omega^2$  and a temperature-dependent part  $\tilde{g}(\omega, T)$ , so that

$$g(\omega, T) = I_{He}\omega^2 + \tilde{g}(\omega, T). \quad (3.5)$$

We will consider the form of  $\tilde{g}(\omega, T)$  for several models of the behavior of solid helium in the following sections.

The resonant frequency of the system at the lowest temperature is  $\omega_0 = \sqrt{K/I}$ , which is that of a perfectly rigid rotor with moment of inertia  $I = I_{TO} + I_{He}$ . We neglect the small dissipation of the TO  $\gamma_{TO} \sim Q_\infty^{-1}$  in the following because it contributes a correction to the resonant frequency proportional to

$Q_\infty^{-2}$ , which is  $O(10^{-11})$  for the TOs we use. Experimentally, we do not track directly the susceptibility at the fixed frequency  $\omega$ , but rather we measure the small deviation of the resonant frequency  $f(T)$  from its low-temperature, rigid-body value  $f_0 = \omega_0/2\pi$ , as well as the accompanying peak in the dissipation  $Q^{-1}(T)$ . To solve for the resonant frequency and dissipation, one solves for the complex frequency  $\tilde{\omega}$ , which is a pole of the function  $\chi$  and therefore the solution to the equation

$$\chi^{-1}(\tilde{\omega}) = 0.$$

The resonant frequency and dissipation are then related to the real and imaginary parts of  $\tilde{\omega}$  via

$$f(T) = \Re[\tilde{\omega}]/2\pi \quad \text{and} \quad Q^{-1}(T) = |2\Im[\tilde{\omega}]/\Re[\tilde{\omega}]|. \quad (3.6)$$

The simplest example is to solve for the resonant frequency and dissipation of the empty TO. Setting Eq. 3.4 to zero at  $\tilde{\omega}_{empty}$ , one finds that

$$\tilde{\omega}_{empty} = \sqrt{\frac{K}{I_{TO}}} \left( 1 - \frac{\gamma_{TO}^2}{KI_{TO}} \right)^{1/2} - i \frac{\gamma_{TO}}{2I_{TO}}$$

which (using Eq. 3.6) gives the following familiar results for a the dissipation  $Q^{-1}$  and resonant frequency  $\omega_R$  of a simple harmonic oscillator ( $\omega_0 \equiv \sqrt{K/I_{TO}}$ ):

$$Q^{-1} \approx \frac{\gamma_{TO}/I_{TO}}{\omega_0} \quad \omega_R = \omega_0 \sqrt{1 - (2Q)^{-2}}. \quad (3.7)$$

I will now address the question of whether it is valid to use a classical equation of motion to describe the rotational susceptibility of solid  $^4\text{He}$ , a material in which quantum behavior plays such a large role in determining its properties. The numbers used here are for the system we studied, but are representative of typical parameters of the TOs employed by the many groups studying solid  $^4\text{He}$ . The effective change in the moment of inertia of the solid  $^4\text{He}$  as it

would be interpreted from  $\Delta I / (I_{He} + I_{TO}) = \Delta f^{max} / 2f_0$ , whether by a super-solid mechanism (NCRIf) or by a moment  $M(t)$  exerted by the  $^4\text{He}$  on the TO, is of the order of 0.01% to 20%. Our sample has a volume  $V = 8.5 \times 10^{-3} \text{ cm}^3$  and a molar volume of about  $20 \text{ cm}^3$  (40 bar,  $0.2 \text{ g/cm}^3$ ). It is confined to a thin annulus of radius  $r = 4.5 \text{ mm}$  and therefore, approximating the  $\sim 10^{20}$  atoms of  $^4\text{He}$  to form a continuous solid of constant density, the sample has a moment of inertia  $I_{He} = mr^2$ . Putting in the numbers, we find that the *minimum* total angular momentum change of the solid  $^4\text{He}$  (using the figure 0.01%) would be of the order of  $10^{24}\hbar$ . Smaller changes than this can certainly be resolved, but even so the rotational quantum numbers of the  $^4\text{He}$  atoms are so large that, according to the correspondence principle, our system is in the classical limit.

If the microscopic nature of the back-action term (or the change in the moment of inertia) is quantum-mechanical but the TO experiments can be well described by Eq. 3.1, it would be more appropriate to say that we are working in a semiclassical limit. An example of such a treatment of TO experiments is the Kosterlitz-Thouless transition in 2-D  $^4\text{He}$  films [25], the frequency and dissipation data of which was fit beautifully by the dynamical theory of Ambegaokar, Halperin, Nelson and Siggia [3, 4]. In these classic papers, they use a Langevin equation for the diffusive motion of quantized vortices and bound vortex pairs to calculate the additional dissipation (and resultant TO frequency shift) as the  $^4\text{He}$  undergoes the K-T transition.

### 3.1.1 Susceptibility Based on Superfluid Decoupling

In the picture of the supersolid transition as a simple decoupling of the superfluid component from the inertia of the rest of the solid, the “back-action” term isn’t really a back-action at all; the relevant term in the rotational susceptibility (Eq. 3.3) would be

$$g_{ss}(\omega, T) = -I_{He} \left( 1 - \frac{\rho_s(T)}{\rho} \right) \omega^2. \quad (3.8)$$

where  $\rho_s/\rho$  is the superfluid fraction. Insofar as Eq. 3.3 is the correct description of the supersolid dynamics, Eq. 3.8 fails to completely describe the data because there is no provision for the dissipation peak  $Q^{-1}$ , that is, there is no added dissipation in the system due to existence of the superfluid. The correct model of the behavior of the solid helium will first and foremost have to address this issue.

### 3.1.2 Debye Susceptibility

A simple and important example of a non-trivial  $\chi^{-1}(\omega, T)$  that qualitatively captures the temperature dependence of  $f$  and of  $Q^{-1}$  is the Debye form

$$\chi^{-1}(\omega, T) = -I\omega^2 - i\gamma_{TO}\omega + K - \frac{g_0}{1 - i\omega\tau(T)}, \quad (3.9)$$

a form that is quite familiar from many other branches of physics. In this equation we have written  $I = I_{TO} + I_{He}$  and we neglect the intrinsic dissipation of the helium. This form represents the overdamped response of an (unspecified) set of excitations within the  $^4\text{He}$  solid that has a resonant response when the frequency of motion of the TO ( $\omega$ ) matches the rate of relaxation of the excitations

( $\tau^{-1}$ ). It is worth deriving the expressions for the resonant frequency and dissipation in order to see how the two are intimately related in this general picture of the response of the torsional oscillator.

We set Eq. 3.9 equal to zero at  $\omega = \tilde{\omega}$  and we see that it becomes a cubic equation for  $\tilde{\omega}$ . It can be solved exactly, but the exact solution is not illuminating; we can achieve a clearer result by recognizing that the last term in Eq. 3.9, the contribution to  $\chi$  from the solid helium, is a small perturbation to the total susceptibility. We therefore consider a form of  $\tilde{\omega}$  that is linearized about the low-temperature solution  $\omega_0 = \sqrt{K/I}$ ,

$$\tilde{\omega} = \omega_0 + ix + y, \quad |ix + y| \ll \omega_0, \quad (3.10)$$

and expand to linear order in  $x$  and  $y$ , giving

$$\begin{aligned} \tilde{\omega}^2 &= \omega_0^2 + 2\omega_0 y + 2i\omega_0 x \\ \tilde{\omega}^3 &= \omega_0^3 + 3\omega_0^2 y + 3i\omega_0^2 x. \end{aligned} \quad (3.11)$$

If we substitute these expressions into the cubic equation for  $\tilde{\omega}$ , we end up with two coupled equations (for the real and imaginary parts of  $\chi^{-1}(\tilde{\omega}) = 0$ ) in two unknowns ( $x$  and  $y$ ). Solving for  $x$  and  $y$  we find that

$$\begin{aligned} x &= -\frac{g_0}{2I\omega_0} \left( \frac{\omega_0\tau}{1 + \omega_0^2\tau^2} \right) = -\frac{g_0}{2I\omega_0} \Im \left( \frac{1}{1 - i\omega_0\tau} \right) \\ y &= -\frac{g_0}{2I\omega_0} \left( \frac{1}{1 + \omega_0^2\tau^2} \right) = -\frac{g_0}{2I\omega_0} \Re \left( \frac{1}{1 - i\omega_0\tau} \right). \end{aligned} \quad (3.12)$$

Using these expressions we can write our observables, the resonant frequency and the dissipation, using Eqs. 3.6 and 3.10, and we find that

$$f(T) = f_0 - \frac{1}{4\pi I\omega_0} \Re \left( \frac{g_0}{1 - i\omega_0\tau} \right) \quad (3.13)$$

and

$$Q^{-1}(T) = Q_\infty^{-1} + \frac{1}{I\omega_0^2} \Im \left( \frac{g_0}{1 - i\omega_0\tau} \right). \quad (3.14)$$

We see that within this Debye model of the susceptibility,  $f$  and  $Q^{-1}$  are related in a simple way to the real and imaginary parts of  $g(\omega, T)$ . In the last line, we added back the contribution to the dissipation from  $\gamma_{TO} = I_{TO}\omega_0 Q_\infty^{-1}$ . The Debye model has the simple property that

$$\frac{\Delta Q^{-1}(T)}{\Delta f(T)/f_0} = 2\omega_0\tau(T), \quad (3.15)$$

where  $\Delta Q^{-1}(T) = Q^{-1}(T) - Q_\infty^{-1}$  and  $\Delta f(T) = f_0 - f(T)$ . Since  $Q^{-1}$  has a peak when  $\omega\tau(T^*) = 1$ , we know that the ratio of the amplitude of the dissipation peak  $\Delta Q^{-1}(T^*)$  to the total (fractional) frequency shift  $\Delta f^{max}/f_0 = (f_0 - f_\infty)/f_0$  is always in a fixed ratio for the Debye model, regardless of the other parameters. This also suggests that Eq. 3.15 can be used to *measure*  $\tau(T)$ .

We are used to thinking about response functions such as  $\chi$  in the frequency domain, so that as the measurement frequency is swept through the response or relaxation time  $\tau$ , there is a change in the real part of  $\chi$  and an accompanying peak in  $\chi$ . The change in  $\Re[\chi(\omega)]$  and  $\Im[\chi(\omega)]$  are related, for example, via the Kramers-Kronig relations: if one quantity is known in the entire frequency range over which the change in that quantity is taking place, the other quantity is completely determined. In the case of the experiments described in Chapters 4 and 5, instead of sweeping the measurement frequency  $\omega$ , we fix the measurement frequency and sweep the *relaxation time*  $\tau(T)$  by changing the temperature. The relationship of the resonant frequency and dissipation to  $\Re[\chi(T)]$  and  $\Im[\chi(T)]$  is dependent on the model we use for  $\chi$ , but in the case of the Debye susceptibility (and of any model that has a single relaxation time  $\tau$  for a given  $\omega$  and  $T$  - see e.g. 3.1.4 but not 3.1.3) the relationship has the simple form given by Eqs. 3.13 and 3.14.

In order to capture qualitatively the behavior of the frequency and dissipa-

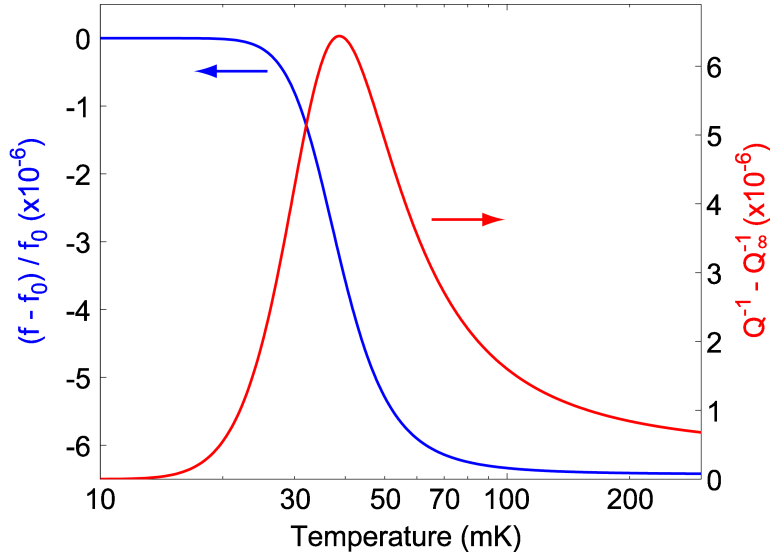


Figure 3.1: **Frequency shift**  $(f - f_0)/f_0$  and **dissipation shift**  $Q^{-1} - Q_{\infty}^{-1}$ . These curves are calculated by Eqs. 3.13 and 3.14.

tion by using Eqs. 3.13 and 3.14 we also need a model for the relaxation time  $\tau(T)$ . It is clear that  $\tau(T)$  should be monotonically decreasing as  $T \rightarrow \infty$ . A very simple model that has this behavior is the Arrhenius form

$$\tau(T) = \tau_0 \exp(\Delta/k_B T), \quad (3.16)$$

which represents the activated dynamics of excitations frozen out at temperatures that are small compared to  $\Delta/k_B$ . Figure 3.1 shows the prediction of Eqs. 3.13 and 3.14 with  $\tau(T)$  given by Eq. 3.16.

### 3.1.3 Glassy Susceptibility

Viscous liquids close to the glass transition have response functions that exhibit non-exponential relaxation in their response functions, in contrast to homogeneous liquids, which generally respond with a single relaxation time [27, 44, 110]. The response function,  $F(t)$ , might be, for example, the polarization

in response to an electric field, or the strain in response to an applied stress; for a comprehensive list of examples, see [27]. The classic form for  $F(t)$  is the “stretched exponential” or Kohlrausch-Williams-Watts (KWW) form

$$F(t) = \exp(-t/\tau)^\theta \quad (3.17)$$

which, for  $\theta < 1$ , represents the response of the system at a wider distribution of frequencies. The limit  $\theta = 1$  corresponds to the Debye relaxation. If one transforms the KWW form to the frequency domain, this distribution becomes explicit, but equally effective at capturing the idea of a distribution of modes is the form first used by Davidson and Cole to fit the complex dielectric constant  $\epsilon^*$  of several polar liquids [40]<sup>1</sup>:

$$\frac{\epsilon^*(\omega) - \epsilon(\infty)}{\epsilon(0) - \epsilon(\infty)} = \frac{1}{(1 - i\omega\tau)^\beta}. \quad (3.18)$$

Here,  $\beta$  plays the role of the “stretching exponent” that  $\theta$  did in Eq. 3.17. Taking their cue from this successful fitting form, Nussinov et al. proposed a form of the rotational susceptibility of the TO-helium system if the helium exhibited glassy behavior, i.e. a response at a distribution of relaxation times:

$$\chi^{-1}(\omega, T) = -I\omega^2 - i\gamma_{TO}\omega + K - \frac{g_0}{[1 - i\omega\tau(T)]^\beta}. \quad (3.19)$$

In the theory of glasses, the response time  $\tau$  often takes the Vogel-Tamman-Fulcher form  $\tau(T) = \tau_0 \exp[D/(T - T_0)]$  (see [110]), which is identical to the Arrhenius form for  $T_0 = 0$ .

---

<sup>1</sup>In fact, a different form was used ten years earlier by Cole and Cole [38]. That form was  $(1 - [i\omega\tau]^{1-\alpha})^{-1}$  instead of the Davidson-Cole form  $(1 - i\omega\tau)^{-\beta}$

### 3.1.4 Viscoelastic Susceptibility

Building on the ideas of Nussinov et al., Yoo and Dorsey modeled the solid helium inside a cylindrical TO (of radius  $R$  and height  $h$ ) as a viscoelastic solid, i.e. an elastic solid with internal friction [125]. They pointed out that the “back-action” term could be due to the finite shear modulus of the helium and the internal stress fields created when the acceleration of the helium was not in phase with the motion of the outer wall of the container. They used the simplest viscoelastic model, a single spring (the shear modulus  $\mu_0$ ) in series with a single dashpot (the viscosity  $\eta$ ),

$$\mu(\omega) = \mu_0 - i\omega\eta = \mu_0(1 - i\omega\tau),$$

with  $\tau = \eta/\mu_0$  the single relaxation time scale in the problem. This is known as the Kelvin-Voigt model. By solving the wave equation for the strain field of the helium inside the container and considering the resultant stress tensor, they were able to derive the moment exerted by the solid on the container

$$M(t) \approx -I_{He}\omega^2 \left(1 + \frac{k^2 R^2}{24}\right) \theta_0 e^{-i\omega t}$$

where  $k = \omega/c_T$ , with  $c_T = \rho/\mu(\omega)$  the speed of transverse sound,  $I_{He}$  the moment of inertia of the helium, and  $\theta_0 e^{-i\omega t}$  the motion of the oscillator in the absence of the helium. The term  $I_{He}\omega^2(k^2 R^2/24)$  is the (small) deviation of the moment from its rigid-body value  $I_{He}\omega^2$ . This result can be put in the form of a rotational susceptibility:

$$\chi^{-1}(\omega, T) = -I\omega^2 - i\gamma_{TO}\omega + K - \frac{\rho R^2 I_{He} F(h/R)\omega^4}{24\mu_0 [1 - i\omega\tau(T)]}. \quad (3.20)$$

The function  $F(h/R)$  includes the finite size effect of the container (but not torsional standing waves generated by the top and bottom of the container) and is

of order unity. The rest of the temperature-independent part of the back-action term can be rearranged to read

$$\frac{\rho R^2 I_{He} \omega^4}{\mu_0} = v_{rim} \left( \frac{v_{rim}}{c_T} \right) I_{He} \omega^2, \quad (3.21)$$

where  $v_{rim} = \omega R$  is the rim velocity of the TO. Since  $c_T \gg v_{rim}$ , we are justified in assuming that the back-action term is small.

If one solves this model for the resonant frequency and dissipation of the TO, one finds that it has the same dependence on temperature as the Debye model and the same ratio  $|\Delta Q^{-1}| / (\Delta f^{max} / f_0)$ . The striking difference is in the frequency dependence of this model. Whereas the Debye model had no frequency dependence in the denominator of  $\tilde{g}(\omega, T)$  (see Eq. 3.5), in the viscoelastic model one has  $\tilde{g}(\omega) \sim \omega^4 / (1 - i\omega\tau)$ . Yoo and Dorsey argued that a nonzero power of  $\omega$  was necessary in the numerator of  $\tilde{g}(\omega)$  because otherwise as  $\omega \rightarrow 0$ ,  $\tilde{g} \rightarrow \text{constant}$ , which would represent an unphysical shift in the torsion constant  $K$ . This strong function of frequency in the back-action term  $\tilde{g}$  means that in a frequency-dependent study of the rotational susceptibility, it should be straightforward to distinguish this model from, say, the Debye model.

### 3.1.5 Two-Level Systems in a Real Glassy TO

In torsional oscillators specifically constructed to study glasses (such as  $\text{SiO}_2$ ) at low temperatures, the standard tunnelling model (STM) has been successful at predicting the acoustic and thermal properties of those materials over a wide range of temperatures [10, 93, 126]. An excellent summary of this model and the relevance to the behavior of glassy TOs is in the dissertation of Andrew Feferman [49]. The model is based on a collection of two-level defects in a crystal

(basically an ensemble of systems each described by a double-well potential) that can tunnel between the two energy states and interact in various ways with the phonon bath. A single one of these two-level systems (TLSs) is characterized by an asymmetry parameter  $\Delta$  that measures the difference in the depth of the two energy wells and a parameter for tunneling between the two wells  $\Delta_0$ , and experimental data are generally well described by a distribution of the energy splittings  $E = \sqrt{\Delta^2 + \Delta_0^2}$  and  $\Delta_0$  given by

$$P(E, \Delta_0) = \frac{P_0}{\Delta_0 \sqrt{1 - (\Delta_0/E)^2}}.$$

This model predicts the linear term in the specific heat referred to in Sec. 1.4.4. It is the interaction of the ensemble of the TLSs with the phonons in the material that determines the acoustic properties, and in particular the frequency shift  $\delta f/f$  and internal friction  $Q^{-1}$  of a torsional oscillator constructed of the material. The details are well beyond the scope of this dissertation, but I wanted to mention two relevant points. First, there two main types of interaction between TLSs and phonons, *resonant* processes and *relaxational* processes. The latter are characterized by a relaxation time for the TLSs to return to thermal equilibrium after perturbation by interaction with phonons, and this (temperature-dependent) relaxation time  $\tau_{rel}$  is just the contribution to  $Q_{rel}^{-1}$  of the relaxational processes divided by their contribution to the frequency shift  $2(\delta f_{rel}/f)$ :

$$\tau_{rel} = \frac{Q_{rel}^{-1}}{2(\delta f_{rel}/f)}, \quad \tau_{rel} \propto \frac{E^3}{\Delta^3(1 - \Delta^2/E^2)} \tanh\left(\frac{E}{2k_B T}\right).$$

The second point is that the overall temperature dependence of  $\delta f/f$  and  $Q^{-1}$  seem to be quite different from what we measure in the solid  $^4\text{He}$ . There is a change in the two quantities over several decades of temperature, due to dominance of different resonant and relaxational processes in different temperature regimes. Because of this obviously large discrepancy, we do not attempt to fit our data to this model.

## 3.2 Fitting to the Various Models

In this section, we fit some of the models to the equilibrium values of the frequency shift and dissipation predicted by a few models described above.

### 3.2.1 Debye Susceptibility

The fits of the frequency and dissipation data of Fig. 1.6 to the predictions of the Debye model (Eqs. 3.13 and 3.14) are shown in Fig. 3.2. The procedure was to fit the dissipation peak and then use the parameters of the dissipation fit to then fit the frequency shift. For this fit, a simple activated Arrhenius form was used, i.e. a single relaxation time of the form  $\tau = \tau_0 \exp(\Delta/k_B T)$ . With this model, the fit has three parameters, the strength of the back-action  $g_0$ , the time scale for the relaxation  $\tau_0$ , and the activation energy  $\Delta$ . With these three parameters, we obtain a satisfactory fit of the dissipation peak with the parameters  $g_0 = 3.17 \mu\text{N/m}$ ,  $\tau_0 = 9.48 \mu\text{s}$ , and  $\Delta/k_B = 0.131 \text{ K}$ . The most striking thing about the subsequent fit using these parameters to the frequency shift is that the strength  $g_0$  seems to be far too inadequate to account for its magnitude, only predicting about 15% of the total frequency shift.

This discrepancy between the dissipation and the frequency shift (when modelled with a Debye susceptibility) seems to be a fairly general feature of the observed behavior in the majority of solid  $^4\text{He}$ -TO systems studied [65], although the “missing frequency shift” seems to vary anywhere from no missing shift up to 99% [74, 101]. It seems that the converse could also be argued: that the frequency shift from the Debye model would predict a dissipation peak that was

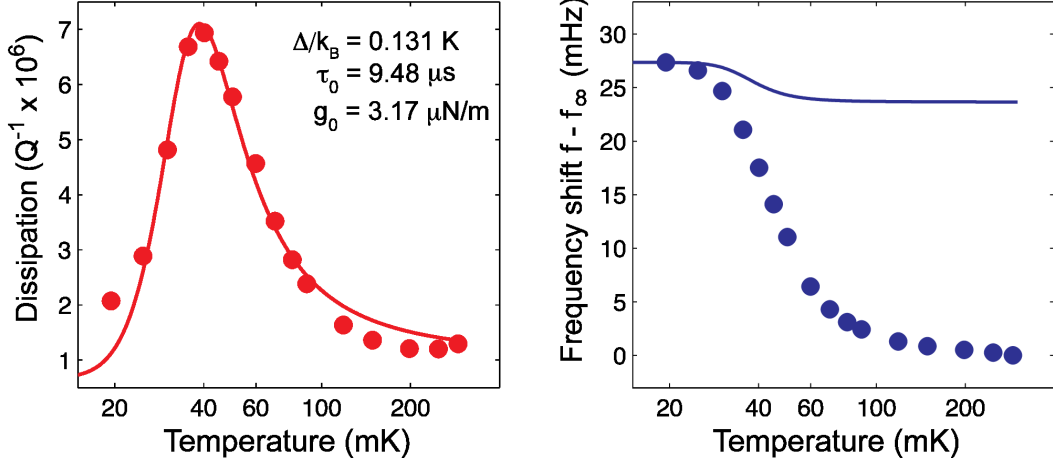


Figure 3.2: **Fits to Debye susceptibility with Arrhenius activation.**

The circles are the data of Fig. 1.6 and the lines are fits to Eqs. 3.13 and 3.14, with  $\tau(T) = \tau_0 \exp(\Delta/k_B T)$ . The (three) fit parameters are  $\tau_0 = 9.48$   $\mu$ s,  $\Delta/k_B = 0.131$  K, and  $g_0 = 3.17$   $\mu$ N/m.

far larger than the observed behavior. However, the fact that a superfluid transition can produce a frequency shift (via the change in the moment of inertia of the TO) with little or no change in the intrinsic dissipation has led some researchers (including us) to conjecture that the “missing frequency shift” might be superfluid in nature and that the coincidence of the excitation freeze-out (at  $T^*$ ) and the superfluid transition implies that freezing the excitations somehow facilitates superfluidity in the system.

It should also be noted that a fit to the viscoelastic susceptibility (Eq. 3.20) would have the same numerical result as the Debye susceptibility if we identify the back-action strength  $g_0$  with the coefficient  $\rho R^2 I_{He} F(h/R) \omega_0^4 / 24 \mu_0$  of the back-action term in the viscoelastic model<sup>2</sup>. The best way to distinguish these two models would be to study the rotational susceptibility as a function of  $\omega$ , since the back-action term in the viscoelastic model has a strong frequency dependence in the numerator ( $\propto \omega^4$ ). The relationship between the internal

<sup>2</sup>For a more transparent form of this coefficient, see Eq. 3.21.

stress fields and the vacancies that may be responsible for the superfluid-like behavior is fairly well established and the elastic nature of the helium solid may play some role in the promotion of superfluidity while the solid is subjected to oscillating stress.

We will now examine the validity of using the Arrhenius form for the relaxation time  $\tau(T)$ , within the Debye and viscoelastic models. There are two approaches, which we shall name after the people that first suggested these ideas to us.

1. *Balatsky approach* [17]. Equation 3.15 showed that the relaxation time could be calculated by dividing the dissipation by the fractional frequency shift, i.e.

$$\omega_0\tau(T) = \frac{\Delta Q^{-1}(T)}{2\Delta f(T)/f_0} \quad (3.22)$$

2. *Dorsey approach* [125]. One can invert Eq. 3.14 to obtain  $\tau(T)$  from the  $Q^{-1}(T)$ ; another way of writing Eq. 3.14 is

$$\Delta Q^{-1}(T) = \frac{2A\omega_0\tau}{1 + (\omega_0\tau)^2}$$

(this defines  $A$  as the dissipation peak height on resonance:  $\Delta Q^{-1}(T^*) = A$ ). We can just invert this to get

$$\omega_0\tau(T) = \frac{A}{\Delta Q^{-1}(T)} \left( 1 \pm \sqrt{1 - \left[ \frac{\Delta Q^{-1}(T)}{A} \right]^2} \right) \quad (3.23)$$

where the sign in front of the square root is chosen so that  $\tau$  is a monotonically decreasing function of temperature. The quantity  $\Delta Q^{-1}(T)/A$  ranges from 0 to 1 in the temperature range of interest and therefore the square root cannot be expanded.

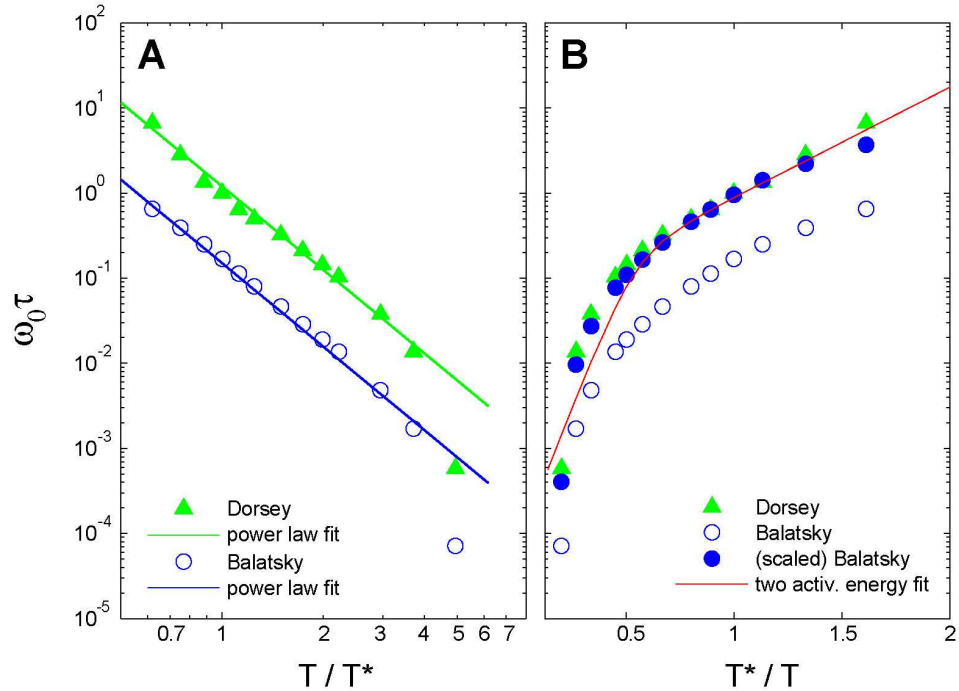


Figure 3.3: **Two methods for obtaining  $\tau(T)$  from the experimental data.** (A) The data on log-log axes. Power law fits yield  $\tau \sim T^{-3.2}$  (for both methods). (B) The data on Arrhenius axes (log vs.  $1/T$ ). They appear to be equally well fit by an Arrhenius law  $\tau \sim \exp(\Delta/T)$  for  $T < 2T^*$ , but they deviate strongly above that temperature.

These two models are shown in Figs. 3.3(A) and (B). In (A), the data are presented on log-log axes, and in (B) they appear on Arrhenius axes (log vs.  $1/T$ ). The data appear to be equally well fit at low temperatures (below  $2T^*$ ) by both power laws and by activated behavior, but the validity of the power law fit seems to extend slightly further, out to  $\sim 4T^*$ . Fitting to the Dorsey and Balatsky methods yields  $\tau \sim T^{-3.2}$  for both methods. The physical implications of having power law behavior vs. activated behavior are significant and will be discussed more in Chapter 5.

The temperature dependence is qualitatively similar for both methods, but the Dorsey result appears to give be more correct in the sense that  $\omega_0 \tau = 1$  when  $T = T^*$ . The reason that the Balatsky method underestimates the magnitude of

the relaxation time is the same reason that there appears to be a frequency shift that is too large by a factor of 85/15; scaling the Balatsky result for  $\tau$  by this factor collapses the result nicely on top of the Dorsey result and emphasizes the similar temperature dependence. Dorsey suggests that this temperature dependence might be explained by a relaxation time with two energies  $E_1$  and  $E_2$ :

$$\tau(T) = s_0 \frac{\exp(E_1/T)}{1 + \delta \exp(E_2/T)} \quad (3.24)$$

A fit to this function of the Dorsey  $\tau(T)$  is also shown in Fig. 3.3. The parameters are  $E_1 = 0.6$  K,  $E_2 = 0.48$  K,  $\delta = 1.6 \times 10^{-3}$  and  $s_0 = 2 \times 10^{-8}$  s. The authors do not give a physical interpretation of  $E_1$  and  $E_2$ , but at low temperatures, Eq. 3.24 reduces to  $\tau(T) = (s_0/\delta) \exp([E_1 - E_2]/T)$  and the parameters are in good agreement with those used in the fits in Fig. 3.2. This result shows that the Arrhenius model for the relaxation time appears to be (self-consistently) correct, at least for temperatures less than about  $2T^*$  and therefore well within the region of interest where the changes in the TO resonant frequency and dissipation occur. A model of the relaxation time  $\tau \sim T^{-\alpha}$ , with  $\alpha = 3.2$ , also fits the data well for an even larger temperature range ( $T = 0$  to  $T \approx 4T^*$ ).

### 3.2.2 Glassy Susceptibility

The glassy susceptibility given by Eq. 3.19 has a distribution of relaxation times, controlled by the exponent  $\beta$ , and therefore does not admit a simple relationship between the resonant frequency and  $\Re[\chi^{-1}]$  and between the dissipation and  $\Im[\chi^{-1}]$  as for the susceptibilities having a single relaxation time  $\tau$ . If one attempts to solve Eq. 3.19 for the poles of  $\tilde{\omega} \approx \omega_0 + ix + y$  in the manner illustrated by Eqs. 3.10-3.14, one finds that the expressions for the real and imag-

inary parts of  $\tilde{\omega}$  are nonlinearly coupled and therefore no closed solution for  $f(T)$  [ $Q^{-1}(T)$ ] exists in terms of only  $\Re[g_{gl}]$  ( $\Im[g_{gl}]$ ) as it does for  $g_{Debye}$  (The glassy back-action term  $g_{gl}$  is the last term in Eq. 3.19). For example, setting the imaginary part to zero, one finds that

$$x = y \tan \left\{ \beta \tan^{-1} \left[ \frac{(\omega_0 + y)\tau}{1 + x\tau} \right] \right\},$$

which (to first order in  $x$  and  $y$ ) reduces to the Debye result  $x = \omega_0\tau y$  when  $\beta = 1$ . (The expression for the real part is much more complicated). The back-action term can be written in the form

$$\begin{aligned} g_{gl} &= \frac{g_0}{(1 - i\omega\tau)^\beta} \\ &= \frac{g_0}{(1 - \omega^2\tau^2)^{\beta/2}} \left[ \cos \left( \beta \tan^{-1}(\omega\tau) \right) + i \left( \sin \beta \tan^{-1}(\omega\tau) \right) \right] \end{aligned} \quad (3.25)$$

The real and imaginary parts of this susceptibility are plotted in Fig. 3.4.

Although to properly fit the data to the glassy susceptibility, it is necessary to solve numerically for the real and imaginary parts of  $\chi^{-1}[\tilde{\omega}] = 0$ , we can make a few general observations about the properties of this susceptibility. First, the total frequency shift from low temperature to high temperature is only controlled by the parameter  $g_0$ , as with the Debye susceptibility ( $\beta = 1$ ). The height of the dissipation peak, on the other hand, falls with increasing  $\beta$ . This is not surprising, since for the Debye susceptibility the dissipation peak is proportional to  $\omega\tau$ , and so the effect of increasing  $\beta$  is to distribute the response over a wider range of relaxation times and therefore to widen the peak and diminish its height. Graf et al. show for the glassy susceptibility (Eq. 3.19) that

$$\frac{|\Delta Q^{-1}|}{\Delta f^{max}/f_0} \approx 2 \tan(\beta\pi/4)$$

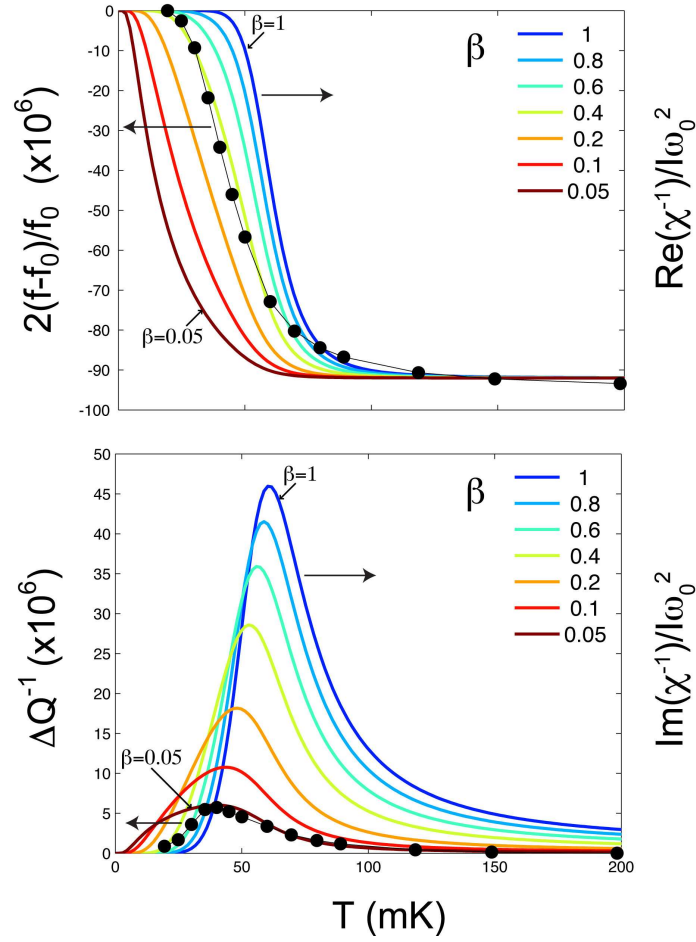


**Figure 3.4: Real and imaginary parts of glassy susceptibility.**

The colored curves are the real and imaginary parts of Eq. 3.25 (divided by  $I\omega_0^2$ ) for a particular choice of  $\tau = \tau_0 \exp(\Delta/T)$  and various values of  $\beta \leq 1$ . For comparison, the data from Fig. 1.6 (and 3.2) are included. The particular combination  $2(f - f_0)/f_0$  makes Eqs. 3.13 and 3.14 symmetric by making the prefactors of  $\Re[(1 - i\omega_0\tau)^{-1}]$  and  $\Im[(1 - i\omega_0\tau)^{-1}]$  both equal to  $1/I\omega_0^2$ . Although the frequency data seem to align with the yellow curve ( $\beta = 0.4$ ) it should be emphasized that for a different choice of the parameters  $\tau_0$  and  $\Delta$ , the frequency data can be made to fit a different value of  $\beta$ . The point is that in principle one can find a susceptibility for which the ratio  $|\Delta Q^{-1}| / (\Delta f^{max} / f_0)$  matches that of the TO data by changing  $\beta$ ; in our case the experimentally observed  $|\Delta Q^{-1}| / (\Delta f^{max} / f_0)$  is matched by the  $\beta = 0.05$  pair of curves (dark red), although the precise temperature dependence of  $f$  and  $Q^{-1}$  are not well described by a susceptibility with  $\beta = 0.05$ .

which ranges from 0 (for  $\beta \rightarrow 0$ ) to 2 (for  $\beta = 1$ ) [51]. The point is that one can find a  $\beta$  such that the the correct ratio  $|\Delta Q^{-1}| / (\Delta f^{max} / f_0)$  is satisfied for any particular experimental pair of curves  $f(T)$  and  $Q^{-1}(T)$ . The wide distribution of results has a natural interpretation in terms of different values of the distribution  $\beta$  achieved by different sample preparations. Specific fits to the data are not performed in this dissertation, but a forthcoming work by Graf et al. [51] finds satisfactory fits of the TO data (of several groups, including ours) to the glassy susceptibility 3.1.3, which they call the “Davidson-Cole” form, as well as satisfactory fits to the alternative “Cole-Cole” form  $g_{gl} = (1 - [i\omega\tau]^\alpha)^{-1}$ .

### 3.3 Summary and Discussion

This chapter introduced a useful formalism for treating the temperature dependence of the TO results, namely the idea of a linear response function (or rotational susceptibility) that described the relationship of the complex angular response  $\theta(\omega)$  to the drive torque  $\Gamma_{ext}(\omega)$ . The temperature dependence of the behavior of the helium inside the TO could all be understood in terms of a “back-action” term  $g(\omega, T)$  in the (inverse) susceptibility. A simple model of this back-action, the Debye susceptibility  $g_{Debye} = g_0(1 - i\omega\tau)^{-1}$  can qualitatively capture the temperature dependence of the TO resonant frequency shift and the dissipation; a more physically appealing model, the viscoelastic model  $g_{VE} = C\omega^4(1 - i\omega\tau)^{-1}$ , is mathematically equivalent to the Debye model in the linear approximation leading to the expressions for  $f(T)$  and  $Q^{-1}(T)$  (Eqs. 3.13 and 3.14) and therefore draws the same conclusions. Both models suffer from the same problem: the prediction for the dissipation peak  $|\Delta Q^{-1}|$  is far too small to account for the total frequency shift  $\Delta f^{max}$ , since both observables are

controlled by the constant  $g_0 (C\omega_0^4)$  in the Debye (viscoelastic) model. In both models, however, one can extract the temperature dependence of the relaxation time  $\tau(T)$  regardless of the discrepancy; for the data used to fit in this section it appears to be equally accounted for by a power law  $\tau \sim T^{-3.2}$  and by an Arrhenius law  $\tau \sim \exp(0.131/T)$  (K).

The discrepancy has notably been addressed by Graf et al. [52, 51] (and earlier by the same researchers in [86]), who proposed a glassy susceptibility  $g_{gl} = g_0(1 - i\omega\tau)^{-\beta}$  having a distribution of relaxation times  $\tau$  controlled by the exponent  $\beta$ . In this case, the ratio  $|\Delta Q^{-1}| / (\Delta f^{max} / f_0) \approx 2 \tan(\beta\pi/4)$  and so can be made arbitrarily small for suitable choice of  $\beta$ . Another proposal that deals with the discrepancy has been made by Huse and Khandker [65], who also attributed the discrepancy to inhomogeneity but couched their answer in terms of the “vortex liquid” model of Anderson. Their equivalent of the disorder parameter  $\beta$  was a putative distribution of *local* transitions from the normal solid to the vortex liquid state; integrated over the whole sample this could be captured by a distribution of transition temperatures  $T_c$  and result in a broadening of the dissipation peak.

Both of these models deal with disorder by subsuming the dependence into a phenomenological parameter. A third model that can deal with this discrepancy is a Debye model describing the freezing transition of excitations of the crystal (i.e. the response at slower and slower  $\tau(T)$  as the temperature is lowered), which transition controls a second degree of freedom - the global superfluid stiffness. The superfluid contribution to the TO frequency shift would have no accompanying dissipation, thereby accounting for the discrepancy in  $|\Delta Q^{-1}| / (\Delta f^{max} / f_0)$ , and its transition temperature would appear to coincide

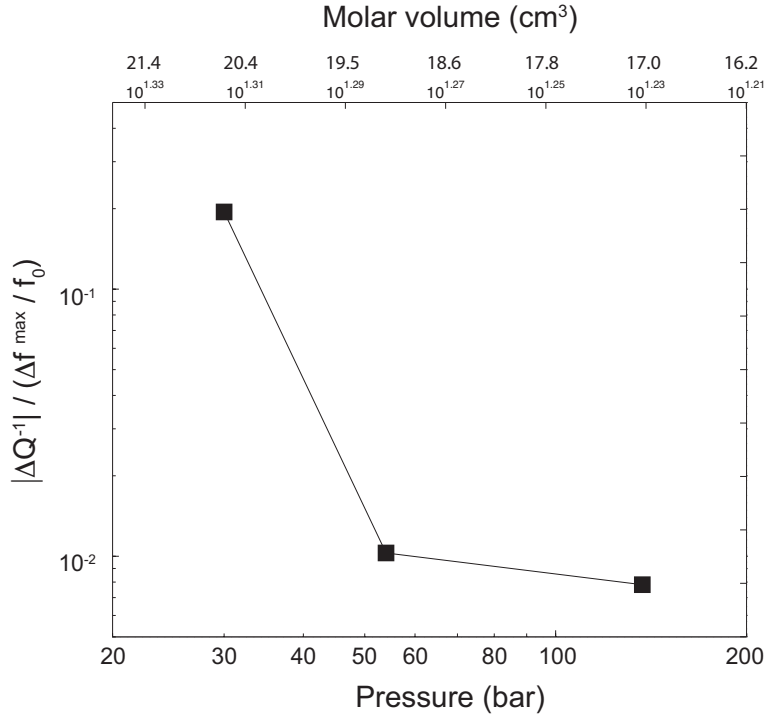


Figure 3.5: **Dependence of the ratio  $|\Delta Q^{-1}| / (\Delta f^{\text{max}} / f_0)$  on hydrostatic pressure and molar volume.**

This figure is derived from data in [74].

with that of the freezing transition precisely because it is the freezing transition that controls when the superfluid component establishes phase coherence in the whole  $^4\text{He}$ . The validity of any one of these models needs to be established by further experiments.

As a final note, no comprehensive studies of the dependence of the ratio

$$|\Delta Q^{-1}| / (\Delta f^{\text{max}} / f_0)$$

on the experimentally-accessible parameters exist to date. However, one piece of evidence can be gleaned from an early paper by Kim and Chan on the pressure dependence of NCRI [74]. I noticed that the ratio  $|\Delta Q^{-1}| / (\Delta f^{\text{max}} / f_0)$  decreases with increasing hydrostatic pressure, a result I plot in Fig. 3.5. On its own, the frequency shift alone  $\Delta f^{\text{max}}$  appears to be *uncorrelated* with the

pressure. In the Debye + superfluid model, the interpretation would be that at higher pressures, there would be a larger superfluid component relative to the Debye contribution to  $\Delta f^{max}$ . In the picture of [96], the existence of gapless vacancies is related to the internal stresses of the helium crystal, and if the superfluid component in this model is of the Andreev-Lifshitz-Chester type, this observation might be the first connection between the superfluid component [in this case deduced from  $|\Delta Q^{-1}| / (\Delta f^{max} / f_0)$ ] and a controllable effect on the stress fields in the crystal.

## CHAPTER 4

### GLASSY DYNAMICS OF SOLID $^4\text{He}$

This chapter describes two experiments that were designed to elucidate the complex dynamics of the low-temperature state of solid  $^4\text{He}$ . One point that every researcher in this field agrees on is the essential role that disorder will play in the eventual explanation of the behavior of supersolid  $^4\text{He}$ . This disorder can be introduced in many ways, as discussed at length in Chapter 1, including the way in which the sample is prepared. As shown by Rittner and Reppy [102], the magnitude of the TO frequency shift was dependent on how rapidly the sample was cooled from the high-pressure liquid, and that the signal could be reduced (and even eliminated) by careful annealing. To make a connection with the various theories, one would like to know what type of disorder was introduced during the formation of the solid. Crystal dislocations had been shown to support gapless vacancy creation and thereby to play a possible role in an Andreev-Lifshitz-Chester type of supersolid. However, in addition to the reduction of the TO frequency shift, the effect of annealing was shown by Rittner and Reppy (and also by Grigor'ev et al. [56]) to cause a simultaneous reduction of the pressure of the sample, an effect much too large to be explained only by the annealing of defects. Grigor'ev proposed that large glassy, disordered regions might have been formed during the quench cooling of the sample, possibly in a jamming-type transition. At the same time, path-integral Monte Carlo simulations showed that off-diagonal long-ranged order (ODLRO) might be present in the same type of quench-cooled samples, which in the simulations also showed glassy regions [29]. A complementary analytical result showed that the existence of such a "superglass" could be understood by a mapping from a classical system known to undergo a jamming transition to a quantum bosonic many-

body state known to support ODLRO.

Glasses are disordered, but disorder does not necessarily imply that what we are dealing with is a glass. How can we make the distinction? One definition of a glass is a liquid that flows on a time scales much longer than that of the laboratory. In the case of supercooled liquids, when the temperature is lowered rapidly enough the molecules cannot adequately sample the configuration space in the available time allowed by the rapid cooling rate and thus the supercooled liquid appears frozen on the laboratory time scale, although it continues to sample all configurations (none of which, statistically speaking, is the crystalline ground state). The glass is essentially trapped in one liquid-like configuration. By analogy, it is plausible that we can treat the disorder in the helium crystal as a (mobile) ensemble of excitations, perhaps a tangle of vortices or dislocation lines, or the relative motion of grains or disordered regions, that can freeze as the temperature is lowered. An exploration of the relaxation dynamics of the helium solid as  $T \rightarrow 0$  would allow one to investigate how this putative ensemble of excitations samples its own configuration space.

In the first experiment, we stepped the temperature down in fixed 5 mK steps from well above the supersolid transition to the lowest attainable temperature and measured the relaxation of the resonant frequency and the dissipation as the system came into thermal and mechanical equilibrium. We found that the frequency and dissipation of the oscillator continued to relax well after the mixing chamber thermometer, well-coupled to the solid helium, arrived at its equilibrium temperature, and we found that the characteristic relaxation times for  $f$  and  $Q^{-1}$  increased identically and dramatically as the temperature was lowered. In the second experiment, inspired by the complex dynamics revealed

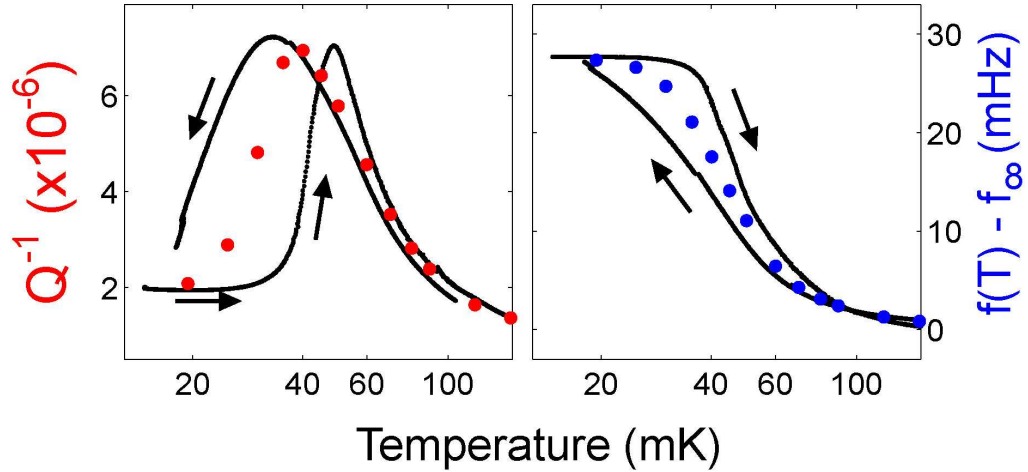


Figure 4.1: **Temperature sweep rate-dependent traces  $f(T)$  and  $Q^{-1}(T)$ .** The black arrows show the direction of the temperature change for the warming and cooling curves. In the limit of sweeping the temperature infinitely slowly the warming and cooling curves converge to the colored data, which are the same data as in Fig. 1.6.

by the step-cooling experiment, we began with the system at its lowest temperature and measured the frequency and dissipation when the system was abruptly heated. The behavior of these two observables on time scales short compared to the relaxation times of experiment #1 reveal a highly non-trivial relationship between  $f(t, T)$  and  $Q^{-1}(t, T)$ . We discuss the results of these experiments in the context of the proposed glassy and superglassy phases of solid  $^4\text{He}$ .

## 4.1 Preliminaries

In addition to the many theoretical and experimental results that motivated our study of the relaxation dynamics, an observation of our own encouraged us to pursue this work. This was our observation of different traces  $f(T)$  and  $Q^{-1}(T)$  when we cooled the system versus when we warmed the system from base temperature, shown in Fig. 4.1. We noticed that the warming and cooling curves began to differ roughly coincident with the onset of the supersolid signal and

we decided to investigate the relaxation times in a systematic way. In Fig. 4.1, as expected, the warming and cooling curves enclose the infinite-time curves shown by the colored dots, which represent the traces for a warming or cooling rate  $\rightarrow \infty$ . They are actually the same data as in Fig. 3.2 and were taken after waiting at a given temperature for a time  $t \gg \tau_{f,Q}$ , where  $\tau_f = \tau_f(T)$  and  $\tau_Q = \tau_Q(T)$  are the temperature-dependent relaxation times for the frequency and dissipation that we measure in the following experiments. The difference in the warming and cooling curves becomes pronounced for temperatures  $T \lesssim T^*$ , but is in fact detectable above this temperature and in the frequency curve the difference is already apparent at about 70 mK.

## 4.2 Experiment #1: Step-Cooling of TO-<sup>4</sup>He

### 4.2.1 Methods

In the first experiment, we measure the relaxation of the resonant frequency and dissipation of the TO containing solid helium after decreasing the temperature in a series of steps, from about 150 mK to the lowest temperatures we can achieve (10 mK). A schematic of this experiment is shown in Fig. 4.2(A). First, the temperature is reduced, typically in a 5 mK step (larger at higher temperatures) toward a new target temperature  $T_{eq}$ . We use a heater mounted to the mixing chamber whose output is controlled using a commercial PID (proportional-integral-derivative) feedback loop<sup>1</sup> to control the mixing chamber temperature precisely. To reach a new target temperature, we allow the system to cool freely

---

<sup>1</sup>Lakeshore, model 370

using the cooling power of the dilution refrigerator and then turn on the feedback loop when the temperature gets close to the target temperature  $T_{eq}$ . Typical temperature traces for this procedure are shown in Fig. 4.2(B). We expect that the solid  $^4\text{He}$  is in good thermal contact with the mixing chamber because of the strong contact with the BeCu walls of the torsion rod and especially with a sintered-silver heat exchanger, whose location on the cryostat is shown in Fig. 2.2.

We monitor the frequency and the dissipation during the temperature relaxation for  $t < t_{eq}$ , the time at which the mixing chamber comes into thermal equilibrium, denoted by a (green) filled circle in Figs. 4.2(A) and (B) and 4.3. We then we record the subsequent behavior of  $f(t, T_{eq})$  and  $Q^{-1}(t, T_{eq})$  for up to four hours after  $t_{eq}$ .

## 4.2.2 Results

The results of the step-cooling experiment are shown in Fig. 4.3 for seven representative temperatures. For ease of comparison between temperatures, both the frequency and dissipation traces at temperature  $T_{eq}$  have been normalized by their total changes as the temperature is changed from  $T_i$  to  $T_{i+1} \equiv T_{eq}$ , i.e. the Y-axis in Fig. 4.3(a) is defined by

$$\delta f(t) = \frac{f(t, T) - f(0, T_i)}{f(\infty, T_{eq}) - f(0, T_i)}$$

and in Fig. 4.3(b) the Y-axis is

$$\delta Q^{-1}(t) = \frac{Q^{-1}(t, T) - Q^{-1}(0, T_i)}{Q^{-1}(\infty, T_{eq}) - Q^{-1}(0, T_i)}.$$

Here,  $\infty$  means the longest time after the temperature has been changed. The curves are offset by 5000 seconds on the X-axis for clarity, and the final tem-

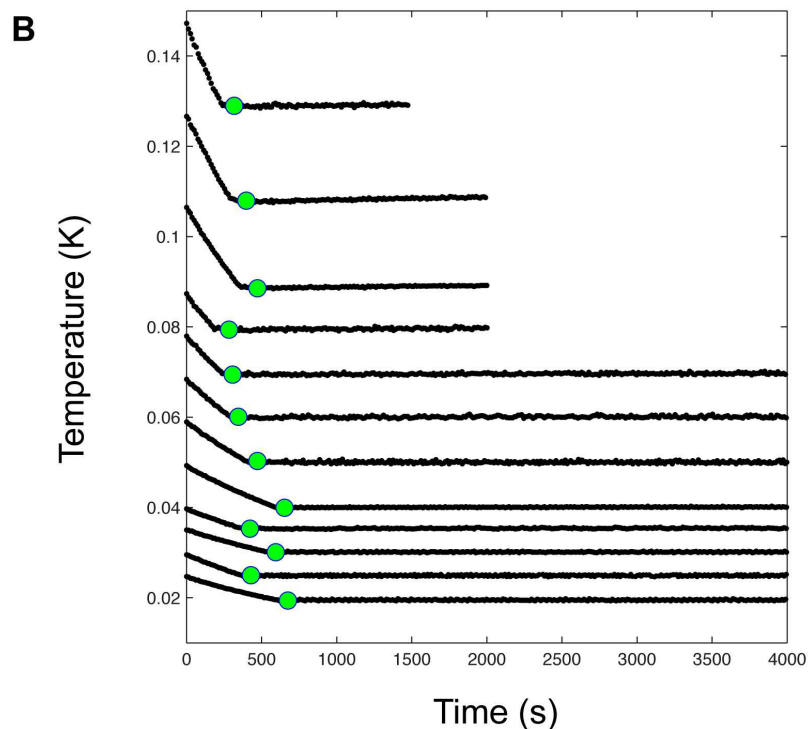
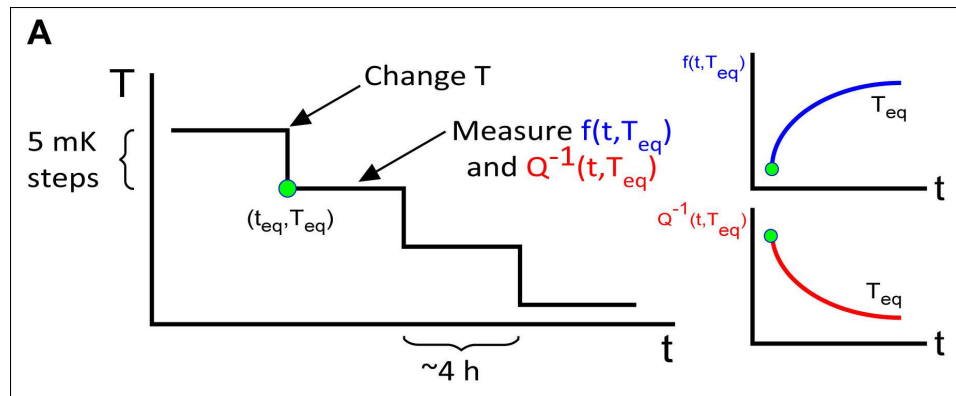


Figure 4.2: **Step-cooling experiment.**

(A) Procedure. The pair of axes to the left shows the protocol we use for stepping down the temperature. The two pairs of axes to the right show schematics of the relaxations in frequency  $f(t, T_{eq})$  and dissipation  $Q^{-1}(t, T_{eq})$  we measure after the mixing chamber comes into equilibrium. (B) Temperature traces for one series of experiments, shown for the first 4000 seconds of the relaxation.  $t_{eq}$ , the time at which the mixing chamber temperature comes into equilibrium, is shown with a (green) filled circle in (A) and (B), and is typically a few hundred seconds after the target temperature  $T_{eq}$  is changed at  $t = 0$ .

perature  $T_{eq}$  associated with each curve is increasing from left to right. There are a few features immediately apparent from both Figs. 4.3(a) and (b). The first feature is that each curve is naturally divided into two parts, the first for  $t < t_{eq}$  before the mixing chamber comes into thermal equilibrium (before the green dot), and the second for  $t > t_{eq}$  when the mixing chamber temperature has equilibrated at  $T_{eq}$  (after the green dot). For the  $t < t_{eq}$  part of the curve, the two quantities  $f$  and  $Q^{-1}$  change at relatively fast rates and appear to respond instantaneously to the changing mixing-chamber temperature. This “fast relaxation” continues until the temperature stabilizes at  $T_{eq}$ . The surprising part is the subsequent “slow relaxation” for  $t > t_{eq}$ . For  $T_{eq} < T^*$  ( $\sim 60$  mK), the frequency and dissipation then continue to relax for several thousand seconds *after* the mixing chamber temperature has come into equilibrium [compare Fig. 4.2(B)]. Note that the dissipation relaxation curves invert for  $T < T^*$  (i.e. for 30.2 mK and 19.6 mK) because  $dQ^{-1}/dT$  changes sign.

It also appears from Fig. 4.3 that the characteristic time for this subsequent relaxation is lengthening as the temperature is lowered, reaching  $\sim 10000$  seconds at the lowest temperature (this curve, taken at roughly 10 mK, is not shown in Fig. 4.3 because it comes from another sample measured when the base temperature of the refrigerator was lower). The characteristic relaxation times for the frequency and for the dissipation,  $\tau_f$  and  $\tau_Q$  respectively, are shown schematically in Fig. 4.3.

To quantify this characteristic time, we fit an exponential form to the curves for  $t > t_{eq}$  and find that this portion of the curves is well fit by an exponential form. The precise form of the fitting functions are  $\delta f(t) = C_1 + C_2 \exp[-(t - t_{eq})/\tau_f]$  for the frequency and  $\delta Q^{-1}(t) = C_3 + C_4 \exp[-(t - t_{eq})/\tau_Q]$  for the dis-

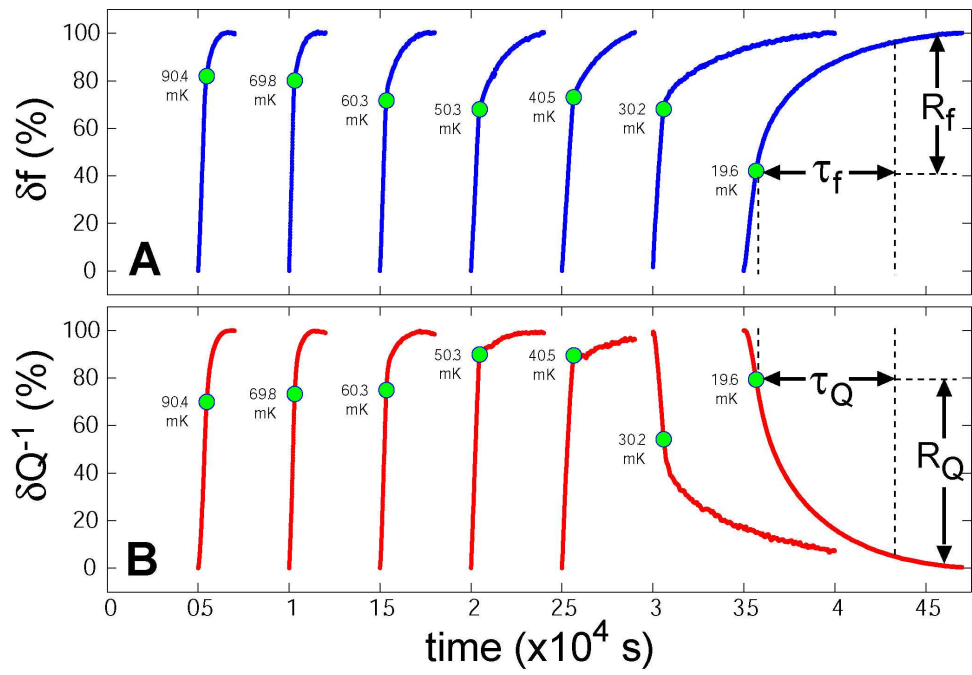


Figure 4.3: Results of step-cooling experiment.

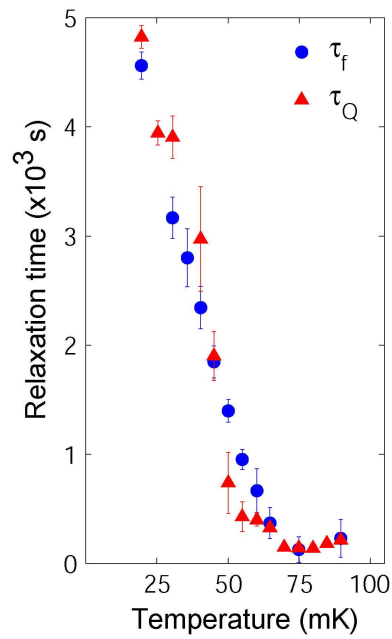


Figure 4.4: Relaxation time for frequency and dissipation.

sipation, where  $C_1 \dots C_4$  are temperature-dependent constants and  $\tau_f = \tau_f(T)$  and  $\tau_Q = \tau_Q(T)$  are the temperature-dependent relaxation times for the frequency and dissipation. These time constants, measured independently for the frequency and dissipation, are shown in Fig. 4.4. The two time constants appear to have the identical temperature dependences which lengthen as the temperature is decreased. Below about 30 mK, there are complications resulting from the thermal relaxation of the Stycast cell [Fig. 4.11(B)] and we can no longer definitively say that the relaxations below this temperature are due only to the mechanical relaxation of the solid  $^4\text{He}$ .

Another feature of the relaxation curves in Fig. 4.3 is that the fraction of each curve relaxing at the slower rate (i.e. the proportion of the curve relaxing for  $t > t_{eq}$  to that relaxing for  $t < t_{eq}$ ) appears to be largest at the lowest temperatures. This fraction is labelled  $R_f$  for the frequency and  $R_Q$  for the dissipation in Fig. 4.3; measurements of these quantities are shown as a function of temperature in Fig. 4.5.  $R_f(T)$  starts out at less than 20% at 110 mK but increases to about 55% at 19.6 mK.  $R_Q(T)$  starts at about 40% at 110 mK, dips down to less than 10% at 50.3 mK and 40.5 mK, close to the dissipation peak, and then increases to 70% at 19.6 mK.

### 4.3 Experiment #2: Abrupt Warming of TO- $^4\text{He}$

In the previous section, we revealed the onset of ultraslow dynamics upon cooling of the solid helium from high temperatures ( $\sim 200$  mK). That experiment measured the dynamical response to a small change in one of the parameters of the experiment, namely the temperature. In the next experiment, we take a

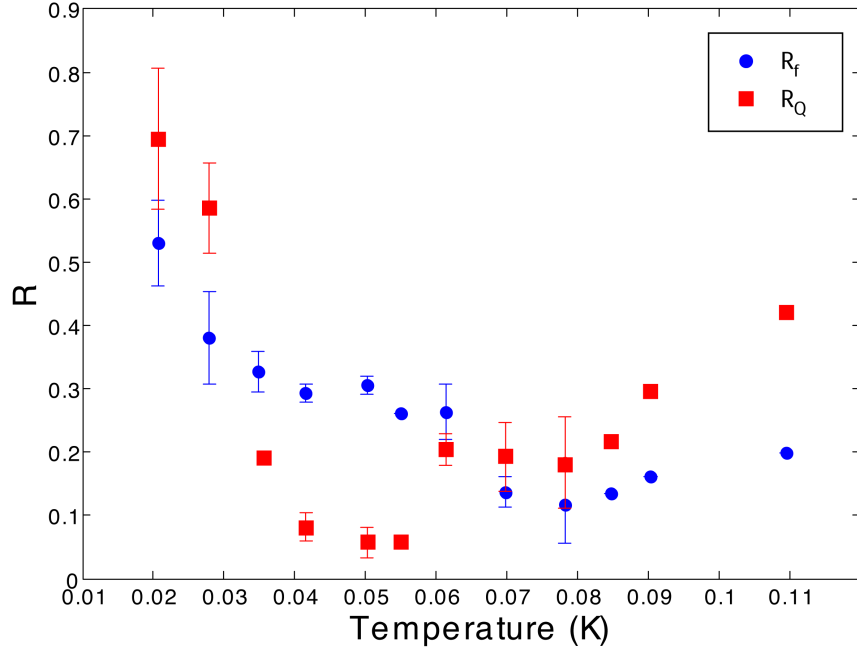


Figure 4.5: Fraction of relaxation traces ( $R_f$  and  $R_Q$ ) relaxing at slower rate.

different approach: we study the dynamics of the formation of the  $T > 0$  state as it emerges from its  $T \rightarrow 0$  ground state, so we change the temperature by a large amount from the base temperature and resolve the dynamics on time scales ( $\sim$ seconds) short compared to those in Fig. 4.4 but still long compared to  $\omega_0^{-1}$ . In principle what we want to observe is non-equilibrium versions of the frequency-dissipation pair of curves. We know from Chapter 3 that there is an intimate relation between the two quantities and that a very useful way of characterizing the relation is with the rotational susceptibility  $\chi^{-1}(\omega, T)$ , for which one can write down various models that contain the frequency and temperature dependence [Eqs. (3.19) and (3.20), for example].

### 4.3.1 Methods

The experiment we perform is shown schematically in Fig. 4.6. We wait for  $\sim 6$  hours at the base temperature of the dilution refrigerator (about 16 mK when we did this experiment). Then at  $t = 0$  we turn on the mixing-chamber heater and warm the mixing chamber until it reaches its first target temperature  $T_{eq}^{(1)}$ . The mixing chamber temperature comes into equilibrium at  $t_{eq}^{(1)}$  seconds after the heat is turned on and the temperature controller does an effective job of stabilizing the temperature at  $T_{eq}^{(1)}$  with a time constant of a few seconds. As with the first experiment, we then record the relaxation of the resonant frequency  $f(t, T_{eq}^{(1)})$  and the dissipation  $D(t, T_{eq}^{(1)})$  for many thousands of seconds after the mixing chamber comes into thermal equilibrium (at the [green] filled circle  $t_{eq}$ ). We then allow the refrigerator to cool back down to its base temperature and remain there for another  $\sim 6$  h before repeating the experiment again for a second target temperature  $T_{eq}^{(2)}$ . Repeating this for a large sequence of temperatures  $T_{eq}^{(1)} \dots T_{eq}^{(N)}$  allows us to map out the whole of the  $f(t, T)$  and  $D(t, T)$  surfaces created as the  $T > 0$  “supersolid” state forms from its ground state.

### 4.3.2 Results

These surfaces are shown in a more intuitive way in Fig. 4.7(A) and (B), as the time evolution of the frequency-dissipation pair of curves (or, equivalently, the rotational susceptibility) as they relax towards equilibrium. Perhaps it is easiest to imagine preparing an ensemble of  $N$  identical TO-solid  $^4\text{He}$  systems and then rapidly heating the  $i$ th system to a final temperature  $T_{eq}^{(i)}$ , where  $T_{eq}^{(1)} \dots T_{eq}^{(N)}$  is from 16  $\dots$  100 mK in Fig. 4.7. We time the heating of each system so that the

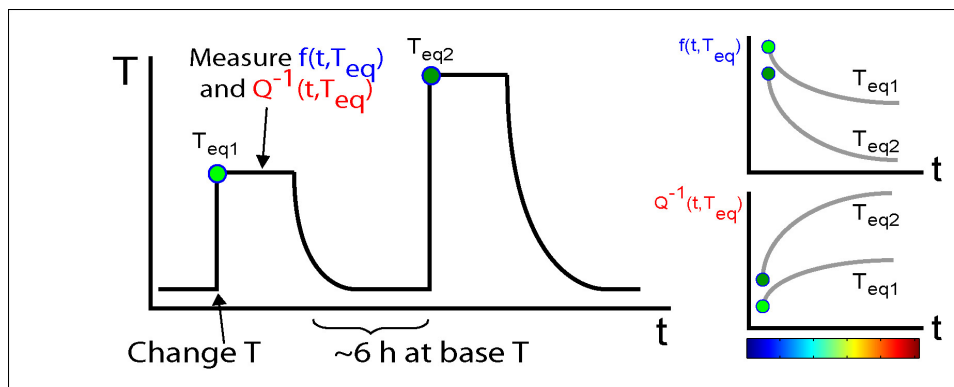


Figure 4.6: **Schematic of abrupt-warming experiment.**

The left portion of the figure shows the temperature-cycling protocol we use. The right portion of the figure shows the different relaxation curves of  $f$  and  $Q^{-1}$  taken at two different target temperatures  $T_{eq}^{(1)}$  and  $T_{eq}^{(2)}$ . The color bar shows increasing time from blue to red and is the same convention used in Figs. 4.7 and 4.9.

temperature of each system comes into equilibrium precisely at the same time  $t_{eq} \equiv 0$  and we then record the relaxation of the  $f(t, T_{eq}^{(i)})$  and  $Q^{-1}(t, T_{eq}^{(i)})$  for each system. Each curve in Fig. 4.7 would then represent a snapshot (in time) of the resonant frequency and dissipation of each member of the ensemble, each of which is at a different temperature  $T_{eq}^{(i)}$ .

It might be appropriate to describe the time evolution of the curves in Fig. 4.7 with a rotational susceptibility whose parameters change on the same time scale as in Fig. 4.3. For any particular model of  $\chi$  from Chapter 3, Fig. 4.7 gives us an idea of the parameters that would have to change with time to describe the data and thereby a preliminary picture of the time evolution of the relevant microscopic processes. For example, the frequency data in Fig. 4.7 appears to have the same total shift from low temperature to high temperature for all times, but  $T^*$  appears to be shifting to lower temperatures as time increases. Within the Debye model, this means that  $g_0$  would be constant in time but that  $\tau$  at a given temperature would be decreasing as time increased ( $\tau$  would be

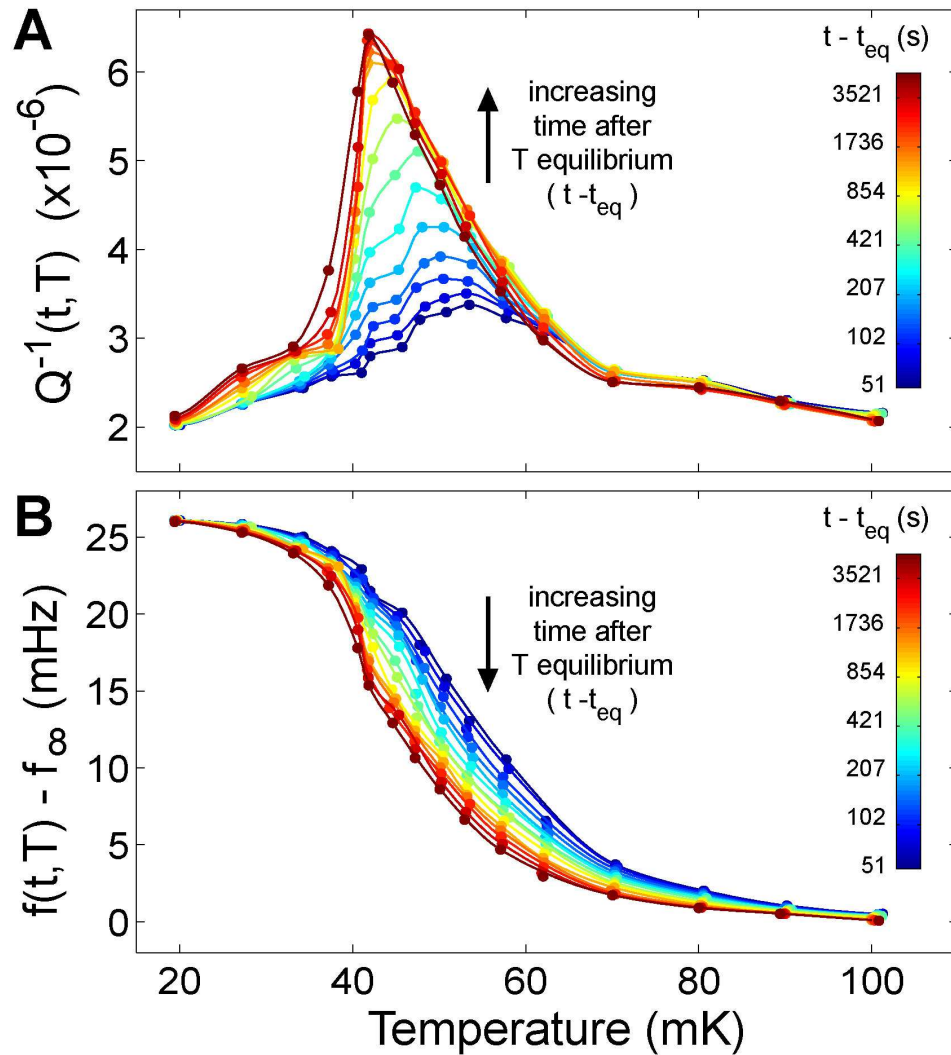


Figure 4.7: Non-equilibrium frequency and dissipation curves from the abrupt warming experiment.

changing such that the condition  $\omega_0 \tau(T^*) = 1$  would be satisfied at increasingly lower temperatures as time increased). This simple model of the (long-) time dependence of  $\chi$  fails in many ways (e.g. it cannot describe the dissipation data as a function of time) but it serves to introduce the types of issues we can begin to address with the time-dependent data. To that end, in the next section we introduce a powerful tool that allows us to simplify the description of the time-dependent data.

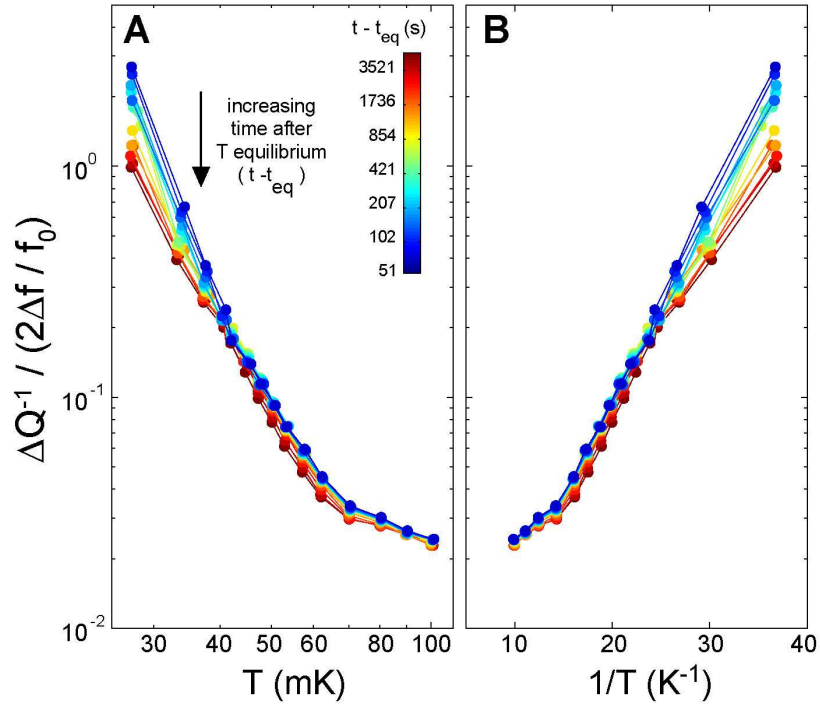


Figure 4.8:  $\Delta Q^{-1} / (2\Delta f / f_0)$  for time dependent data. (A) On log-log axes. (B) On Arrhenius axes (log vs.  $1/T$ ).

Fig. 4.8 shows the quantity  $\Delta Q^{-1} / (2\Delta f / f_0)$  for each curve in Fig. 4.7. For a Debye model or a viscoelastic model, this quantity is interpreted as  $\omega_0\tau(T)$ , and as for the well-equilibrated data of Fig. 3.3 the data seem to be equally well described by a power law and an Arrhenius law for  $T$  from zero up to around  $2T^*$  (and certainly in the dissipation peak region). As a function of time,  $\omega_0\tau(T)$  appears to be decreasing with time, which is consistent with the observation that the dissipation peak is shifting to lower temperatures as time increases after abrupt heating. Independent of the model used, at a given temperature the ratio  $\Delta Q^{-1} / (2\Delta f / f_0)$  is decreasing as a function of time. This change in the ratio is most pronounced for  $T \lesssim 40$  mK ( $1/T \gtrsim 25$  K $^{-1}$ ), where the data appear to fan out, but this is true at nearly all temperatures.

### 4.3.3 Davidson-Cole Plot

The identical relaxational characteristics of the TO frequency shift and dissipation reinforce the idea that the two observables are two facets of a single underlying physical mechanism, for which a single complex function, the rotational susceptibility  $\chi(\omega, T)$ , might be the most appropriate description. In such a scenario, we could expect the temperature to appear as a parameterization of the relationship between the real and imaginary components of  $\chi$ . A tool commonly used to illuminate this type of relationship is a direct plot of the imaginary vs. real components of a susceptibility in the complex plane. When used in the context of the dielectric susceptibility  $\epsilon$  of classical glasses or polarized liquids, this is called a Cole-Cole or Davidson-Cole (D-C) plot [38, 40]: the plot is the locus of points  $(\Re[\epsilon], \Im[\epsilon])$  and the implicit parameter is typically the measurement frequency  $\omega$ . In our experiment, by contrast, we fix the measurement frequency at the resonant frequency of the system  $\omega_0$  and we vary the resonant response of the system at  $\tau^{-1}$  by varying the temperature. The analogous plot to  $(\Re[\epsilon], \Im[\epsilon])$  would be the locus of points  $(\Re[\chi^{-1}], \Im[\chi^{-1}])$ . The D-C plot is important conceptually because it displays information about the linear response of the system without favoring one implicit variable over another.

It should be emphasized that in our experiments we do not *directly* measure the rotational susceptibility  $\chi^{-1}$  and therefore we cannot produce a true D-C plot of the data. Our observables  $\Delta f$  and  $Q^{-1}$  are related to the rotational susceptibility via Eq. 3.6, where  $\tilde{\omega} (\approx \omega_0 + ix + y)$  in that equation is the complex pole of  $\chi$  (i.e. the solution to  $\chi^{-1}(\tilde{\omega}, T) = 0$ ). Each model of the back-action  $g(\omega, T)$  and therefore of  $\chi^{-1}(\omega, T)$  will have a separate expression for  $\Delta f$  and  $Q^{-1}$  in terms of the parameters of that particular model, and so a D-C plot of our data

is necessarily model-dependent. However, for several models of  $g$  we find that

$$\begin{aligned}\frac{2\Delta f}{f_0} &\approx \frac{1}{I\omega_0^2} \Re [g(\omega_0, T)] \\ \Delta Q^{-1} &\approx \frac{1}{I\omega_0^2} \Im [g(\omega_0, T)],\end{aligned}\tag{4.1}$$

where  $\approx$  becomes an equality for the Debye susceptibility (to linear order in  $x$  and  $y$ ). In Eq. 4.1,  $\Delta f = f_0 - f(T)$  and  $\Delta Q^{-1} = Q^{-1}(T) - Q_\infty^{-1}$ . Thus, instead of plotting the susceptibility directly, we plot  $\Delta Q^{-1}$  vs  $2\Delta f/f_0$  and then if there are deviations from the Debye susceptibility, they should appear as prominent geometric features in the D-C plot. The Debye susceptibility represented by

$$g_{Debye}(\omega_0, T) = \frac{g_0}{1 - i\omega_0\tau(T)}\tag{4.2}$$

would appear as semicircle centered on  $X = g_0/2$  and with radius  $g_0/2$  (the  $X$ -axis is defined by  $X \equiv \Re[g_{Debye}]$ ), as can be seen from taking the real and imaginary parts of Eq. 4.2 and eliminating  $\omega_0\tau$  from the resulting equations. One finds that

$$(X - g_0/2)^2 + Y^2 = (g_0/2)^2$$

( $Y \equiv \Im[g_{Debye}]$ ). Thus, in Fig. 4.9(A) and (B) we plot  $\Delta Q^{-1}$  vs  $2\Delta f/f_0$  for the time-dependent data of Fig. 4.7. For comparison, in (A) we also include the D-C plot of a simple time-dependent model of the Debye susceptibility for values of  $g_0 = g_0(t)$  as determined by a fit to the (increasing) dissipation peak of Fig. 4.7(A). Presenting the data along the properly scaled axes as in 4.9(A) is a striking way of visualizing the result of Fig. 3.2, namely the result that although the Debye susceptibility can adequately describe the size and shape of the dissipation peak it underestimates the size of the frequency shift by a significant factor.

It is clear in Fig. 4.7 that the location of the dissipation peak  $T_{peak}$  is shifting to lower temperatures, and that the same is true for  $T_{max\ slope}$ , the the tem-

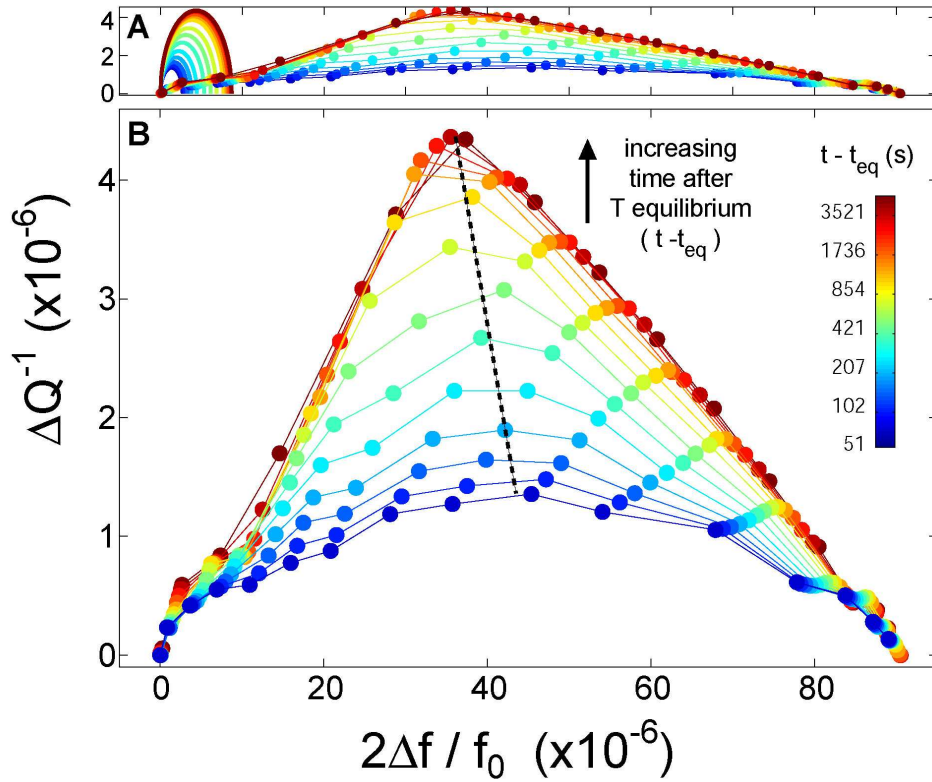


**Figure 4.9: Time-dependent Davidson-Cole (D-C) plot.**

(A) D-C plot on axes scaled such that the Y-axis is exaggerated by a factor of about 3:1. The semicircular Debye D-C plots are shown for comparison at the left. (B) D-C plot on axes where the Y-axis is exaggerated 20:1. The dashed line shows the skewing of the D-C plot with increasing time.

perature of maximum slope in the frequency  $df/dT$ . The time-dependence of the D-C plot in Fig. 4.9(B) allows us to see immediately a feature not readily apparent from Fig. 4.7: the temperature  $T_{peak}$  is shifting relative to  $T_{max\ slope}$ . This is another feature not captured by the Debye susceptibility, where  $T_{peak} = T_{max\ slope} = T^*$ , the temperature for which  $\omega_0\tau(T^*) = 1$ . In Fig. 4.9 this is manifest as a skewing of the shape of the D-C plot, indicated by a dashed line in the figure. From Chapter 3, one model that goes beyond the Debye susceptibility in explaining the frequency shift and dissipation was the glassy model of the

back-action

$$g_{gl}(\omega, T) = \frac{g_0}{[1 - i\omega\tau(T)]^\beta}$$

where  $\beta$  was an additional parameter (the stretching exponent) that captured the effect of having a distribution of modes. A skewed semicircular D-C plot is characteristic of the glassy susceptibility and is a consequence of the stretching exponent  $\beta < 1$ . It is apparent from Fig. 3.4 that in the glassy model  $T_{peak}$  can be quite different than  $T_{max\ slope}$  and that the difference increases as  $\beta$  gets farther from unity.

Fig. 4.10(A) shows the time-independent version of the D-C plot of the glassy susceptibility and Fig. 4.10(B) and (C) illustrate two different possibilities for the ways in which the glassy susceptibility might give a time-dependent D-C plot. Quite simply, there are two parameters,  $g_0$  and  $\beta$ , that can affect the total magnitudes of the real and imaginary parts of the susceptibility and therefore the range, domain and shape of the D-C plot. In 4.10(B) we allow only  $\beta$  to vary with time while keeping  $g_0$  constant. It is clear that such a model cannot describe our Fig. 4.9 data accurately; in this model, the height of the D-C plot decreases as time increases whereas in Fig. 4.9 the height clearly increases with time. The model in Fig. 4.10(C) allows  $g_0$  to increase and  $\beta$  to decrease with time and captures some of the essential features of the time-dependent susceptibility that we measure: the height of the D-C plot increases with time and the skew increases as well. (For clarity, the curves in Fig. 4.10(C) are offset so that they are centered at the same point on the X-axis). However, a central question of this work remains: what can account for the disproportionately large extent of the D-C plot along the frequency (X-) direction and why does it not appear to change with time? A naive argument is that most of the frequency shift is due to a superfluid component of the solid helium coexisting with (and whose phase

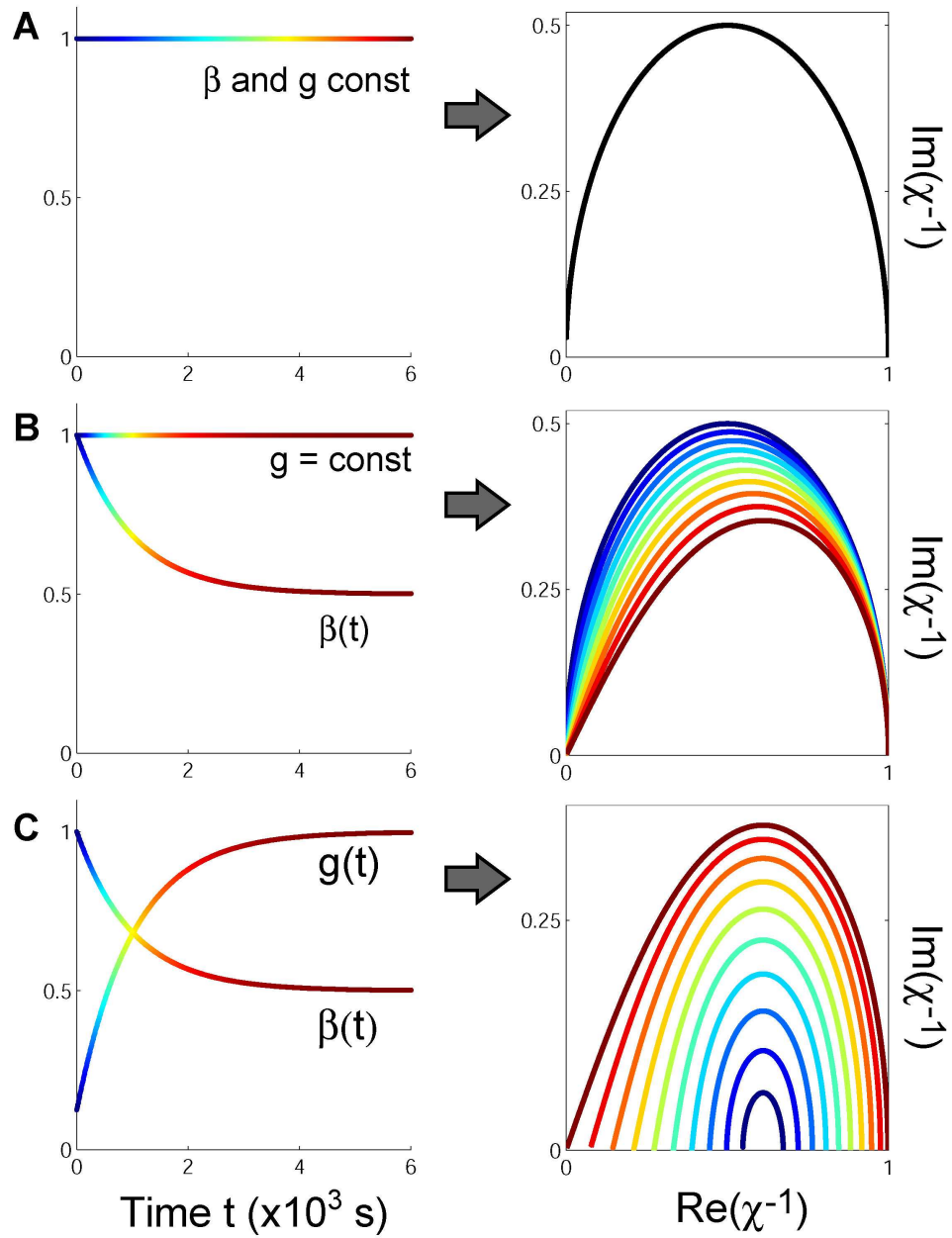


Figure 4.10: Three models of time dependence of parameters in a glassy susceptibility.

stiffness is apparently controlled by) the glassy component.

#### 4.4 Discussion of the Origin of the Long-Term Relaxation

In this section, I discuss the issue of whether the long time-constants we observe are related to the true mechanical disequilibrium of the  $^4\text{He}$  inside the TO, perhaps because of its glassy nature, or whether the long time-constants are simply a conspiracy of the thermal time-constants present in the TO- $^4\text{He}$  system. The section can be skipped with no consequence for the understanding of the physics of solid  $^4\text{He}$ .

We studied the thermal time-constants of the empty torsional oscillator by gluing a 100- $\Omega$  Matsushita carbon resistance thermometer onto a test cell with the identical geometry and materials used in the actual TO and securing the test cell to the mixing chamber. We attempted to measure the temperature of the actual torsional oscillator by inserting a germanium thermometer into a tightly fitting receptacle glued to its base and securing it in place with Apiezon N-grease. Unfortunately, the thermometer never correctly read the temperature of the Stycast oscillator, possibly because of a large thermal boundary resistance across the the thermometer-N-grease-TO interface. The thermal measurements in this section were therefore all taken on the test cell, but a picture of the thermometer assembly on the actual oscillator is shown in Fig. 4.11(A) for reference. A repeat of the cooling protocol for Experiment 1 (Fig. 4.2) indicated that there are always long time-constants associated with the relaxation of the temperature of the empty Stycast cell; these are shown in Fig. 4.11(B) alongside the full-cell mechanical relaxation data from Fig. 4.4. There are several differences. First, the

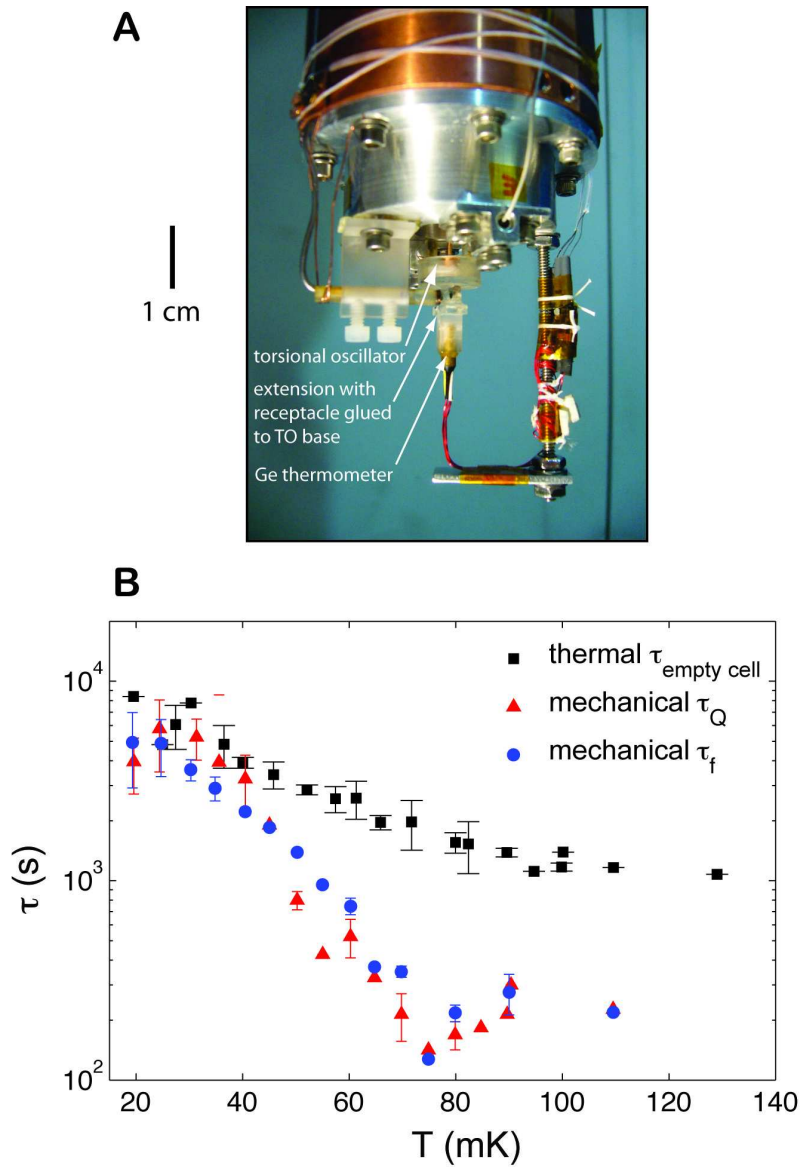


Figure 4.11: **Thermal relaxation study of torsional oscillator.** (A) Thermometer glued to TO. (B) The time constant for thermal relaxation of the empty cell (black squares) compared to the mechanical time-constants for the relaxation of the dissipation (red triangles) and frequency (blue circles) of the full cell containing solid helium.

change in the thermal and mechanical time-constants appear to have different temperature dependences. Second, for  $T > 75$  mK the thermal time-constants are an order of magnitude larger than the mechanical time-constants. Thirdly, and perhaps most importantly, there appears to be no feature in the empty-cell thermal time-constant at 75 mK, where the onset of the rise in the full-cell mechanical time-constants begins. If the temperature of the Stycast bob and the helium contained within it relax at different rates<sup>2</sup>, as seems to be the case from Fig. 4.11(B), then we would expect an overall slow relaxation of the frequency and of the dissipation of the Stycast-helium system. How do we determine the contribution of each component to the overall relaxation? Fig. 4.5 shows  $R_f$ , the percentage of a given frequency change for a given 5 mK temperature step that occurs after the temperature of the mixing chamber has come into equilibrium; this number ranges from around 10% to about 55% at the lowest temperatures measured. It is clear from Fig. 4.12, however, that the contribution to the frequency change of the system between 100 mK and 15 mK due to the Stycast is tiny compared to that due to the solid  $^4\text{He}$ . As a specific example, consider the temperature around 50 mK, where  $R_f = 30\%$ . At this temperature, the slope of the full cell  $df/dT$  is about 60 times larger than the that of the empty cell  $df/dT$ , so that if the slow relaxation at 50 mK was primarily due to that of the empty cell we would expect  $R_f$  to be closer to  $1/60$  (1.7%) than to 30%, and the relaxation after the temperature equilibration of the mixing chamber would appear flat on the scale of Fig. 4.3 for all temperatures. The conclusion is that whatever is ultimately responsible for the slow dynamics of the Stycast- $^4\text{He}$  system as a whole (thermal relaxation, mechanical relaxation or otherwise), the data of Fig.

---

<sup>2</sup>As mentioned in Section 4.2.1, we expect that the solid  $^4\text{He}$  and the mixing chamber are in very good thermal contact, owing to the presence of a silver-sintered heat exchanger between the two and the high thermal conductivity of solid  $^4\text{He}$ . The energy dissipated in the solid  $^4\text{He}$  is rapidly removed to the mixing chamber thermal bath.

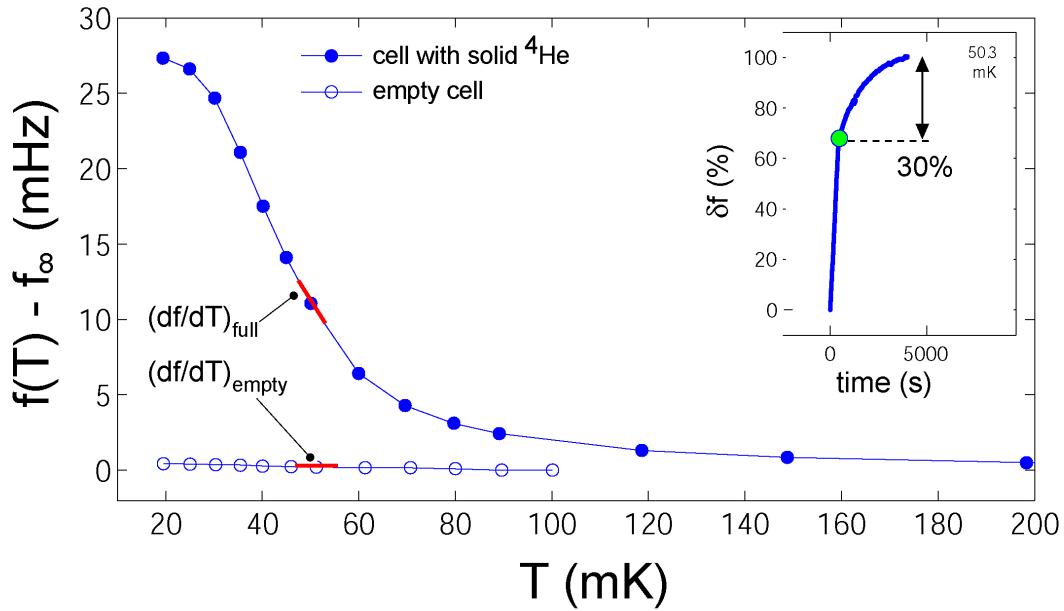


Figure 4.12: **Comparison of resonant frequency  $f$  of the empty TO and  $f$  of the TO filled with solid helium.**

The slope  $(df/dT)_{full}$  of the filled cell is about 60 times that of the empty cell  $(df/dT)_{empty}$  at 50 mK. For a given small temperature change, the contribution to the changes in  $f$  due to the solid  $^4\text{He}$  is 60 times the contribution from the weak temperature dependence of the empty cell. **(Inset)** The percentage change  $\delta f(t)$  of the filled TO after a  $\delta T = 5$  mK step down to 50.3 mK (reproduced from Fig. 4.3). After the mixing chamber temperature comes into equilibrium (at the [green] filled circle), the frequency relaxation continues for an additional 30% of its total change at this temperature, for several thousand seconds. From Fig. 4.11, the Stycast chassis appears to thermalize with the mixing chamber much more slowly than the solid  $^4\text{He}$  contained within it. If the behavior in the inset figure were separable into the fast relaxation of  $f$  and  $Q^{-1}$  due to the solid  $^4\text{He}$  and the subsequent slow relaxation due to the poor thermalization of the Stycast, one would expect the percentage change at the slow rate to be of the order of  $1/60$  ( $\approx 1.7\%$ ) instead of 30%.

4.3 suggest that the effect is predominantly because of the relaxation of the solid helium and not solely to that of the Stycast.

Since this argument shows that the relaxation of the TO must be primarily because of the  $^4\text{He}$ , there are two possible conclusions about the nature of the relaxation. The first is that the helium has a complicated temperature relaxation

function  $T_{4\text{He}}(t)$ , whose precise form depends on the various quantities in the system (Kapitza and thermal boundary resistances, thermal conductivities, heat capacities), and that the dissipation and frequency relaxation data of Fig. 4.3 and of Fig. 4.7 are simply independent measurements of this temperature relaxation function, according to the functionals  $Q^{-1}[T_{4\text{He}}(t)]$  and  $f[T_{4\text{He}}(t)]$ , whose infinite-time curves would be the results shown in Fig. 1.6. To test this idea, one would need to measure directly the temperature of the helium within the  $100\ \mu\text{m}$ -wide annular cavity, which is at present impossible. However, there is a simple argument that shows that the complex relaxation dynamics of the solid  $^4\text{He}$  we have shown in this chapter cannot be explained by the  $^4\text{He}$  sample being out of thermal equilibrium with the mixing chamber thermometer. For this argument, the time-dependent Davidson-Cole plot (Fig. 4.9) is an essential tool.

The Davidson-Cole plot for the infinite-time curves  $Q^{-1}[T_{4\text{He}}(t \rightarrow \infty)]$  and  $f[T_{4\text{He}}(t \rightarrow \infty)]$ , is shown in Fig. 4.13(A); this is a D-C plot of the data in Fig. 3.2. One usually thinks of this curve as being parameterized by the temperature of the helium, but if its temperature is changing as a function of time (and is  $T_{4\text{He}}(t)$  changing slowly compared to  $Q/\omega_0$ ) one can regard as an equivalent parameter the time  $t$ . This means that the time-dependent Davidson-Cole plot would be indistinguishable from the static (infinite-time) plot – as a function of time the system would simply be moving along the single curve [depicted with a sequence of arrows in Fig. 4.13(A)]. The data from Fig. 4.9, reproduced in Fig. 4.13(B), demonstrate that this is not the case and lead one to the second conclusion: far richer relaxation dynamics exist in solid  $^4\text{He}$  than would be produced by a mere delay in thermalization of the sample.

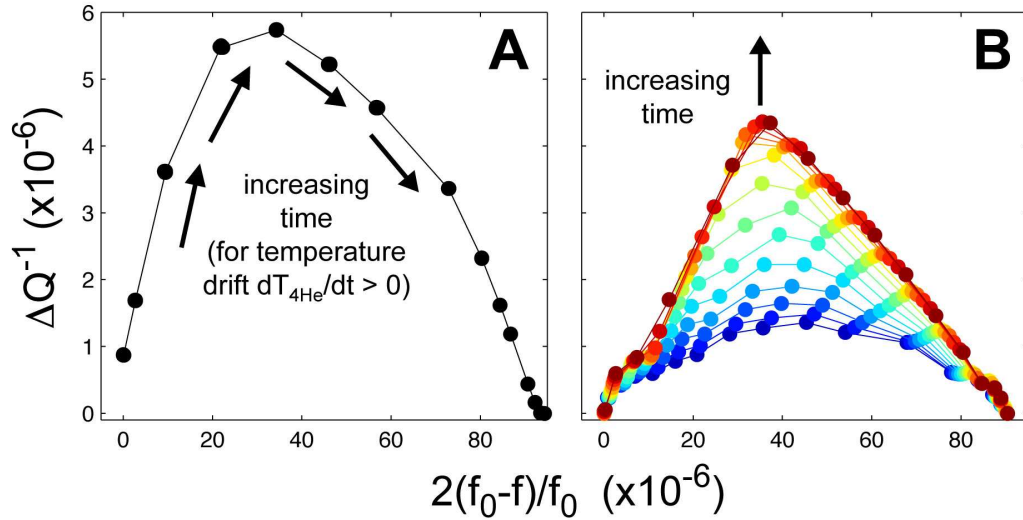


Figure 4.13: **Comparison of time-dependent D-C plots for thermalization dynamics and the observed dynamics.**

(A) The time evolution of the Davidson-Cole plot for the dynamics described only by a changing  $T_{4He}(t)$ . The plot is shown for the case where the temperature increases with time (as would be expected if  $T_{4He}(t)$ , lagged the mixing chamber temperature  $T_{mixc}$  after an increase in  $T_{mixc}$ , as per the heating protocol of Experiment 2). (B) The observed time evolution of the Davidson-Cole plot. These are the same data as Fig. 4.9; they reveal a more complicated relationship between the dynamics of the frequency and of the dissipation as the TO- $^4\text{He}$  system evolves from its low-temperature state (cf. Fig. 4.10).

## 4.5 Summary and Discussion

In this chapter we presented the results of experiments on the relaxation dynamics of solid  $^4\text{He}$  contained in a torsional oscillator. The central observations of those experiments were the following:

1. When cooling the TO-solid  $^4\text{He}$  from high temperature in 5 mK steps, the relaxation times for the TO resonant frequency ( $\tau_f$ ) and dissipation ( $\tau_Q$ ) began to lengthen at a temperature between the onset of the TO frequency shift and the location of the dissipation peak (at  $T^*$ ). The relaxation times

$\tau_f$  and  $\tau_Q$  increase with decreasing temperature and have identical temperature dependences.

2. After a temperature step, there is a portion of the  $f$  and  $Q^{-1}$  relaxations that responds immediately to the mixing chamber temperature and a portion that relaxes on the slow time scales  $\tau_f$  and  $\tau_Q$ . We quantify the portion of the  $f$  ( $Q^{-1}$ ) that relaxes at the slow rate as the percentage  $R_f$  ( $R_Q$ ) of the total change for a given temperature step.  $R_f$  ( $R_Q$ ) varies from 10% to 55% (5% to 70%) depending on the temperature.
3. If we abruptly heat the helium from its lowest temperature to a final temperature  $T_{eq}^{(1)}$ , cool back down to base temperature, and repeat for a sequence of temperatures  $T = T_{eq}^{(1)} \dots T_{eq}^{(N)}$ , we can construct a picture of the time evolution of  $f(T)$  and  $Q^{-1}(T)$  as the helium solid emerges from its state at the lowest temperature.

In Chapter 3 we discussed models of the back-action of the helium solid on the TO and we concluded that a back-action term with a single response time (the Debye form) could not simultaneously fit the frequency and dissipation data. We suggested that the main fault of the Debye form could be corrected either by the addition of a superfluid term (with no accompanying dissipation) or by considering a susceptibility that had a response at a distribution of response times, characterized by a “stretching exponent”  $\beta$ , which broadened the dissipation peak and reduced its height. The latter susceptibility was termed “glassy” by analogy to the dielectric susceptibility of certain supercooled liquids. One of the hallmarks of structural glass formers such as supercooled liquids is this “nonexponentiality”: the response at not one but a distribution of relaxation times [27]. The basic idea of the Debye and glassy models is the same, though: a liquid-like ensemble of excitations having a (distribution of) relaxation rate(s)  $\tau_s^{-1}$  responds

resonantly when the frequency of the oscillator  $\omega_0$  matches this relaxation rate. As the temperature is lowered, the excitations freeze into a (glassy) solid: the relaxation time  $\tau_s$  becomes extremely long. It is possible that this freezing transition facilitates the establishment of global phase coherence of the putative supercomponent. This basic picture of the (super)glass is shown schematically in Fig. 4.14(A).

We observe long relaxation times  $\tau_\ell$  in the mechanical equilibration of the helium at low temperatures ( $\sim 10^3 - 10^4$  seconds), in addition to the much shorter time scale  $\tau_s$  of the response time to agitation on the time scale of  $\omega_0^{-1} \sim 1$  ms. Glasses often exhibit behavior on two distinct time scales (corresponding to the  $\alpha$  and  $\beta$  processes in the energy landscape picture of Stillinger [110]; this is not the same  $\beta$  as the stretching exponent of Eq. 3.19), but we do not observe the  $\alpha - \beta$  bifurcation typical of certain glass formers. However, a viscous slowdown of relaxation processes as the glass transition is approached from above is a ubiquitous feature of glasses, and our Fig. 4.4 may be a demonstration of such an effect.

There is ample experimental evidence from the TO studies (though somewhat less evidence from the structural measurements) and a sound theoretical groundwork for the existence of a glass, and even a superglass, in solid helium, summarized in the introduction to this chapter and in Secs. 1.4.6 and 1.5.1. We have contributed to this body of knowledge by providing evidence of relaxation of the helium which is long and lengthens as  $T \rightarrow 0$ . We do not show any direct evidence for the existence of superfluid behavior in the helium, but if the correct interpretation of the blocked annulus experiments is the existence of a superfluid, then this phase might indeed be characterized as a superglass.

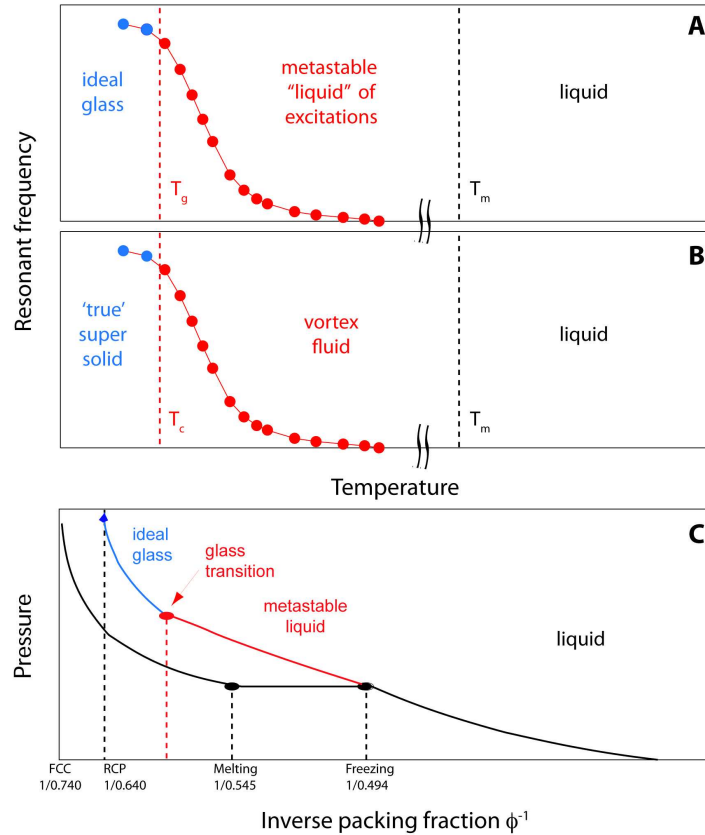


Figure 4.14: **Analogy between glass/vortex fluid transitions and Brownian hard-sphere transition.**

(A) Excitation freeze-out as introduced in [86]. (B) Vortex fluid state as introduced in [7]. The 'true' supersolid is possibly of the Andreev-Lifshitz-Chester type in this theory. The data in (A) and (B) are the same as those in Fig. 3.2 and are included to illustrate how the behavior of the TO resonant frequency reflects each stage of the proposed glassy and vortex fluid transitions. (C) Jamming of hard spheres (top curve), eventually resulting in glassy random close packing (RCP) and "freezing" transition (bottom curve) resulting in a face-centered cubic lattice (FCC). This is reproduced from Fig. 1.10(A) but shown on an inverted X-axis ( $\phi^{-1}$  instead of  $\phi$ ) for easy comparison with (A) and (B).

An important final issue to address is whether we have characterized a glass correctly. There are many types of glasses in nature described by many models, and so to observe behavior associated with the disorder present in the helium crystal may not guarantee that we are observing an analog of another glassy phase of matter. This is a perspective advocated by Anderson [5], who emphatically suggested that what we observe is not like any known glass but rather can be understood in terms of his model of a vortex fluid above its true supersolid transition temperature [Fig. 4.14(B)]. He attributes the long relaxation times as a slow decay of the number of the vortices present in the sample as the transition temperature is approached from above, which may be caused by large fluctuations in the superfluid density [9], which, significantly, he says is a consequence of disorder but not of glassiness. I am of a different mind; I believe that “glass” is an appropriate characterization of a system in which disorder plays a large role, the disorder depends on how the sample is prepared [in analogy to a supercooled liquid or jamming transition - see Fig. 4.14(C)], and in which behavior on several time scales is evident. That the correct microscopic model has not been identified does not exclude characterization of the helium solid as a glass, although it should be said that X-ray scattering measurements do not find evidence of any liquid-like or amorphous component. Whether the idea of the system as a glass or as a vortex fluid constitute mutually exclusive descriptions, or whether the vortex tangle could itself be described as a glass, I believe the correct direction is to look for evidence for particular types of excitations. For example, if we revisit the heat capacity measurements (which currently are much more precise) and find that the linear term persists in all of the measurements, or is more highly correlated with quench-cooled samples, then this would be evidence for the type of glass for which an ensemble of (two-level)

tunneling systems is a good model. On the other hand, if evidence for phase slips or measurements of quantized vorticity could be found it would virtually close the door on the idea of a glass, or at least specific models of glasses such as two-level systems.

## CHAPTER 5

### UNIFIED DYNAMICS OF SOLID $^4\text{He}$

We undertook this study in order to understand the puzzling role of velocity in the TO experiments. The velocity dependence of the TO frequency shift was introduced in the first paper of Kim and Chan [72], where it was reported that frequency shift began to be reduced from its low-velocity saturated value by increasing the rim velocity to a few tens of  $\mu\text{m/s}$ . This number was called the “critical velocity” of the superflow and was identified with the velocity field of a few quanta of vorticity in a typical (annular) geometry having a radius of a few millimetres, though the magnitude of this critical velocity is several orders of magnitude smaller than most critical velocities observed in other superflow experiments. Further confounding the issue, Kojima reported the existence of hysteresis in the frequency shift as the velocity was cycled from high to low to high again [14], a result our group and others have been able to reproduce [103].

The miniscule critical velocity and the existence of hysteresis in the frequency shift are quite unexpected in the context of a mean-field 3D superfluid transition and known mechanisms for vortex creation. Compared to their treatment of the disorder,  $^3\text{He}$ -impurity, temperature and frequency dependence, other models of solid helium have been somewhat reticent to address the velocity dependence. Some experimentalists have found qualitative explanations of their history-dependent data in the vortex fluid model of Anderson [14, 35], but perhaps it is the lack of published quantitative studies of the velocity dependence that is responsible for its absence in the theoretical discussion. Possibly, the velocity dependence is viewed as a trivial consequence of exceeding the critical velocity in superfluid models or entering a nonlinear regime in other models;

we hope to show in this chapter that this is not the case. Another outstanding issue is the uncanny resemblance of the velocity dependence of the TO frequency shift to the strain dependence of the shear stiffening ([43], Sec 1.4.3). The principle of parsimony would suggest that they are related phenomena, but an exact correspondence is not quite reconciled by the predicted stress fields within the <sup>4</sup>He solid samples [35]. This does bring up the important issue of whether velocity is really the correct quantity on which to be structuring our analysis, or if velocity should cede its place to a more physically appropriate variable, such as the shear or shear rate.

Making use of the high signal-to-noise of our SQUID-based displacement sensor, we developed a new technique for mapping of the TO frequency shift and dissipation in the velocity-temperature plane and we found a remarkable symmetry in the behavior of the two observables along the two axes. This result is suggestive of the idea that, in analogy to an ensemble of excitations of which the population is temperature-dependent, the agitation of the helium crystal (for which the velocity is a proxy) generates an equivalent ensemble of excitations; it is known that for certain driven systems near their glass (or jamming) transition that the shear rate  $\dot{\gamma}$  can be thought of as an effective temperature [87]. We show that the data along the velocity and temperature axes can be collapsed to a single axis  $X = X(v, T)$  and that using a generalized *nonlinear* rotational susceptibility  $\chi^{-1}(v, T)$ , the entire set of  $f(v, T)$  and  $Q^{-1}(v, T)$  data can be satisfactorily fit using a single function.

## 5.1 Methods

To efficiently map the frequency and dissipation as a function of temperature and velocity, we studied the free inertial decay (FID), or ringdown, of the TO at a series of different temperatures. The term “ringdown” for a simple harmonic oscillator (SHO) with a constant  $Q$  is just the response when the drive is suddenly switched off and the oscillatory motion  $x_{SHO}(t)$  of the SHO decays with an exponential envelope

$$x_{SHO}(t) = x(0)e^{-t/\tau_{ampl}} \cos(\omega_0 t + \phi),$$

where the time constant for *amplitude* decay  $\tau_{ampl} = 2Q/\omega_0 = Q/\pi f_0$ . The factor of 2 is present because  $Q$  is defined as  $2\pi \times (\text{energy stored in oscillator} / \text{energy lost in one cycle}) \approx \omega_0 \tau_{energy}$ , and since the energy  $E \sim x^2$ ,  $\tau_{ampl} = 2\tau_{energy}$ . For a SHO one could determine the  $Q$  by measuring the slope of the envelope  $e^{-t/\tau_{ampl}}$  on a log scale.

For the TO filled with solid  $^4\text{He}$  the procedure for determining  $Q$  is analogous but not quite as straightforward, because the dissipation  $Q^{-1}$  is a function of velocity, meaning that the ringdown amplitude is not a simple exponential decay as a function of time. Fig. 5.1 shows a typical ringdown envelope of the oscillator amplitude as a function of time. We determine the  $Q(t)$  (and therefore the  $Q[v(t)]$ ) by measuring the instantaneous slope of the envelope at each time  $t$  (for a finite dataset, we of course need to take a window of data points centered at  $t$  and perform an exponential fit to the data in this window - a boxcar fitting procedure). Repeating this for a sequence of temperatures allows us to measure  $Q^{-1}(v, T)$ . We simultaneously record the resonant frequency as a function of time during the ringdown and thereby construct the complementary surface  $f(v, T)$ .

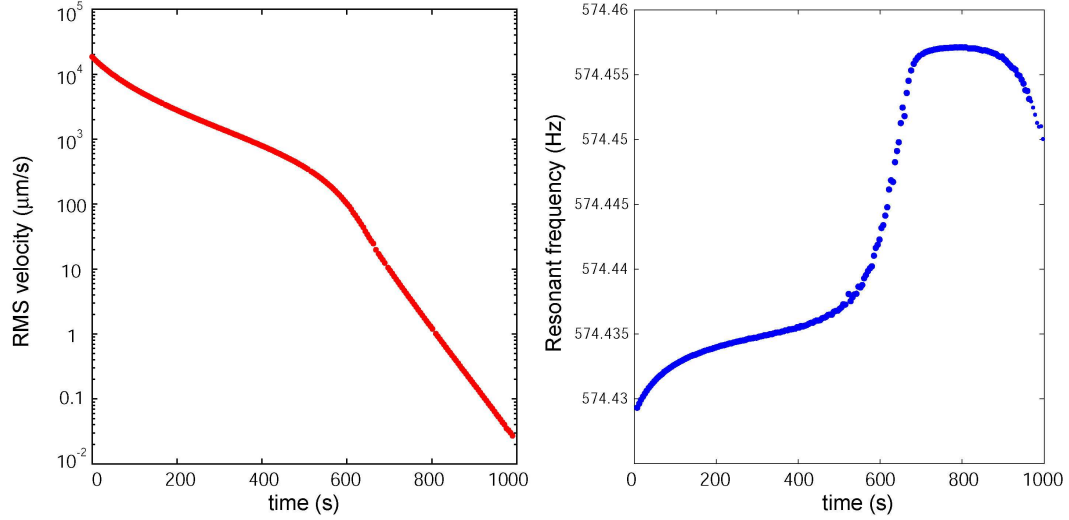


Figure 5.1: **Typical ringdown of the solid  $^4\text{He}$ -filled TO at 47 mK.**

The left panel shows the velocity as a function of time. Where the velocity is changing the slowest with time, around 500 s, the  $Q$  is lowest and the dissipation  $Q^{-1}$  the highest. To obtain  $Q[v(t)]$ , we perform a boxcar exponential fit to the data with a sliding window about 28 seconds wide. The right panel shows the resonant frequency as a function of time. The change between 0-100 seconds is a feature of the empty oscillator (it is present in the empty cell ringdowns as well). The sudden turndown at about 900 seconds is because of the limitations of the self-resonant locked loop. The large increase starting at 500 seconds and ending at about 700 seconds is the appearance of the supersolid signal as the velocity drops below about  $30 \mu\text{m/s}$ .

Before each ringdown at a new temperature  $T_{eq}$ , the TO is driven to a high velocity (typically around 3 mm/s) and allowed to relax (thermalize) for about 330 seconds<sup>1</sup>. The ringdown begins at  $t = 0$  by turning the drive amplitude to zero (but maintaining the measurement circuit in the self-locked detection scheme of Fig. 2.5). The resonant frequency is recorded with the high-precision frequency counter using a 4.0 second integration gate time and the displacement amplitude (proportional to either the SQUID or capacitor output) is averaged with a lock-in amplifier for approximately the same amount of time. The boxcar fitting procedure to obtain  $Q^{-1}(v)$  uses a window seven gate-times (28

<sup>1</sup>This, plus the  $> 2500$  sec for ringdown and ringup, is adequate to stabilize the frequency for all but the very lowest temperatures

seconds) wide. Because we measure the ringdown over 5-6 decades of velocity, we need to employ both the SQUID detector and the capacitive detector to capture the entire range of behavior. The capacitive sensor is approximately useful in the range  $20 \mu\text{m/s} \rightarrow >3 \text{ mm/s}$  and the SQUID sensor in the range  $<10 \text{ nm/s} \rightarrow 40 \mu\text{m/s}$ , so there is a very small overlap region where both sensors can be used, but the region is fortunately large enough to construct ringdowns that are sufficiently continuous to use the boxcar fitting procedure to obtain  $Q^{-1}(v)$ . Unfortunately, the velocity range  $10 \mu\text{m/s} \rightarrow 100 \mu\text{m/s}$  is where most of the interesting behavior occurs, and so in the future the plan is to operate the ringdown experiment with an order of magnitude reduced sensitivity in the SQUID to allow the upper limit of the SQUID to be above the region of largest change in  $Q^{-1}(v)$  and  $f(v)$ . At about  $30 \mu\text{m/s}$ , close to the upper limit of the SQUID, the displacement detection circuit is switched electronically from capacitor to SQUID within one gate time and the ringdown progresses until the self-resonant detection loop can no longer lock to the SQUID signal. This is actually above the minimum sensitivity of the SQUID, which is less than  $0.01 \text{ nm/s}$  when integrating for 4 seconds, but we have verified that no additional information is gained by measuring the velocity dependence between the unlocking of the self-resonant loop and this minimum sensitivity. The entire ringdown takes approximately 20 minutes. The temperature is subsequently incremented, the TO is rung up to  $3 \text{ mm/s}$ , and the FID procedure is repeated.

## 5.2 Results

Figures 5.2(A) and (B) show the frequency shift and dissipation, respectively, as functions of the ringdown velocity for a number of different temperatures.

The empty cell data have been subtracted, and the curves have been cut off at  $1 \mu\text{m/s}$  to avoid obscuring their features with the difficulties at extremely low velocity (see Fig. 5.1). The resemblance of these curves to the  $f(T)$  and  $Q^{-1}(T)$  curves for a sequence of increasing velocities is quite striking (see, e.g., Fig. 1.5) and is made even more so by presenting the data of Figs. 5.2(A) and (B) in a temperature-velocity **contour plot** of the frequency shift and dissipation. To obtain enough data to smoothly interpolate between temperatures, we took ringdowns at 98 temperatures between 20 mK and 300 mK, which we could do in approximately four days (at about 30 minutes per ringdown). These contour plots are shown in Fig. 5.3 on logarithmic scales in both velocity and temperature. Viewing the data in this way allows us to notice a number of features immediately:

1. The temperature dependence of the putative 'critical velocity' can be read directly from the frequency contours. One can choose to define the critical velocity in a particular way, such as the velocity at which the frequency shift is diminished from its low velocity value  $\Delta f^{max}$  by a certain fraction  $x$ , and then  $v_c(T)$  is the contour that corresponds to the constant value of frequency shift  $(1 - x)\Delta f^{max}$ . For example, if  $v_c$  was defined so that  $x = 0.5$ , then  $v_c(T)$  would be the contour passing through the green region of Fig. 5.3(A). (A more realistic  $x$  might be defined as the minimum value for which a change from  $\Delta f^{max}$  due to the increased velocity is detectable above the noise).
2. There is a peak in  $Q^{-1}(v)$  for all temperatures  $T \lesssim T^*$ . This is apparent from Fig. 5.2(B), and is the first time that this has been explicitly reported. The symmetry of the behavior of  $Q^{-1}(v)$  at constant  $T$  and  $Q^{-1}(T)$  at constant  $v$  is immediately apparent from the contour plot.

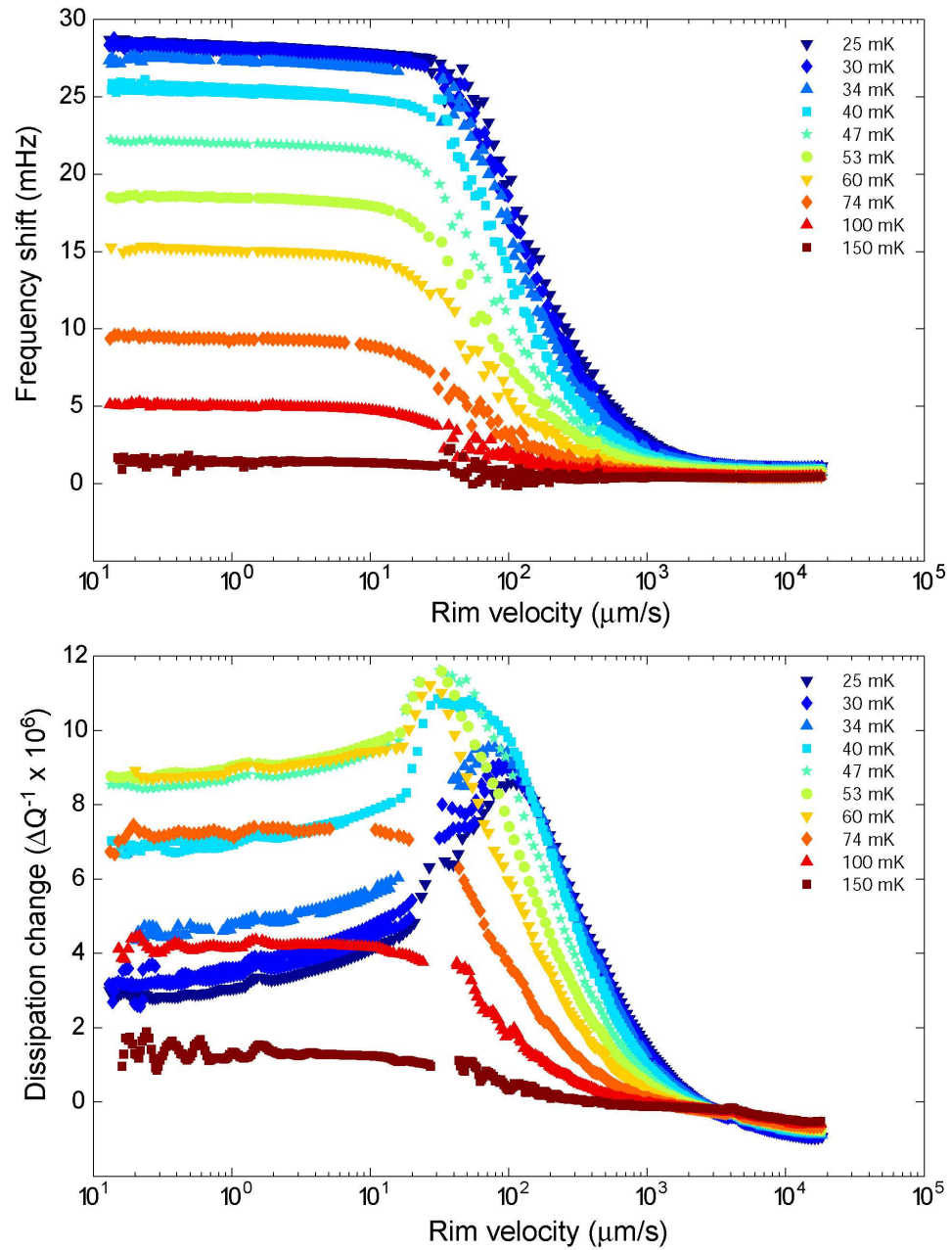


Figure 5.2: Resonant frequency shift and dissipation as a function of ring-down velocity.

The break in the data around  $30 \mu\text{m/s}$  is an artifact of switching between the (high-velocity) capacitive sensor and the (low-velocity) SQUID sensor.

3. There is a 'superpeak' where the dissipation is maximum at a single point in the phase diagram at  $Q^{-1}(v^*, T^*)$ , where  $v^* = 30 \mu\text{m/s}$  and  $T^* = 50 \text{ mK}$ . This feature is also an original discovery of ours, but the implication of such a superpeak for the unified behavior in  $v$  and  $T$  is not entirely understood.
4. The symmetry of the temperature and velocity dependence of  $f$  and  $Q^{-1}$  immediately leads us to ask about the scaling behavior of  $v$  and  $T$ . In other words, if we were to take a linecut (of  $f$  or  $Q^{-1}$ ) at constant  $v$  and one at constant  $T$ , how would  $v$  have to be scaled in order that the two curves laid on top of one another? In the vocabulary of [87], if there were an effective temperature associated with the variable  $v$ , how would  $T_{eff}$  depend on  $v$ ? For example, would it behave as a power law  $T_{eff} \sim v^{\zeta/\alpha}$  for some power  $\zeta/\alpha$ ?

I will discuss point #4 in the greatest detail because it has the most far-reaching consequences for the discovery of new physics. Points #2 and #3 will be addressed in conjunction with point #4 and in the context of extending the ideas of Chapter 3 to include a velocity-dependent analog of the rotational susceptibility. Point #1 will be addressed briefly at the end to contrast the behavior of this system with that of the critical velocity in superfluid systems.

### 5.2.1 Scaling of Velocity and Temperature

To search for a quantitative relationship between  $f(T)$ ,  $f(v)$ ,  $Q^{-1}(T)$  and  $Q^{-1}(v)$ , we compared the dynamics of these quantities as a function of  $T$  at constant velocity to those as a function of  $v$  at constant temperature. This is equivalent to

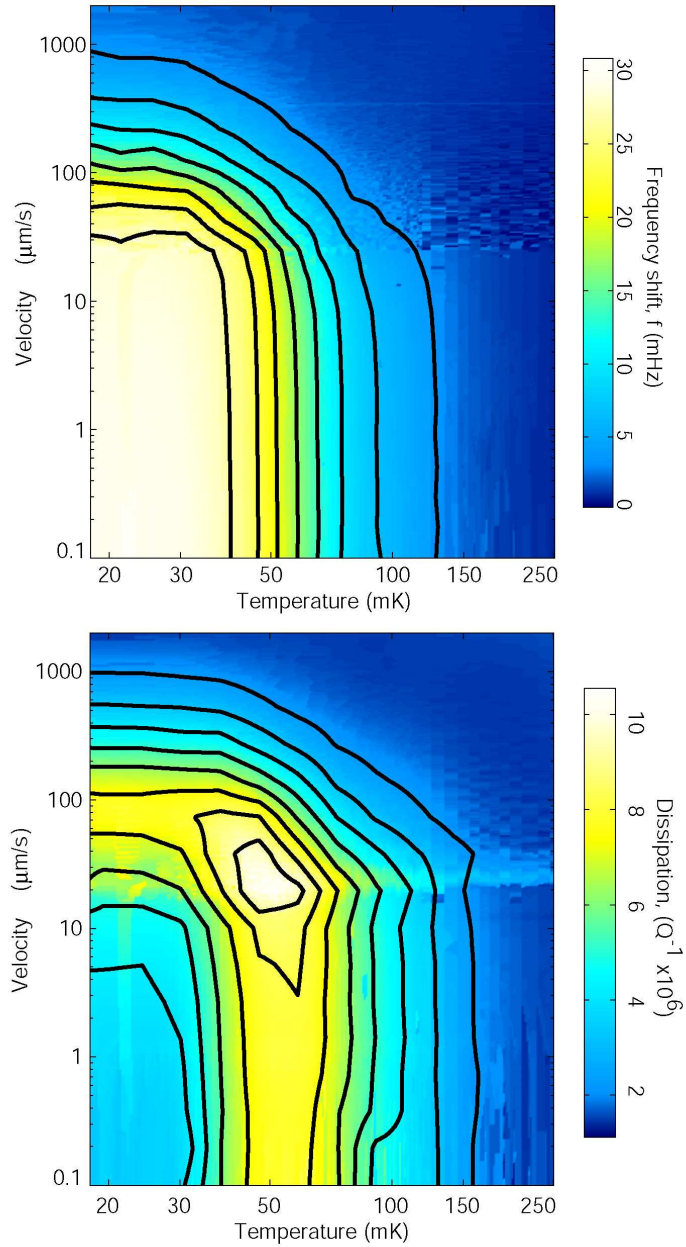


**Figure 5.3: Temperature-velocity phase diagrams.**  
 The feature in the data around 30  $\mu\text{m/s}$  is an artifact of switching between the (high-velocity) capacitive sensor and the (low-velocity) SQUID sensor.

taking linecuts in the contour plots of Fig. 5.3, horizontally for constant temperature and vertically for constant velocity. Four such linecuts are shown in Fig. 5.4,  $\Delta f(T)$  and  $Q^{-1}(T)$  at a constant velocity of  $5 \mu\text{m/s}$  (horizontal dashed lines) and  $\Delta f(v)$  and  $Q^{-1}(v)$  at a constant temperature of  $19.5 \text{ mK}$  (vertical solid lines). Indeed it is easy to define the empirical  $T^*$  and  $v^*$  and by examination of these curves, as shown by arrows in Fig. 5.4(B) and (D). Moreover, as a first step toward quantitative understanding of this unified behavior, we can determine an approximate scaling relationship between  $T$  and  $v$  from a comparison of the data of Fig. 5.4(A) and the data of Fig. 5.4(B):  $T$  should scale *roughly* as  $\sqrt{v}$ . The same conclusion holds if instead we compare the dissipation data of Fig. 5.4(C) and of Fig. 5.4(D).

In Chapter 3 and Chapter 4 it was suggested that the behavior of the solid  $^4\text{He}$  in the TO could be modelled as a back-action term in the rotational susceptibility  $\chi$ , an idea I review here in the context of the current discussion. The entire temperature dependence of the system would be subsumed in the back-action term of  $\chi$ , and for the Debye model of the back-action term there would be a resonant response of the system when the probe frequency  $\omega_0$  matched the relaxation rate  $\tau^{-1}(T)$  of the putative ensemble of excitations in the helium solid (the identical conclusions come from modelling the helium as a viscoelastic (VE) solid [125]). I reproduce the equation for the Debye model of the rotational susceptibility here for clarity (the back-action is the term proportional to  $g_0$ ):

$$\chi^{-1}(\omega, T) = -I\omega^2 - i\gamma_{TO}\omega + K - \frac{g_0}{1 - i\omega\tau(T)}. \quad (5.1)$$

The symbols have the same meaning as Eq. 3.9. The resonant frequency shift and dissipation were obtained by solving for the real and imaginary parts of  $\chi^{-1}(\tilde{\omega}, T) = 0$ , so the frequency shift and dissipation are related to the real and imaginary parts of  $\chi^{-1}$ . In the Debye and VE models, they are related exactly

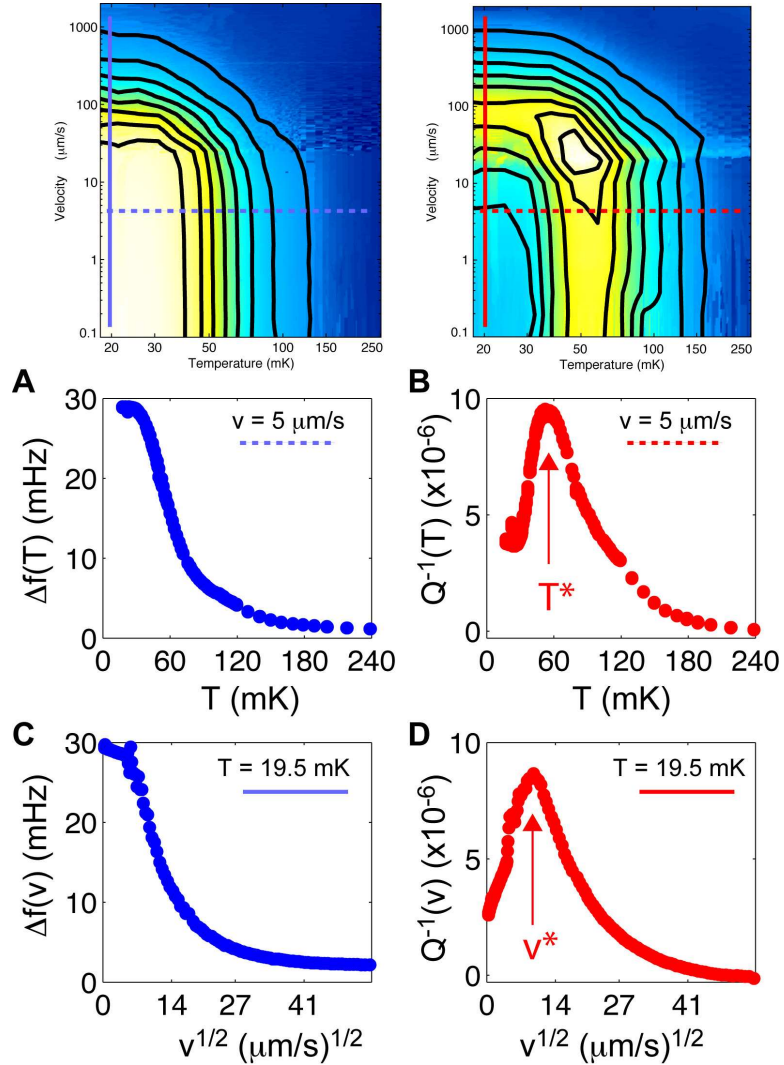


**Figure 5.4: Linecuts of frequency shift and dissipation contours.** Panels A and B show linecuts at a constant velocity of  $5 \mu\text{m/s}$  of the TO frequency shift and dissipation, respectively (dashed horizontal lines on the contour plots). Panels C and D show linecuts at a constant temperature of  $19.5 \text{ mK}$  (solid vertical lines on the contour plots).

by

$$\frac{2\Delta f(T)}{f_0} = A \frac{1}{1 + (\omega_0 \tau)^2} \quad (5.2)$$

and

$$\Delta Q^{-1}(T) = A' \frac{\omega_0 \tau}{1 + (\omega_0 \tau)^2} \quad (5.3)$$

where  $A = A' = g_0$  for the Debye susceptibility and

$$A = A' = \rho R^2 I_{He} F(h/R) \omega_0^4 / 24 \mu_0$$

for the VE model. In both of these models, one can directly solve for the relaxation time  $\tau$ :

$$\frac{\Delta Q^{-1}(T)}{2\Delta f(T)/f_0} = \omega_0 \tau(T). \quad (5.4)$$

Given the striking similarity in the system's response to temperature and velocity perturbations, the obvious question is whether Eqs. 5.1-5.4 comprise a valid physical model of the response of the system if one replaces  $v \rightarrow T$ . Putting aside the question of the physics of the model for a moment, let us assume that the  $v \rightarrow T$  in Eqs. 5.1-5.4 procedure is a valid one and that there is an analogous relaxation time  $\tau_v$  for the response of the system to agitation brought on by changes in the velocity. Let us also rename  $\tau(T) \equiv \tau_T$  to emphasize that  $\tau_T$  and  $\tau_v$  are different characteristic times.

Just as we used Eq. 5.4 to show that  $\tau_T$  could have power law behavior (Sec. 3.2.1 and Fig. 3.3[B]), here we can Eq. 5.4 and its analog for velocity

$$\frac{\Delta Q^{-1}(v)}{2\Delta f(v)/f_0} = \omega_0 \tau_v(v) \quad (5.5)$$

to determine the relationship between the power laws of the two relaxation times  $\tau_T$  and  $\tau_v$ . Fig. 5.5 shows a plot of the left-hand side (LHS) of Eq. 5.4 vs.  $T$  beside a plot of the LHS of Eq. 5.5 vs.  $v$ . In the top two panels, the quantities  $\Delta Q^{-1}/(\Delta f/f_0) \propto \tau$  are plotted on log-log axes and in the middle two

panels they are plotted on Arrhenius axes (ordinate:  $\log(\tau_T)$  or  $\log(\tau_v)$  and abscissa:  $1/T$  or  $1/v$ ). It is fairly clear from a visual comparison of the two plotting schemes that the data are fit better to a power law than to an Arrhenius law in the unshaded region, which extends from  $T = 0$  ( $v = 0$ ) to  $T = 2T^*$  ( $v = 2v^*$ ). The best fit exponents for  $\tau_T \sim T^{-\alpha}$  and  $\tau_v \sim v^{-\zeta}$  are  $\alpha = 2.74$  and  $\zeta = 1.13$ , so the ratio is  $\alpha/\zeta = 2.42$ .

As has been discussed in Chapters 3 and 4, Eqs. 5.1 and 5.2 are insufficient to completely describe the data because the dissipation peak is too small to account for the total frequency shift. For our data, we have found the discrepancy  $A/A'$  to be in the approximate range 10-13 for the temperature dependence; for other TO experiments it can be in the range 1-100 [74, 101]. It is remarkable that roughly the same discrepancy is found for the ratio  $|\Delta Q^{-1}| / (\Delta f^{max} / f_0)$  if one considers the velocity dependent curves instead (see Fig. 5.4: the dissipation peak height and total frequency shift are roughly the same whether one looks at the temperature or velocity data). The exponents found from power law fits are independent of the discrepancy  $A/A'$ . However, if  $A/A' = 1$ , as would be predicted from the Debye or VE model, we should find that  $\omega_0 \tau_T = 1$  ( $\omega_0 \tau_v = 1$ ) when  $T/T^* = 1$  ( $v/v^* = 1$ ). The fact that  $\Delta Q^{-1}(T)/[\Delta f(T)/f_0]$  and  $\Delta Q^{-1}(v)/[\Delta f(v)/f_0]$  appear an order of magnitude smaller ( $\simeq 0.1$ ) at  $T/T^* = 1$  and  $v/v^* = 1$  is due to the discrepancy  $A/A' \approx 10$ .

The deviation from the Arrhenius law (middle panels of Fig. 5.5) appears to be more prominent in this experiment than in the data of Fig. 3.3. An explanation for this might be that at the very lowest temperatures (roughly  $T < T^*/2$ ) the data of Fig. 3.3 have come from a system that is in better equilibrium. At these temperatures  $\Delta Q^{-1}(T)/[\Delta f(T)/f_0]$  seems to be relatively smaller for the

(ringdown) data of Fig. 5.5 than for the (well-equilibrated) data of Fig. 3.3. Comparison of these two figures for low temperatures seems to support the idea that a component of the frequency shift is equilibrating quickly and causing  $\Delta Q^{-1}(T)/[\Delta f(T)/f_0]$  to be smaller relative to its value if one waits for a much longer time. We do not observe the same phenomenon of an ultra-slow relaxation after a change in the drive amplitude (or velocity), although it has been reported by Kojima's group [15].

We would like to explore the validity of this scaling behavior not just for the limiting cases shown in Fig. 5.4 but for the entire phase diagram of Fig. 5.3. Our strategy is to search for an appropriate variable  $X = X(v, T)$  that collapses the data  $f(v, T)$  and  $Q^{-1}(v, T)$  onto a single axis  $f(X)$  and  $Q^{-1}(X)$ . The Debye susceptibility suggests a strategy for hypothesizing a collapse axis. That model predicted that in the  $v \rightarrow 0$  limit the frequency would be well fit by  $A(1 + [\omega_0\tau_T]^2)^{-1}$  and the dissipation by  $A'\omega_0\tau_T(1 + [\omega_0\tau_T]^2)^{-1}$ , i.e., by Lorentzian functions of the variable  $\tau_T$ . Thus, a physically appealing collapse axis is a generalization of  $\tau_T$  to an effective relaxation time  $\tau_{eff}$  that depends on both  $T$  and  $v$ . In order to reproduce the limiting power law behavior of Fig. 5.5 ( $\tau_{eff} \rightarrow \tau_T$  as  $v \rightarrow 0$  and  $\tau_{eff} \rightarrow \tau_v$  as  $T \rightarrow 0$ ) the correct form is

$$\begin{aligned}\tau_{eff}^{-1} &= \tau_T^{-1} + \tau_v^{-1} \\ &= \tau_{0T}^{-1} \left( \frac{T}{T^*} \right)^\alpha + \tau_{0v}^{-1} \left( \frac{v}{v^*} \right)^\zeta\end{aligned}\quad (5.6)$$

where  $\tau_{0T}^{-1}$  and  $\tau_{0v}^{-1}$  are coefficients that will be determined by optimization of the collapse. The other parameters  $T^*$  and  $v^*$  refer to their limiting values as shown in Fig. 5.4(B) and (D). This expression can be interpreted as the sum of the relaxation rates of two independent, uncorrelated processes, one thermal and one in which the excitations are a result of agitation of the crystal. In the case of

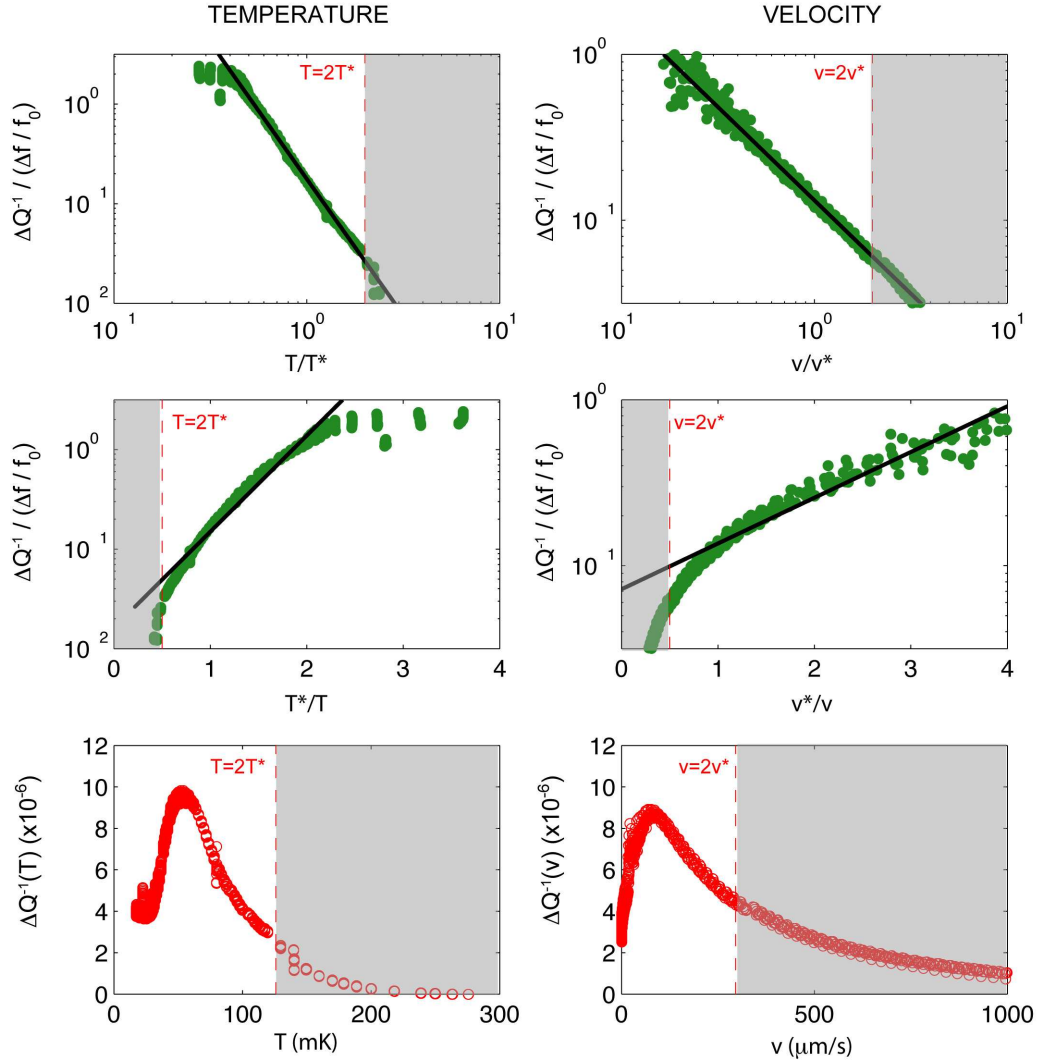


Figure 5.5: **Comparison of  $\tau_T$  and  $\tau_v$ .**

$\tau_T$  and  $\tau_v$  are defined empirically (within a multiplicative constant) by Eqs. 5.4 and 5.5. **(Top row)**  $\tau_T$  and  $\tau_v$  shown on log-log axes. Fits to power law behavior yields the exponents  $\tau_T \sim T^{-2.74}$  and  $\tau_v \sim v^{-1.13}$ . The valid range of the fit is roughly from zero temperature (velocity) up to  $2T^*$  ( $2v^*$ ), the non-shaded region. **(Middle row)**  $\tau_T$  and  $\tau_v$  shown on Arrhenius axes (ordinate:  $\log(\tau_T)$  or  $\log(\tau_v)$  and abscissa:  $1/T$  or  $1/v$ ) for comparison. In the non-shaded region it is clear that the quantities are better fit by power laws than by Arrhenius activated behavior. The black lines are guides to the eye and show how Arrhenius behavior would appear on this choice of axes. **(Bottom row)** Dissipation peaks in temperature (for  $v \rightarrow 0$ ) and in velocity (for  $T \rightarrow 0$ ) showing region where power law fits are valid.

Table 5.1: Parameters for unified collapse.

$\alpha$	$\zeta$	$T^*$	$v^*$	$\tau_{0T}$	$\tau_{0v}$
2.74	1.13	63 mK	148 $\mu\text{m/s}$	282 $\mu\text{s}$	213 $\mu\text{s}$

the scattering of electrons, this incoherent sum of individual rates is known as *Matthiessen's rule* [16].

Therefore we collapse the data of Fig. 5.3 onto a single axis characterized by  $\tau_{eff}$ . In Fig. 5.6, we show the result of this procedure, the remarkable collapse of 97% of the data of Fig. 5.3. The slightly different axis from Eq. 5.6 is explained below. We emphasize that although the motivation for the choice of the axis came from a specific model, this unified collapse of  $f(v, T)$  and  $Q^{-1}(v, T)$  onto simple related curves is an empirical fact, and any physical deductions about solid  $^4\text{He}$  phenomenology derived merely from its existence are not dependent on the validity of the analytic formulae or models used.

For the collapse,  $T^*$  and  $v^*$  are determined empirically, and  $\alpha$  and  $\zeta$  by fitting, from the  $T \rightarrow 0$  and  $v \rightarrow 0$  limiting cases of Fig. 5.5. That leaves two free parameters in Eq. 5.6 to be determined by an optimization of the collapse,  $\tau_{0T}$  and  $\tau_{0v}$ . Using an optimization algorithm written by Ethan Pratt, we find the values listed in Table 5.1. The values for  $\tau_{0T}$  and  $\tau_{0v}$  are quite close to one another, but more significantly both very close to the time scale of the probe frequency  $\omega_0^{-1} = 277 \mu\text{s}$ . This means that the data can be collapsed onto an axis given by

$$X = \left[ \left( \frac{T}{T^*} \right)^\alpha + \left( \frac{v}{v^*} \right)^\zeta \right]^{-1} \quad (5.7)$$

where all four of the parameters can be determined by the  $T \rightarrow 0$  and  $v \rightarrow 0$  limits! I proposed earlier that the Debye-type equations (5.1-5.4) might be valid for the replacement  $v \rightarrow T$  (i.e. the response of the system to agitation brought

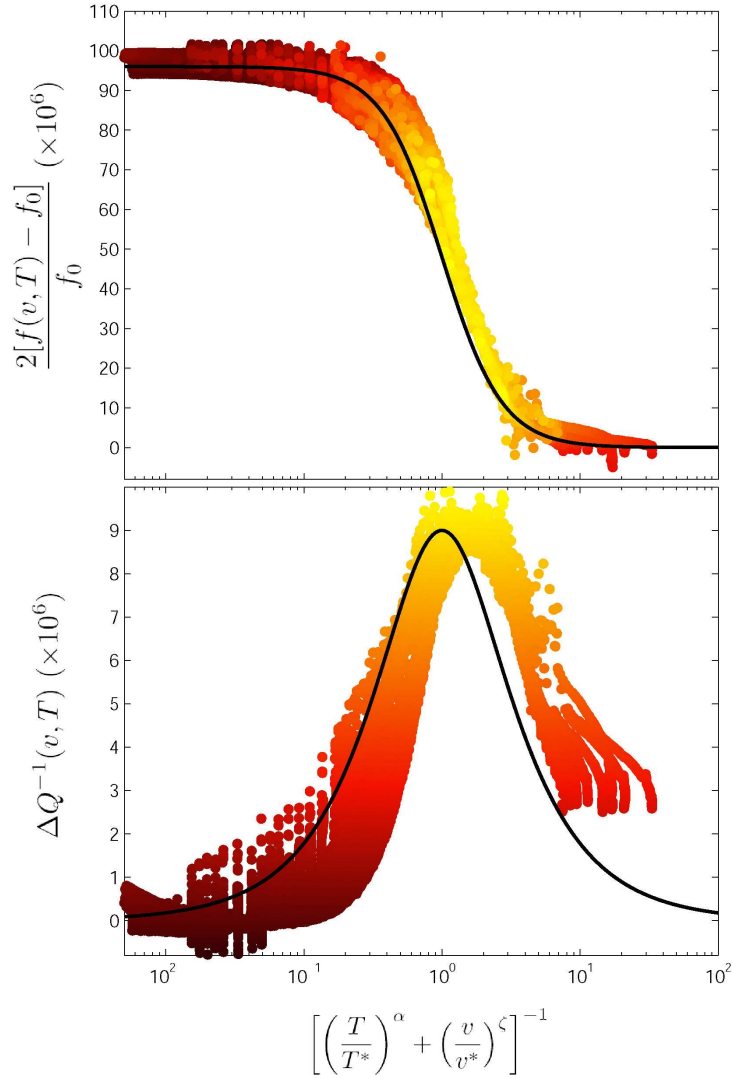


Figure 5.6: **Unified collapse of  $f(v, T)$  and  $Q^{-1}(v, T)$  onto a single axis.**

The choice of the axis  $X = \left[ \left( \frac{T}{T^*} \right)^\alpha + \left( \frac{v}{v^*} \right)^\zeta \right]^{-1}$  is discussed in the text. It corresponds, within a Debye model, to an effective relaxation time  $\tau_{eff}$ . The black curves are fits of the collapsed data to  $2\Delta f / f_0 \propto \Re[1 - i\omega_0\tau_{eff}]^{-1}$  and  $\Delta Q^{-1} \propto \Im[1 - i\omega_0\tau_{eff}]^{-1}$ , where the proportionality constant is different for the frequency and dissipation (see comment following Eq. 5.9). The axis of Fig. 5.6 is proportional to the inverse of  $T$  and  $v$ , and so the low-temperature, low-velocity state (the 'supersolid') is at the extreme right of the figure. The collapse of the frequency data is best for  $X > 1$  (low  $T$  and low  $v$ ); for  $X < 1$  it is only good within about an order of magnitude. The collapse of the dissipation data is best near the peak ( $0.4 < X < 4$ ) and only good within about an order of magnitude outside these limits.

on by changes in the velocity was similar to that induced by changes in the temperature). In such a scenario, the variable  $X = \omega_0 \tau_{eff} = \omega_0 (\tau_T^{-1} + \tau_V^{-1})^{-1}$ . Thus, the reduction of the Eq. 5.6 collapse to that of Eq. 5.7 reflects the trivial result that in the  $v \rightarrow 0$  limit,  $X(T^*) = \omega_0 \tau_{eff}(T^*) = 1$  (and similarly in the  $T \rightarrow 0$  limit that  $\omega_0 \tau_{eff}(v^*) = 1$ ). However, what is decidedly not trivial is the fact that this works for any combination of  $T \neq 0, v \neq 0$ , let alone that the scheme works whatsoever for the velocity axis.

The shortcoming of the expression Eq. 5.7 in its ability to collapse the data is its failure to describe the “superpeak” [the point of maximum global dissipation in the vicinity of  $(T^*, v^*)$ ]. This may represent a breakdown of the idea that the relaxation rates  $\tau_T^{-1}$  and  $\tau_v^{-1}$  add incoherently.

## 5.2.2 Temperature Dependence of Critical Velocity

Models of solid helium that attribute the TO frequency shift  $\Delta f(T)$  to a superfluid transition naturally interpret the suppression of  $\Delta f(T)$  with increasing TO rim velocity as evidence of a superfluid critical velocity, in analogy to experiments using a TO to study superfluid critical velocities [90]. As has been discussed, the size of the supersolid critical velocity, of the order of  $10 \mu\text{m/s}$ , is many orders of magnitude smaller than its counterpart in superfluid  $^4\text{He}$ , and so we would like to study the temperature dependence of the supersolid  $v_c$  in order to better understand this perplexing issue. We can use the contour plots to deduce the temperature dependence of the supersolid  $v_c$  in the manner discussed in the introduction to Sec. 5.2. Figure 5.7 reproduces the  $f(v, T)$  contour plot on a linear-linear scale in  $v$  and  $T$ . The red dashed line is the constant

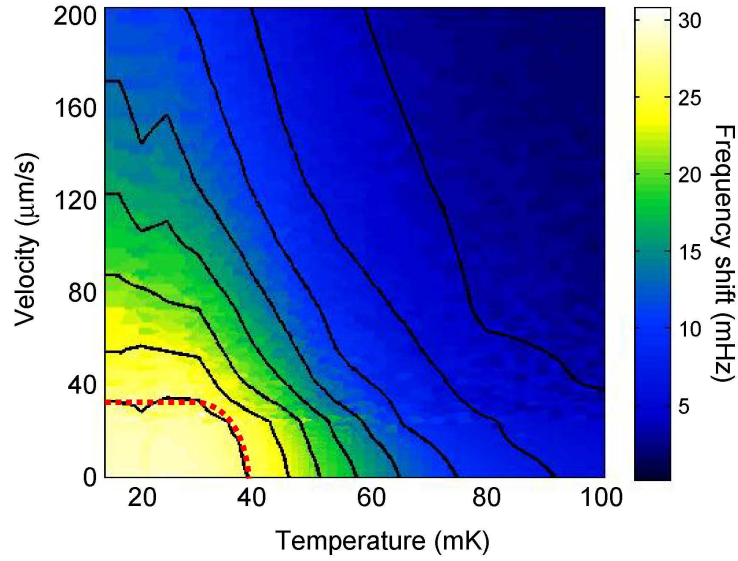


Figure 5.7:  $v_c(T)$  as represented by a single contour.

The critical velocity  $v_c(T)$  is shown as the dashed red contour. It is determined by the condition that the frequency shift is reduced from its low- $v$ , low- $T$  value  $\Delta f^{max}$  by 5% (an arbitrary, but reasonable, designation for the definition of  $v_c$ ). Note that the contour plot is on a linear scale in both  $T$  and  $v$ .

frequency contour for which  $\Delta f$  is diminished by 5% from its maximum value  $\Delta f^{max} \equiv \Delta f(T \rightarrow 0, v \rightarrow 0)$ . It is reasonable to interpret this curve as  $v_c(T)$  for the purposes of comparison to the superfluid results. It appears that  $v_c(T)$  for solid helium is roughly temperature independent between  $T = 0$  and  $T \approx 35$  mK, at which point it begins to decrease sharply with increasing temperature as  $T^*$  is approached from below.

The success of the scaling behavior in Sec. 5.2.1 also suggests a strategy for defining a critical velocity. One can define a constant  $X_c$  for which  $f(X_c)$  is reduced from its high  $X$  (low  $T$  and  $v$ ) value  $f^{max}$  by some amount, perhaps the minimum resolvable change in  $f$  from  $f^{max}$  above the noise. Along the critical contour  $f(X_c)$  we will have that  $(T/T^*)^\alpha + (v/v^*)^\zeta = \text{const} = X_c^{-1}$  and therefore

along that contour  $v \equiv v_c(T)$ , where

$$v_c(T) = v_{c0} \left[ 1 - \left( \frac{T}{T_0} \right)^\alpha \right]^{1/\zeta}, \quad (5.8)$$

where  $v_{c0} = v^* X_c^{-1/\zeta}$  and  $T_0 = T^* X_c^{-1/\alpha}$ . This power-law decay of the critical velocity is to be compared with the expression for the critical velocity due to thermally-activated phase slips, which decays linearly in the temperature. The domain of validity of Eq. 5.8 is for  $T > T_0$ , so it depends on how  $X_c$  is chosen.

### 5.2.3 Velocity Hysteresis

In [14], Aoki, Graves and Kojima first reported the observation of hysteresis in the TO frequency shift upon cycling of the drive amplitude (and therefore the rim velocity of the TO). This result was reproduced by Reppy's group [103], and ours. I include here an example at  $T = 21.6$  mK of the type of hysteresis loop we encounter when starting at a high drive level stepping the drive down, waiting for equilibrium at that particular level, continuing to step down until the lowest drive level is reached, and then repeating the process in the opposite direction.

I should point out additionally that all of the preceding data in this chapter were taken with ringdowns, and so are equivalent to the the lower curve of Fig. 5.8. Most of the results of this chapter would be quantitatively different if the data were taken during ringups of the TO, but this was technically too challenging. We do not expect that qualitatively the results would be very different.

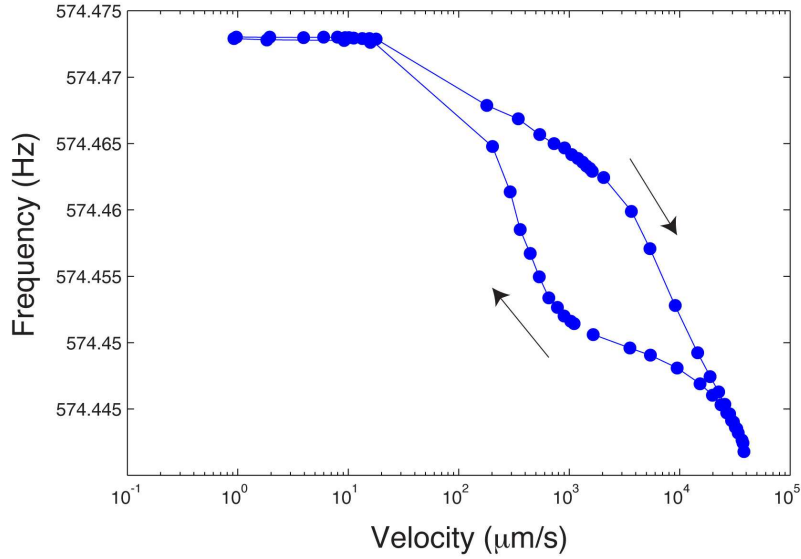


Figure 5.8: **Velocity hysteresis.**

The black arrows show the direction of change of velocity between data points. The temperature is 21.6 mK.

### 5.3 Summary and Discussion

In this chapter, we used a new, efficient technique to map the temperature and velocity dependence of the TO frequency shift and dissipation. The precision of the data led to several new discoveries about the role of velocity in the TO experiments. The main theme unifying the discoveries is the remarkable symmetry of the observables along the temperature and velocity axes, leading us to ask if the same excitations of the  $^4\text{He}$  solid generated by temperature might also be generated by agitation of the solid (for which the TO rim velocity serves as a convenient proxy). The central discoveries are the following; all are independent of any models of the behavior of the solid:

1. There is a peak in  $Q^{-1}(v)$  at  $v = v^*$  and a shift in  $f(v)$  (for  $T \rightarrow 0$ ) that match their counterparts  $Q^{-1}(T)$  and  $f(T)$  (for  $v \rightarrow 0$ ). The peak height-

to-total shift ratio  $|\Delta Q^{-1}| / (\Delta f^{max} / f_0)$  is roughly the same for both variables.  $\Delta Q^{-1}(\zeta) / (\Delta f(\zeta) / f_0)$  can be better fit by a power law than an Arrhenius law, whether  $\zeta$  is temperature or velocity. The behavior of that quantity is  $\sim T^{-\alpha}$  and  $\sim v^{-\zeta}$ , where  $\alpha = 2.74$  and  $\zeta = 1.13$ .

2. There is a “superpeak” - a global maximum in the dissipation - in the vicinity of the point  $(T^*, v^*)$
3. The symmetry in the velocity and temperature axes can be expressed by collapsing nearly the entire contour plots of either  $f(v, T)$  or  $Q^{-1}(v, T)$  onto a single axis  $X = X(v, T)$ , where  $X \equiv [(T/T^*)^\alpha + (v/v^*)^\zeta]^{-1}$ . This can be accomplished using only the empirically determined  $T^*$  and  $v^*$  and the fits to  $T^{-\alpha}$  and  $v^{-\zeta}$  in the limiting cases  $T \rightarrow 0$  and  $v \rightarrow 0$ . This collapse fails in the vicinity of the superpeak.

In addition to these new discoveries, we also observed hysteresis in the TO frequency shift when cycling the drive amplitude.

When we discussed whether the  $T \rightarrow v$  substitution was valid for the Debye expressions for  $f$  and  $Q^{-1}$  (Eqs. 5.2 and 5.3), what was implicit was the question of whether an equivalent *nonlinear* susceptibility  $\chi(\dot{\theta}, T)$  (with  $\dot{\theta} \propto v$ ) would be suitable for the description of the data on the two axes  $v$  and  $T$ . Formally, such a function could not be derived in the same manner as in Eqs. 3.1 through 3.6, because that process was manifestly linear. One way to determine such a function would be to measure the angular displacement  $\theta$  as a function of drive torque  $\Gamma$  for a sequence of temperatures at each torque, and then fit the result to a function such as

$$\theta(T) = \chi^{(1)}(T)\Gamma + \chi^{(3)}(T)\Gamma^3 + \dots$$

(The terms  $\chi^{(k)}\Gamma^k$ , for  $k$  an even integer, are absent because of symmetry considerations). The terms of  $O(\Gamma^3)$  and higher would constitute the nonlinear susceptibilities and the linear term  $\chi^{(1)}$  would correspond to one of the models in Chapter 3. However, as was shown in Fig. 5.6, the collapsed data could be reasonable well fit by a single function with

$$\begin{aligned}\frac{2\Delta f(v, T)}{f_0} &= \Re \left[ \frac{A}{1 - i\omega_0\tau_{eff}(v, T)} \right] \\ \Delta Q^{-1}(v, T) &= \Im \left[ \frac{A}{1 - i\omega_0\tau_{eff}(v, T)} \right]\end{aligned}\quad (5.9)$$

provided we are allowed to account for the discrepancy in the magnitudes by one of the modifications discussed in Chapter 3 (i.e. inclusion of a superfluid term or a stretching exponent  $\beta$ ). The physical implications of using such a function is an issue that will have to be dealt with, particularly the significance of the power law behavior of  $\omega_0\tau_{eff} = [(T/T^*)^\alpha + (v/v^*)^\zeta]^{-1}$ .

The existence of the superpeak is also a confounding issue. We proposed that it might represent the breakdown of the idea that the relaxation rates  $\tau_T^{-1}$  and  $\tau_v^{-1}$  add incoherently. In the case of electron scattering, this would represent the (well-known) failure of Matthiessen's rule, which in general would result in an inequality for the total relaxation rate  $\tau_{tot}^{-1}$ ,

$$\tau_{tot}^{-1} > \tau_A^{-1} + \tau_B^{-1}, \quad (5.10)$$

where  $A$  and  $B$  refer to two distinct electronic scattering processes (e.g. scattering from impurities and from phonons). However, in our case, it is unlikely that the analog of Eq. 5.10, i.e.  $\tau_{eff}^{-1} > \tau_T^{-1} + \tau_v^{-1}$ , could be used to describe the superpeak, since such an expression cannot have any effect of the *maximum value* of the quantity that depends on  $\tau_{eff}^{-1}$  when the dependence is of the form given by Eq. 5.9.

Before continuing to discuss the significance of the velocity axis, let us address the contentious issue of the critical velocity. The magnitude of the reported critical velocity is of the order of  $10 \mu\text{m/s}$  and appears to be insensitive to the geometry of the cavity containing the solid  $^4\text{He}$ . This is three orders of magnitude smaller than the Feynman critical velocity (Eq. 1.11), obeyed by superflow in channels of width  $\sim 100 \mu\text{m}$ , and six orders of magnitude smaller than typical critical velocities for superflow through apertures of nanoscale dimensions (Eq. 1.12), so interpretation of the supersolid critical velocity in terms of vortex creation requires introduction of a new idea about vortex generation in the solid. This has been addressed by Saslow [106]. In these two known mechanisms for vortex creation, the critical velocity in superfluid  $^4\text{He}$  may be temperature-dependent or independent. In the case of a phase-slip critical velocity,  $v_c$  decreases linearly with temperature over a large range of  $T$  below the superfluid transition ([41] and Fig.1.4[A]), consistent with the thermal activation of the vortex motion at a rate  $r = \exp[E(v)/k_B T]$  over a velocity-dependent energy barrier  $E(v)$ . At very low temperatures ( $< 200 \text{ mK}$ ), the phase slip critical velocity can become temperature-independent in a regime where quantum tunneling of vortices dominates thermal activation [41]. The temperature dependence of what might be considered the critical velocity in the supersolid experiments, as discussed in Sec. 5.2.2, does not appear to be in agreement with the known temperature-dependence (or independence) of vortex-related critical velocities in superfluid  $^4\text{He}$ .

If indeed what is observed turns out to be a critical velocity, one reason why the critical velocity might seem so low is that the rim velocity of the TO is much smaller than the actual velocity of the flow of the supercomponent. The observed critical velocities are insensitive to the size or shape of the con-

tainer and equally insensitive to whether the sample is grown in the bulk or in a porous matrix, implying that the physical channels available to the superflow are perhaps not those defined by the geometry of the container. A torsional oscillator with an annular flow path interrupted by a barrier with a tiny aperture can act as a “velocity multiplier” of the flow through the aperture, as in the experiments described in [90]. If the superflow in the helium crystal takes place along constrictions (such as grain boundaries or dislocation cores) the actual flow velocity could be much higher because of the greater hydrodynamic inductance along such paths.

One can follow a constant-frequency or constant-dissipation contour by simultaneously decreasing the velocity and increasing the temperature. As far as the TO experiments are concerned, along a contour *the solid  $^4\text{He}$  is in the same state*. This is a strong argument in favor of the idea that temperature and mechanical agitation of the solid control the same bath of excitations. In [87], it was shown that a particular driven, glassy, athermal system, a foam (consisting of bubbles of different sizes) sheared at a rate  $\dot{\gamma}$ , can behave as a thermal system with the shear rate  $\dot{\gamma}$  playing the role of an effective temperature. In an equilibrium system, the viscosity is related to the integral of the shear stress autocorrelation function

$$\eta_{xy} = \frac{A}{T} \int_0^\infty dt \langle \delta\sigma_{xy}(t) \delta\sigma_{xy}(0) \rangle \quad (5.11)$$

where the integrand (autocorrelation function) depends on  $\dot{\gamma}$ , and  $A$  is the area over which the shear is being applied. This equation serves to define the effective temperature in the *non-equilibrium* case as it is related to fluctuations in the shear stress. From the results of [87], we have some confidence that the temperature-dependent viscosity of the solid  $^4\text{He}$  (perhaps more accurately the viscosity of the excitations in the solid), which would be related to the super-

solid transition, could in principle also have a shear-rate (or velocity) dependent viscosity  $\eta(\dot{\gamma})$  that mimicks  $\eta(T)$  and its role in the behavior of the observables of the system (the TO frequency shift and dissipation). In the vortex fluid model, the viscous drag on the vortices is  $\eta_v = \hbar n_v$ , with  $n_v$  the area density of thermal vortices. It is possible that the TO observables are related along the velocity (shear rate) and temperature axes because the agitation of the solid can change the density of vortices above  $T_c$ .

It is clear from the work of Paalanen [88] and more recently from Day and Beamish [43] that at some level the low-temperature increase of the shear modulus must be related to the TO frequency shift because of the qualitatively similar effects when changing the temperature and when changing the TO velocity/strain/shear rate. The work of this chapter and the ideas of [87] suggest that the temperature and velocity/shear rate can in some sense be thought of in equivalent terms. I think that elucidating the relationship between the stress in the  $^4\text{He}$  solid and the TO frequency shift is one of the key steps to solving the supersolid puzzle, and in the next chapter I propose an experiment designed to address this issue.

## CHAPTER 6

### CONCLUSIONS AND OUTLOOK

#### 6.1 Summary

Three years ago when we began our studies of solid helium, the field was still very much dominated by the vocabulary of superfluidity: terms like “critical velocity” and “non-classical rotational inertia” were used rather matter-of-factly. These terms are useful and evocative, but remain merely useful until definitive proof of the existence of superfluidity in the helium solid is found. Since that time, there have been many experiments that have forced us to take a second look at our ideas about whether the state of solid helium below 100 mK is a true superfluid, in three dimensions or otherwise. There have been no studies affirming the existence of persistent currents and there have been roughly equal numbers of negative and positive results in the search for dc flow. There is no evidence for Bose-Einstein condensation from either X-ray or neutron scattering. There is only indirect evidence of the existence of quantized vorticity. The existence of a dissipation peak at the transition is present in the 2-D superfluid transition but certainly not in any 3-D superfluid transitions studied with a torsional oscillator.

I have tried to present the results of this dissertation in a way that reflects our genuine perspective of the mysterious phenomenology of solid helium, that is, without being wedded to a particular model of the solid. In Chapter 3, I have attempted to present the TO studies of solid helium in the general framework of linear response, that of the rotational susceptibility of the TO-helium system to an external torque, an idea first suggested to us by Nussinov et al. I have

included some of our early work on attempting to fit our data to various models of the behavior in the solid helium. In Chapter 4 I presented our studies of the relaxation dynamics of solid helium within the TO. We discovered the phenomenon of ultraslow relaxation while we were attempting to measure the equilibrium properties of the solid helium. We found that the relaxation times of both the resonant frequency and dissipation increased identically as the temperature was lowered below the transition temperature of the supersolid state. We undertook a more detailed study of the dynamics of the supersolid state and found that the interplay of the dynamics of the TO frequency shift and dissipation were more subtle than could be described by many simple models presented in Chapter 3.

In Chapter 5 I described our study of another aspect of the dynamics of the solid helium-TO system, namely the velocity dependence of the TO frequency shift and dissipation. Employing a new technique for efficient mapping of the velocity/temperature phase diagram, we found a remarkable symmetry in the behavior along the two axes. The dependence of the TO resonant frequency and dissipation on velocity was dissimilar to any known critical velocity behavior in superfluid  $^4\text{He}$ . This led us to ask if the observed TO phenomena could be explained by a model in which both thermal and mechanical agitation of the system controlled a single set of excitations, which in turn might control the global phase coherence of the supercomponent, if it indeed exists.

## 6.2 Perspectives

This section will be divided roughly into the following categories:

1. What is well-established about the low-temperature behavior of solid  $^4\text{He}$
2. What is contentious
3. What we have contributed

**What is well-established.** The most comprehensive data in recent years we have come from the torsional oscillator experiments. The primary result from these experiments has been that the TO frequency shift and excess dissipation depend strongly on the way in which the helium sample has been prepared. The observed NCRIf values span a large range, from about 0.01% up to 20%. For blocked capillary samples, this number increases as the amount of time required to form the sample decreases. The NCRIf seems generally to decrease when the sample is annealed, though there are exceptions to this observation as well. On the one hand, the NCRIf can change by an order of magnitude when grown in similar geometries but different materials (coin silver [AgCu] vs. BeCu) but, on the other hand, can be the same magnitude when grown in the bulk and when grown in a porous matrix with 1000 times the surface-to-volume ratio. The NCRIf is larger when grown by the blocked capillary method than by other methods (constant pressure and constant temperature). The general conclusion is that disorder plays an important role, but what kind of disorder, let alone how to quantify it, is still an open question. However, structural measurements, taken in conjunction with TO measurements, seem to indicate that NCRIf is the same in highly polycrystalline samples and in (quasi-) single-crystal samples, effectively ruling out grain boundaries as the primary explanation for the TO frequency shift.

Based on a large body of literature on the way  $^3\text{He}$  interacts with crystal dislocations in  $^4\text{He}$ , it is believed that dislocations are the most relevant type

of disorder for the TO experiments. The shear modulus measurements of Day and Beamish (and earlier of Paalanen et al.) are consistent with the idea that at lower temperatures  $^3\text{He}$  impurities can act as additional pinning centers for the dislocations, thereby increasing the shear modulus of the solid  $^4\text{He}$  as the temperature is lowered. The TO frequency shift and shear stiffening have very similar temperature,  $^3\text{He}$ , and annealing dependences, and since the role of dislocations is well understood in the context of shear stiffening it is reasonable to assume that the dislocation network plays a similarly important role in the TO experiments.

**What is contentious.** Although the TO frequency shift and shear stiffening must be related on some level, the magnitude of the expected frequency shift due to shear stiffening alone appears to be too small. This issue needs to be resolved and we propose an experiment to do so in the next section. Of course, asking whether the shear stiffening can explain the TO frequency shift is akin to the more general question of whether there is a non-supersolid explanation for the TO experiments. As of yet, the only evidence of a superfluid comes from the blocked annulus experiments, and it is indirect evidence. The heat capacity measurements are also open to interpretation. Some researchers have been able to fit the data by including a linear term added to the Debye  $T^3$  dependence, which is suggestive of the presence of a glassy component. The physical origin of the peak in the heat capacity is also unknown; although too small to be explained by the entropy of a BEC between  $T = 0$  and  $T = T_c$ , it was interpreted as the thermodynamic signature of the 'supersolid' and shown to be present in a stress-free sample (liquid and solid in coexistence), indicating that the phenomena associated with the supersolid are intrinsic to solid helium and the role of stress and dislocations is only to enhance the effect. Finally, returning to the TO

measurements, attempts to fit the TO frequency shift and dissipation to simple models of the rotational susceptibility  $\chi$  have been hampered by one outstanding empirical feature: the ratio of the dissipation peak to the (fractional) frequency shift,  $|\Delta Q^{-1}| / (\Delta f^{max} / f_0)$ , varies over two orders of magnitude in the body of TO experiments, which may suggest an additional degree of freedom not accounted for by simple models of  $\chi$ . The dependence of this quantity on the variables available to the TO experiments is not well known, although some measurements indicate that it could be a decreasing function of the external pressure (or equivalently the density or molar volume).

**What we have contributed.** The overarching question is whether phenomena present in the TO experiments have either a supersolid or non-supersolid origin, or whether the eventual explanation will necessarily contain elements of both. In a set of experiments designed to study the relaxation dynamics of solid  $^4\text{He}$ , we showed principally that the characteristic relaxation time of the TO frequency and dissipation lengthened as  $T \rightarrow 0$ . This result was consistent with other observations of long relaxations in the TO behavior, in the behavior of the solid during the annealing process, and in the slow rearrangement of crystallites visible in the X-ray scattering experiments. Such behavior might reflect the existence of a glassy component of the solid  $^4\text{He}$ : it has been proposed that the crystal dislocations might form an ensemble of tunnelling systems, in analogy to the two-level systems that have been successful in predicting the acoustic and thermal properties of structural glasses. Looking at these relaxations in more detail revealed that the response of the TO had a “fast relaxation” that responded immediately to a change in the mixing-chamber temperature and a subsequent “slow relaxation” after the solid  $^4\text{He}$  had come into thermal equilibrium that lengthened as  $T \rightarrow 0$ . We speculated that this might represent the

distinct dynamics of a superfluid component and a glassy component.

In superfluids, the velocity of the superflow plays a fundamental role. The critical velocity of superfluid  $^4\text{He}$  can vary by three orders of magnitude, depending on the geometry of the flow path, the temperature, and the mechanism for the creation of elementary excitations from the superfluid ground state. By comparison, the 'critical velocity' of solid  $^4\text{He}$  as measured by the TO experiments is (a) extremely small and (b) insensitive to the temperature, and to container geometry. Our experiments showed that the behavior of the TO, in both the frequency and the dissipation, was surprisingly symmetric along the velocity and the temperature axes. A similar effect in the shear stiffening occurs: the stiffening is suppressed by increasing the strain amplitude  $\epsilon$  beyond a critical value  $\epsilon_c$ . The discrepancy with superfluid critical velocities, the symmetry of the TO behavior along the  $v$  and  $T$  axes, and the qualitative similarity to the results of the shear modulus experiments led us to propose the question of whether the velocity is the correct variable with which to understand the TO experiments, or whether there is a more appropriate quantity. This question remains unanswered but will hopefully come to the forefront of the field if some of the proposed experiments of the next section can be performed.

### 6.3 Future Experiments

On the experimental side, I think there are a few classes of experiments that need to be pursued. The first is a better study of the frequency dependence of the response of solid helium to rotation. The second is an experimental reconciliation of the tantalizingly similar temperature- and amplitude-dependence of

the TO frequency shift and the shear modulus. Third, a new approach to the question of dc (super)currents is required.

### 6.3.1 Frequency Dependence of Rotational Susceptibility

The advantage of the high-Q torsional oscillator is its ability to resolve extremely small changes in the resonant frequency due to, for example, any extra inertial loading. Because of that feature, it is also equivalently difficult to operate the oscillator away from its resonant frequency. We attempted to measure the rotational susceptibility of the TO-helium system *directly* by operating the TO off-resonance, but we found that even with the additional sensitivity of our SQUID-based sensor we could not resolve the change in  $\chi$  due to the supersolid much more than 50 Hz above or below the resonant frequency  $\sim 574.475$  Hz. The results of this study are summarized in Fig. 6.1. It is not easy to make general statements about the frequency-dependent behavior when the data is limited to a 100-Hz bandwidth!

A solution to this problem might be a variable-resonant frequency torsional oscillator. There are roughly two ways to accomplish this: by changing the moment of inertia of the bob or by changing the spring constant of the torsion rod. The latter could be accomplished by clamping of the torsion rod in different places using a tight-fitting sleeve, and the former by changing the distribution of mass away from the axis of rotation using some sort of mechanical actuation. A possible realization of the second scheme will be shown.

The two most important issues in the design of such a variable frequency TO are the following:

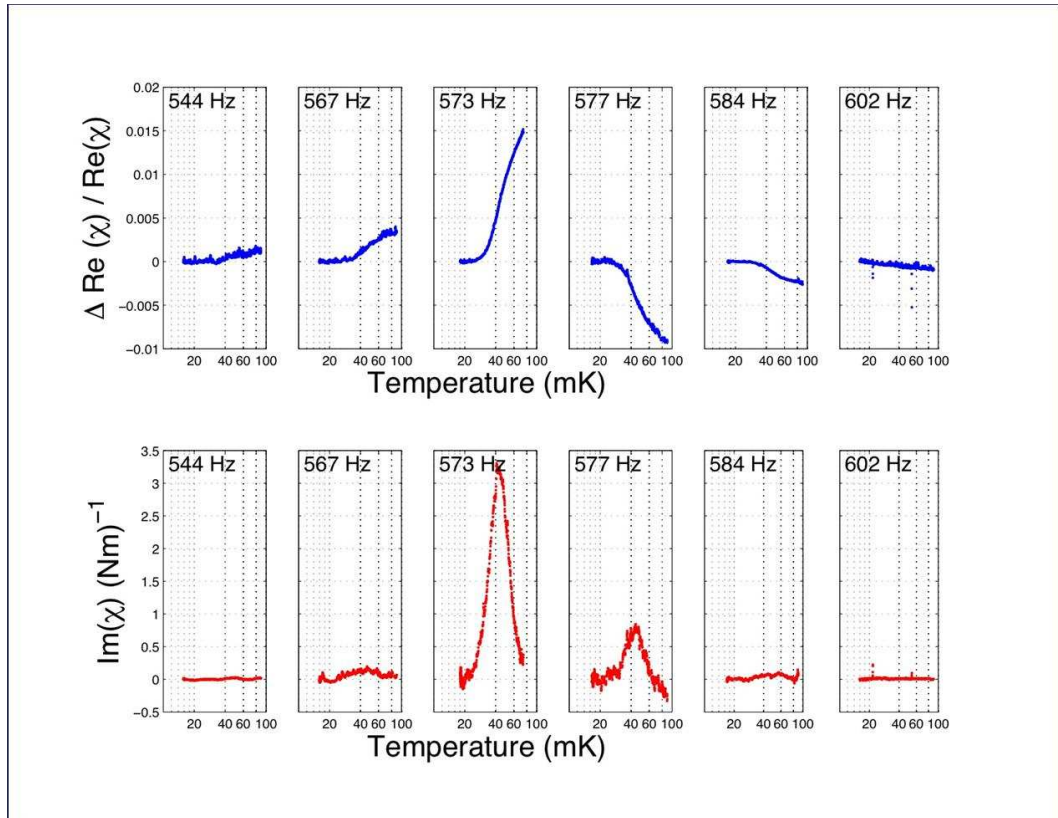


Figure 6.1: Frequency dependence of rotational susceptibility.  
[63]

1. Can the frequency be changed at low temperature (i.e.  $< 1$  K) so that the helium crystal need not be altered irreversibly when adjusting the frequency?
2. Can the frequency be made to change over a large enough range (and can the Q of the oscillator simultaneously be kept large enough) to make this effort worthwhile?

Future experiments should employ the persistent-current based system if precision better than  $10^{-13}$  m is required.

A second possibility for studying the frequency dependence of the rotational susceptibility would be to build several similar torsional oscillators that could

be studied simultaneously during a single cooldown. They would share a common fill line and have identical sample geometries but have resonant frequencies that span, say, one full decade (e.g. 100 to 1000 Hz), perhaps by varying the moment of inertia of each torsion bob. A variation of this idea would be to build several dual-mode oscillators [14], doubling the number of frequencies that could be studied. This idea may seem unreasonable because of the complications due to having the oscillators in close proximity (e.g. a vibration block for each TO would probably be required [Fig. 2.2]), but I do not imagine it would be any more complicated than building a single variable-resonant frequency TO or a TO that could simultaneously measure the inertia stress (next section). The important idea of both of the proposed experiments in this section is to vary a single parameter (here  $\omega$ ) and study *the same sample*. This is one aspect of the body of TO experiments that is lacking.

### 6.3.2 Simultaneous Determination of Rotational and Shear Susceptibility

An outstanding question is how the low-temperature increase of the shear modulus is related to the TO resonant frequency shift. Finite-element calculations have suggested that even the largest shear modulus changes (up to about 30%) are far too small to produce the size of the observed frequency shift. It is also difficult to imagine how the shear stiffening in the torsion bob can produce a frequency *increase*, since stiffening of the material in the bob should entrain more mass in phase with the TO itself and therefore look like an increase in the moment of inertia. Finally, the blocked annulus experiments have been shown to

nearly completely eliminate the frequency shift, implying that the block affects the global behavior of the helium solid, whereas the effect of introducing the block should have only a local effect on the elastic properties. On the other hand, the striking similarity in the temperature dependence and the strain/velocity dependences of the two phenomena suggest that they must be related on some level.

The conclusions of the previous paragraph based on calculations and intuition, but the only way truly to know is to do an experiment that can measure both the rotational susceptibility of the  $^4\text{He}$  as well as the shear strain induced by acceleration of the container. There are two experiments that might accomplish this.

1. Embed shear strain sensors in the cavity of a torsional oscillator. The shear strain sensor is just a piezoelectric crystal and can be made narrow enough to fit in an annular cavity (so chosen because such a geometry appears to give rise to the largest TO frequency shift). For details of the operation and utility of the piezo crystal as a shear sensor, see the work of Day and Beamish [43]. The piezo crystal should be placed where it can detect the maximum strain amplitude; one face should be mounted to the outer (or inner) wall of the annular cavity and the other face should be positioned at the midpoint between the two walls.
2. Construct a torsional oscillator such that the the inner wall of the annular cavity can be fixed relative to the outer wall. This experiment would be designed to operate in two modes, one in which the inner wall and outer wall would move in unison (TO mode) and the other in which the inner wall would be fixed and the outer wall could be be moved relative to the

inner wall (shear mode). This is a more difficult experiment since it is highly likely that the  $Q$  of the oscillator would be severely degraded by the necessary complexity of the design.

Finally, in [43] only the real part of the shear susceptibility was reported. One would like to know how an analogous linear response theory for the shear susceptibility  $\chi_{shear}$  would apply to the measurements of Day and Beamish. In particular, one would like to know how some of the features of the TO rotational susceptibility (for example, the large range in the value  $|\Delta Q^{-1}| / (\Delta f^{max} / f_0)$  from different TO experiments) map to the analogous features of  $\Re[\chi_{shear}]$  and  $\Im[\chi_{shear}]$ .

### 6.3.3 Mass Transport through Superfluid-Solid Junctions

At the time of writing, the current experiment on our cryostat is one designed to measure the flow of  $^4\text{He}$  atoms from the superfluid into and then out of the solid. It is an idea conceived of and executed entirely by Ethan Pratt. The idea is similar in concept to that of the experiment of Ray and Hallock (described in Sec. 1.4.5 and [97]), whereby a superfluid-solid junction can be created at constant pressure and temperature by coupling a bulk cavity and a volume containing porous material. The onset of solidification of the  $^4\text{He}$  in the pores can be suppressed by some 5 bar, and so at the right place in the phase diagram one can have the coexistence of superfluid and solid in adjoining volumes.

Whereas the experiment of Ray and Hallock used a pressure difference across the superfluid-solid-superfluid system to inject  $^4\text{He}$  atoms from the superfluid into the solid, the scheme shown in Fig. 6.2 is quite different. It uses the finite

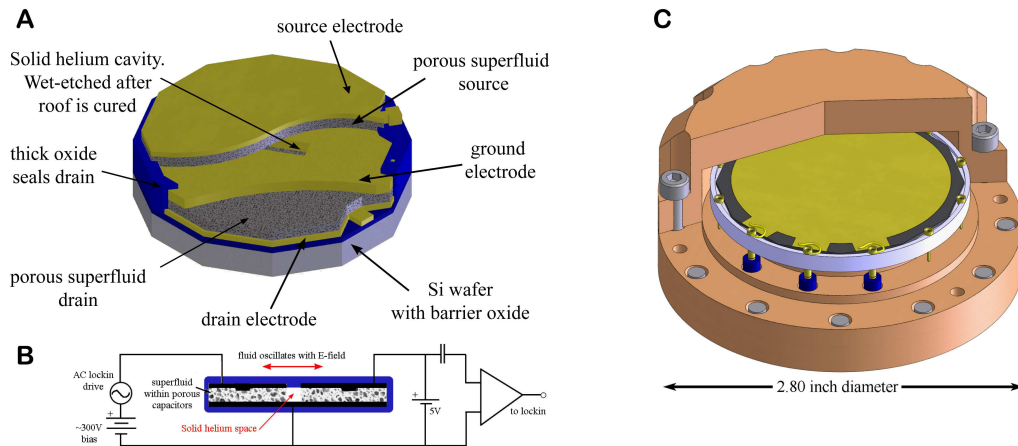


**Figure 6.2: Proposed superfluid-solid junction experiment.** (A) Fabrication steps and components of nanoporous device. (B) Device mounted in high-pressure cell. (C) Principle of operation.

polarizability of the helium atoms to create electrostatically a chemical potential difference across the superfluid-solid junction; it accomplishes this by confining the superfluid in a very thin nanoporous matrix between the plates of a gigantic capacitor ( $\sim 30$  nF) placed to one side of the solid  $^4\text{He}$ . An identical capacitor pair is located on the other side of the solid, and atoms can (in theory) be driven from one nanoporous volume through the solid  $^4\text{He}$  and detected as a change in the dielectric constant of the other pair.

This scheme is advantageous over many of the other dc flow experiments because we will not need to push on the crystal lattice to create a chemical potential difference. The Ray-Hallock configuration suffered from large heat leaks due to the necessity of maintaining one end of the column of normal fluid/superfluid close to 4 K and the other end at low temperature; this limited the base temperature of their study to be above the range of the TO frequency shift. Because we push on the superfluid-solid junction electrostatically, we do not anticipate having the same set of problems. If the technique is successful,

there are many other interesting experiments that can then be done by changing the geometry and complexity of the flow paths. The junctions can be made very small by modern fabrication techniques, opening the possibility for microscale and nanoscale investigation of the flow properties. If true dc superflow is shown to exist, the junctions could be configured to produce interference devices, such as a superfluid-supersolid based-SQUID.

## 6.4 Conclusions

The proposal that solid  $^4\text{He}$  might be a supersolid of the type described by Andreev and Lifshitz, Chester, and others appeared to have been vindicated by the TO experiments of Kim and Chan in 2004. Since the initial excitement over the prospect of a new state of quantum matter, however, there have been no experiments providing *direct* evidence that there exists a component of solid  $^4\text{He}$  that behaves as a superfluid. Consequently, the question at the forefront of every researcher's mind remains whether solid  $^4\text{He}$  can be considered a supersolid.

I think that a supersolid mechanism, at least in the Andreev-Lifshitz-Chester sense, cannot be the *complete* explanation for the TO experiments. Our data show a symmetry in the TO resonant frequency and dissipation dependences on temperature and velocity, suggesting that the two dependences have the same physical origin. This idea is reinforced by the similar qualitative dependences of the low-temperature shear stiffening and the TO frequency shift on annealing,  $^3\text{He}$ , and shear rate/velocity. One possible explanation is that there are excitations of the solid  $^4\text{He}$  that respond equivalently to agitation and to thermal perturbation. The precise microscopic origin of these putative excitations

is not known, but it has been suggested that perhaps they represent an ensemble of the possible structural configurations of crystalline dislocations or grain boundaries, or even of frozen-in glassy regions. Possibly, it is the dynamics of these excitations which are responsible for the extremely slow relaxation times reported in Chapter 4 and also by several other groups, and for phenomena such as thermal history dependence of the TO resonant frequency and velocity hysteresis. It is difficult to imagine that a superfluid component can be responsible for some of the phenomena we observe, such as the extremely small 'critical velocity' and the peak in the dissipation at  $v^*$ .

On the other hand, I take very seriously the observation that the ratio

$$\left| \Delta Q^{-1} \right| / (\Delta f^{max} / f_0)$$

can vary by two orders of magnitude from experiment to experiment, and that in several cases the frequency shift is far too large to be explained by the magnitude of the dissipation, a prediction common to several simple models of the rotational susceptibility of the TO-solid  $^4\text{He}$  system. This suggests to me that there is another degree of freedom in the solid, in addition to those associated with the excitations, that can effect a frequency shift with no accompanying dissipation; one interpretation is that this degree of freedom represents a superfluid component, perhaps of the Andreev-Lifshitz-Chester type. In this model,  $T^*$  and  $v^*$  are characteristic of the excitations, but also mark the onset of superfluidity, and therefore one would have to conclude that the excitations somehow *control* the global phase coherence of the superfluid component. The dependence of  $\left| \Delta Q^{-1} \right| / (\Delta f^{max} / f_0)$  on other variables relevant to the TO experiments (such as the frequency or pressure/molar volume) is not well known and I would encourage a more systematic treatment of this quantity.

The model I suggest above, wherein an unspecified ensemble of excitations undergoes a freeze-out at low temperature and controls the superfluid stiffness, is intentionally formulated quite generally. Despite the many numerical simulations that have studied the interplay of superfluidity and disorder in solid  $^4\text{He}$ , we really do not know enough experimentally about this interplay to make any definite conclusions about how these excitations, related to the disorder in the solid, control the superfluid stiffness. It is very possible that Anderson's vortex fluid model captures all of the relevant physics of the TO experiments, but in its current qualitative form it is difficult to make any comparison with experiment. Other, more quantitative models have admirably attempted to fit the TO frequency shift and dissipation, but they all seem to suffer from either (a) a lack of specificity about the microscopic mechanism, or (b) inconsistency with one or more of the myriad experimental variations of the TO experiments. Simply because of the number of variables that seem to affect the behavior of solid  $^4\text{He}$  in a TO, a single model that can describe the TO data appears to be a long way off, until we learn how to make samples with reproducible frequency shifts and dissipation peaks, or at least a reproducible ratio  $|\Delta Q^{-1}| / (\Delta f^{max} / f_0)$ .

I believe that the current evidence for a superfluid component that *partially* describes the TO results is good enough that we should continue to pursue experiments that look specifically for evidence of superfluidity, such as quantized vorticity or persistent currents. In light of the large variability of the TO experiments from sample to sample, I also believe that the aim of future experiments using TOs should be to incorporate a secondary experimental probe, e.g. in Sec. 6.3.2, so that multiple pieces of information about a single sample can be correlated. As shown by the number of careful yet sometimes seemingly contradictory experiments from 2004 up to the present, the solution to the supersolid

problem is unlikely to be solved by a single definitive experiment.

## APPENDIX A

### OPERATION OF DILUTION REFRIGERATOR IN CLARK A17

In this Appendix, I discuss some particulars of the operation of the Janis dilution refrigerator (JDR-100) currently installed in Clark A17.

#### A.1 Common Problems

We ran into a few common problems with the DR over the two years during which the experiments described in this dissertation were performed. The first was the gradual plugging of the condenser line, which we attributed to oil from the pump getting through both traps. Before finally warming up to  $\sim 100\text{K}$  and vigorously cryopumping the return line and condenser line, we managed to run the refrigerator at a return pressure of about 700 mbar (when the refrigerator worked ideally the return pressure was closer to 200-250 mbar). The main problem with running the DR with such a high return pressure was the large heat load presented to the pot by trying to recondense the  $^3\text{He}$  at too high a pressure, which precluded attaining the lowest temperatures, but this can work in a pinch. In the future, it might be advantageous to replace the rotary vane pump with an oil-free pump such as a scroll pump or a turbo pump backed by a scroll pump.

The second problem was that we believed we were losing mixture, likely  $^3\text{He}$  through a room temperature leak, and we blamed a large number of other problems on this (e.g. a higher base temperature). It was proposed that perhaps this mysterious “room temperature leak” was due to the return pressure/pump back pressure being momentarily higher than the 1 bar trigger level of the emer-

gency valve, which in the olden days would have blown the shaft seals on the rotary pump [100]. However, the magnetically-coupled motor on the rotary vane pump should not suffer from this problem, since it no longer relies on shaft seals. I am not completely convinced that this “leak” was actually to blame for all problems, nor do I believe it had anything to do with blowing the emergency valve (Fig. 2.3), but we did find one major leak in the shaft seals of the large gate valve on the still line. What I do know is that on several occasions all problems were fixed by warming up to room temperature, pumping all of the mixture back to the kegs, resetting the mixture so that it matched the ratio in the large H13 storage keg (nominally 22.9%  $^3\text{He}$ ) and adjusting the keg pressure so that the total pressure in the kegs and in the back of the circulation pump / return line was about 900 mbar (-10 kPa).

## A.2 Starting the Dilution Refrigerator

Here I report the best way to start our dilution refrigerator, in my experience.

1. Set the keg mash to approximately 23%  $^3\text{He}$  and 900 mbar or greater (-10 kPa on DG3/4), including the volume of the pump and the nitrogen cold trap. Wash it pretty well; the amount of time depends on how dirty you think the keg is, but a few hours is a good rule.
2. Turn on the 1K pot.
3. Open the kegs to the *condenser* side of the DR through both cold traps (usually through V6-5-12-16-21), keeping the circulation pump out of the circuit (i.e. keep V11 and V15 closed). The gate valve on top of the cryostat should be open, but the main gate valve before the pump should be

closed. If you have pumped out the still line previously, you can do the 4K condenser impedance test (the still pressure should rise 1 mbar in 30 seconds). Go home and sleep and let the kegs condense.<sup>1</sup>

4. When you come in 12 hours later, the keg pressure should be between -70 and -60 kPa and the still should have cooled to somewhere around 2.1-2.5 K. If the mash doesn't really condense (it stays between -30 and -20 kPa) and the still stays warm (~3-4 K), there is probably a heat leak to 4 K somewhere - possibly the VC needs pumping out.
5. Close off the kegs, for now: close V12.
6. Start circulating, very gently! Open the back of the pump to the condenser (open V11 and V15). Open the still line bypass valves *very slowly* and try to regulate the return pressure (DG2) to a value between -50 and -30 kPa. If you can manage to get the return pressure stable (or rising/falling slowly), you are in good shape. The still will cool slowly, and when the still temperature reaches around 1K, the digital still gauge will come on scale and the still pressure will be <100 mbar. At this point you can open the bypass valve more aggressively and within a few minutes you can open the main gate valve.
7. In step #6, a few things can go wrong. First, you might open the bypass valves too quickly and the return pressure might increase so that its trajectory exceeds 1 bar. The two options are (a) to close the bypasses, which is annoying because you'll have to open them slowly and incrementally again, or (b), a better option, to relieve some of the return pressure by opening V18 momentarily to the kegs. The second common thing to go

---

<sup>1</sup>Several reliable sources, such as [100], advise condensing the mash into the still side of the DR, with the added advantage that if there is any garbage left in the mash it will plate out on the walls of the still pipe. This method has never worked for me.

wrong is that the heat load to the pot is too large and you empty it. In this case, just stop pumping on the still and wait until the pot refills - it will probably take a few hours.

8. Hopefully at this point the DR will cool to its base temperature, usually between 10 and 20 mK as measured by thermometer #6. I have found the DR cools to its base temperature with as much as 200 mbar (-80 kPa) of mash left uncondensed in the keg, but if you find that the DR is not getting as low as about 10 or 20 mK, you can try condensing the rest of this mash by opening the kegs directly to the front of the circulation pump (i.e. through V6-3). Heating the still with 1 or 2 mW increases the circulation rate and can lower the base temperature as well; expect the still temperature to increase from about 0.65 to 0.85 K and the still pressure to increase from 0.15 mbar to 0.22 mbar with 2 mW heat.

### **A.3 Throughput Tests of the Condenser Impedance**

To perform the throughput tests of the condenser impedance, it is better to pump out the still line and test the flow of the mixture into the fridge (in the normal direction of circulation). The alternative is to pump out a volume around DG2 and measure the impedance of the flow in the opposite sense of the circulation, but since the still pressure gauge is much more sensitive, the first method works better. The starting pressure in front of the condenser can be anywhere from 300 to 900 mbar. The following numbers are good indicators of an unblocked impedance.

**Table A.1: Condenser impedance at various temperatures.**

Temperature (K)	Still pressure rate of change $dP_{still}/dt$
300	1 mbar / 1 hr
77	1 mbar / 8 min
4*	1 mbar / 30 sec

\* This indicates the impedance of the condenser immediately after the 1 K pot has been turned on and you are ready to start condensing the mixture as outlined in Sec. A.2.

## BIBLIOGRAPHY

- [1] M. A. Adams, J. Mayers, O. Kirichek, and R. B. E. Down. Measurement of the kinetic energy and lattice constant in hcp solid helium at temperatures 0.07–0.4 K. *Physical Review Letters*, 98(8):085301, 2007.
- [2] J. F. Allen and A. D. Misener. Flow of liquid helium ii. *Nature*, 141:75, 1938.
- [3] Vinay Ambegaokar, B. I. Halperin, David R. Nelson, and Eric D. Siggia. Dissipation in two-dimensional superfluids. *Phys. Rev. Lett.*, 40(12):783–786, Mar 1978.
- [4] Vinay Ambegaokar, B. I. Halperin, David R. Nelson, and Eric D. Siggia. Dynamics of superfluid films. *Phys. Rev. B*, 21(5):1806–1826, Mar 1980.
- [5] P. W. Anderson. personal communication.
- [6] P. W. Anderson. Considerations on the flow of superfluid helium. *Rev. Mod. Phys.*, 38(2):298–310, Apr 1966.
- [7] P. W. Anderson. Two new vortex liquids. *Nat Phys*, 3(3):160–162, 03 2007/03//print.
- [8] P. W. Anderson. Bose fluids above  $t_c$ : Incompressible vortex fluids and “supersolidity”. *Physical Review Letters*, 100(21):215301, 2008.
- [9] P. W. Anderson. A gross-pitaevskii treatment for supersolid helium. *Science*, 324(5927):631–632, 5 2009/5/1.
- [10] P. W. Anderson, B. L. Halperin, and C. M. Varma. Anomalous low-temperature thermal properties of glasses and spin glasses. *Phil. Mag.*, 25:1, 1972.
- [11] A. F. Andreev and I. M. Lifshitz. Quantum theory of defects in crystals. *Soviet Physics JETP-USSR*, 29(6):1107, 1969.
- [12] E. L. Andronikashvili. *Zh. Eksp. Teor. Fiz.*, 16:780, 1946.
- [13] James F. Annett. *Superconductivity, Superfluids and Condensates*. Oxford, oxford master series in condensed matter physics edition, 2004.

- [14] Y. Aoki, J. C. Graves, and H. Kojima. Oscillation frequency dependence of nonclassical rotation inertia of solid <sup>4</sup>He. *Physical Review Letters*, 99(1):015301, 2007.
- [15] Y. Aoki, M. C. Keiderling, and H. Kojima. New dissipation relaxation phenomenon in oscillating solid <sup>4</sup>He. *Physical Review Letters*, 100(21):215303, 2008.
- [16] N. W. Ashcroft and N. D. Mermin. *Solid State Physics*. Harcourt, Brace and Co., 1976.
- [17] A. V. Balatsky. personal communication.
- [18] A. V. Balatsky, M. J. Graf, Z. Nussinov, and S. A. Trugman. Entropy of solid <sup>4</sup>He: The possible role of a dislocation-induced glass. *Physical Review B (Condensed Matter and Materials Physics)*, 75(9):094201, 2007.
- [19] S. Balibar and F. Caupin. Supersolidity and disorder. *Journal of Physics: Condensed Matter*, 20(173201):1–19, 2008.
- [20] John Beamish. personal communication.
- [21] J. E. Berthold, D. J. Bishop, and J. D. Reppy. Superfluid transition of he-4 films adsorbed on porous vycor glass. *Phys. Rev. Lett.*, 39(6):348–352, Aug 1977.
- [22] Giulio Biroli, Claudio Chamon, and Francesco Zamponi. Theory of the superglass phase. *Physical Review B (Condensed Matter and Materials Physics)*, 78(22):224306, 2008.
- [23] D. J. Bishop, J. E. Berthold, J. M. Parpia, and J. D. Reppy. Superfluid density of thin he-4 films adsorbed in porous vycor glass. *Phys. Rev. B*, 24(9):5047–5057, Nov 1981.
- [24] D. J. Bishop, M. A. Paalanen, and J. D. Reppy. Search for superfluidity in hcp <sup>4</sup>He. *Physical Review B (Condensed Matter)*, 24(5):2844–2845, 1981.
- [25] D. J. Bishop and J. D. Reppy. Study of the superfluid transition in two-dimensional he4 films. *Phys. Rev. Lett.*, 40(26):1727–1730, Jun 1978.
- [26] D. J. Bishop and J. D. Reppy. Study of the superfluid transition in two-dimensional he4 films. *Phys. Rev. B*, 22(11):5171–5185, Dec 1980.

- [27] R. Bohmer, K. L. Ngai, C. A. Angell, and D. J. Plazek. Nonexponential relaxations in strong and fragile glass formers. *The Journal of Chemical Physics*, 99(5):4201–4209, 1993.
- [28] M. Boninsegni, A. B. Kuklov, L. Pollet, N. V. Prokof'ev, B. V. Svistunov, and M. Troyer. Luttinger liquid in the core of a screw dislocation in helium-4. *Physical Review Letters*, 99(3):035301, 2007.
- [29] Massimo Boninsegni, Nikolay Prokof'ev, and Boris Svistunov. Superglass phase of [sup 4]he. *Physical Review Letters*, 96(10):105301, 2006.
- [30] C. A. Burns and E. D. Isaacs. Debye-waller factor in solid 4 he crystals. *Phys. Rev. B*, 55(9):5767–5771, Mar 1997.
- [31] C. A. Burns, N. Mulders, L. Lurio, M. H. W. Chan, A. Said, C. N. Kodituwakku, and P. M. Platzman. X-ray studies of low-temperature solid [sup 4]he. *Physical Review B (Condensed Matter and Materials Physics)*, 78(22):224305, 2008.
- [32] D. M. Ceperley. Path integrals in the theory of condensed helium. *Rev. Mod. Phys.*, 67(2):279–355, Apr 1995.
- [33] E. Cheng, Milton W. Cole, W. F. Saam, and J. Treiner. Helium prewetting and nonwetting on weak-binding substrates. *Phys. Rev. Lett.*, 67(8):1007–1010, Aug 1991.
- [34] G. V. Chester. Speculations on bose-einstein condensation and quantum crystals. *Phys. Rev. A*, 2(1):256–258, Jul 1970.
- [35] A. C. Clark, J. D. Maynard, and M. H. W. Chan. Thermal history of solid he-4 under oscillation. *Physical Review B (Condensed Matter and Materials Physics)*, 77(18):184513, 2008.
- [36] A. C. Clark, J. T. West, and M. H. W. Chan. Nonclassical rotational inertia in helium crystals. *Physical Review Letters*, 99(13):135302, 2007.
- [37] J. Clarke and A. Braginski, editors. *The SQUID Handbook, vol. 1*, volume 1. Wiley-VCH, 2004.
- [38] Kenneth S. Cole and Robert H. Cole. Dispersion and absorption in dielectrics i. alternating current characteristics. *The Journal of Chemical Physics*, 9(4):341–351, 1941.

- [39] R. H. Crepeau, O. Heybey, D. M. Lee, and Stanley A. Strauss. Sound propagation in hcp solid helium crystals of known orientation. *Phys. Rev. A*, 3(3):1162–1174, Mar 1971.
- [40] D. W. Davidson and R. H. Cole. Dielectric relaxation in glycerol, propylene glycol, and n-propanol. *The Journal of Chemical Physics*, 19(12):1484–1490, 1951.
- [41] J. C. Davis, J. Steinhauer, K. Schwab, Yu. M. Mukharsky, A. Amar, Y. Sasaki, and R. E. Packard. Evidence for quantum tunneling of phase-slip vortices in superfluid *he*<sub>4</sub>. *Phys. Rev. Lett.*, 69(2):323–326, Jul 1992.
- [42] James Day and John Beamish. Pressure-driven flow of solid helium. *Physical Review Letters*, 96(10):105304, 2006.
- [43] James Day and John Beamish. Low-temperature shear modulus changes in solid *4he* and connection to supersolidity. *Nature*, 450(7171):853–856, 12 2007/12/06/print.
- [44] Pablo G. Debenedetti and Frank H. Stillinger. Supercooled liquids and the glass transition. *Nature*, 410(6825):259–267, 03 2001/03/08/print.
- [45] S. O. Diallo, J. V. Pearce, R. T. Azuah, O. Kirichek, J. W. Taylor, and H. R. Glyde. Bose-einstein condensation in solid *he*-4. *Physical Review Letters*, 98(20):205301, 2007.
- [46] R. J. Donnelly, R. A. Riegelmann, and C. F. Barenghi. The observed properties of liquid helium at the saturated vapor pressure. 1992.
- [47] Alan T. Dorsey, Paul M. Goldbart, and John Toner. Squeezing superfluid from a stone: Coupling superfluidity and elasticity in a supersolid. *Physical Review Letters*, 96(5):055301, 2006.
- [48] V. J. Emery and S. A. Kivelson. Importance of phase fluctuations in superconductors with small superfluid density. *Nature*, 374(6521):434–437, 03 1995/03/30/print.
- [49] A. Fefferman. *The Low Temperature Acoustic Properties of Amorphous Silica and Polycrystalline Aluminum*. PhD thesis, Cornell University, 2009.
- [50] J.P. Franck. Specific heat of solid *he*-4. *Physics Letters*, 11(3):208 – 210, 1964.

- [51] M. J. Graf, Z. Nussinov, and A. V. Balatsky. The glassy response of solid  $^4\text{He}$  to torsional oscillations. *Journal of Low Temperature Physics*, (not yet published), 2009.
- [52] Matthias Graf. Presentation at the aps march meeting. 2009.
- [53] A. Granato and K. Lucke. Theory of mechanical damping due to dislocations. *Journal of Applied Physics*, 27(6):583–593, 1956.
- [54] D. S. Greywall. Sound propagation in x-ray-oriented single crystals of hcp helium-4 and bcc helium-3. *Phys. Rev. A*, 3(6):2106–2121, Jun 1971.
- [55] A. Griffin. *Excitations in a Bose-Condensed Liquid*. Cambridge University Press, England, 1993.
- [56] V. N. Grigor'ev, V. A. Maidanov, V. Yu. Rubanskii, S. P. Rubets, E. Ya. Rudavskii, A. S. Rybalko, Ye. V. Syrnikov, and V. A. Tikhii. Observation of a glassy phase of  $^4\text{He}$  in the region of supersolid effects. *Physical Review B (Condensed Matter and Materials Physics)*, 76(22):224524–6, 12 2007/12/01/.
- [57] L. G. Gunderson. *An Experiment to Detect the Supersolid Transition in Helium Four*. PhD thesis, Cornell University, 1995.
- [58] E. C. Heltemes and C. A. Swenson. Specific heat of solid  $^3\text{He}$ . *Phys. Rev. Lett.*, 7(10):363–365, Nov 1961.
- [59] O. W. Heybey and D. M. Lee. Optical birefringence and crystal growth of hexagonal-close-packed  $^4\text{He}$  from superfluid helium. *Phys. Rev. Lett.*, 19(3):106–108, Jul 1967.
- [60] E. Hoskinson, Y. Sato, I. Hahn, and R. E. Packard. Transition from phase slips to the josephson effect in a superfluid  $^4\text{He}$  weak link. *Nat Phys*, 2(1):23–26, 01 2006.
- [61] J. P. Hulin, D. D'Humieres, B. Perrin, and A. Libchaber. Critical velocities for superfluid-helium flow through a small hole. *Phys. Rev. A*, 9(2):885–892, Feb 1974.
- [62] B. Hunt, E. Pratt, V. Gadagkar, M. Yamashita, A. V. Balatsky, and J. C. Davis. Evidence for a Superglass State in Solid  $^4\text{He}$ . *Science*, 324(5927):632–636, 2009.

- [63] B. Hunt, E. Pratt, V. Gadagkar, M. Yamashita, and J. C. Davis. *unpublished results*.
- [64] B. Hunt, M. Yamashita, J. A. Hoffmann, C. T. Black, and J. C. Davis. unpublished results.
- [65] David A. Huse and Zuhair U. Khandker. Dissipation peak as an indicator of inhomogeneity in solid [sup 4]he oscillator experiments. *Physical Review B (Condensed Matter and Materials Physics)*, 75(21):212504, 2007.
- [66] Izumi Iwasa and Hideji Suzuki. Sound velocity and attenuation in hcp he-4 crystals containing <sup>3</sup>he impurities. *Journal of the Physical Society of Japan*, 49(5):1722–1730, 1980.
- [67] Robert Jastrow. Many-body problem with strong forces. *Phys. Rev.*, 98(5):1479–1484, Jun 1955.
- [68] Pyotr Kapitza. Viscosity of liquid helium below the lambda-point. *Nature*, 141:74, 1938.
- [69] W. H. Keesom and K. W. Taconis. *Physica*, 5:161, 1938.
- [70] K. S. Ketola, S. Wang, and R. B. Hallock. Anomalous wetting of helium on cesium. *Phys. Rev. Lett.*, 68(2):201–204, Jan 1992.
- [71] E. Kim and M. H. W. Chan. Observation of Superflow in Solid Helium. *Science*, 305(5692):1941–1944, 2004.
- [72] E. Kim and M. H. W. Chan. Probable observation of a supersolid helium phase. *Nature*, 427(6971):225–227, 2004.
- [73] E. Kim and M. H. W. Chan. *Journal of Low Temperature Physics*, 138:859, 2005.
- [74] E. Kim and M. H. W. Chan. Supersolid helium at high pressure. *Physical Review Letters*, 97(11):115302, 2006.
- [75] E. Kim, J. S. Xia, J. T. West, X. Lin, A. C. Clark, and M. H. W. Chan. Effect of he-3 impurities on the nonclassical response to oscillation of solid he-4. *Physical Review Letters*, 100(6):065301, 2008.

- [76] J. Klier, P. Stefanyi, and A. F. G. Wyatt. Contact angle of liquid he-4 on a cs surface. *Phys. Rev. Lett.*, 75(20):3709–3712, Nov 1995.
- [77] L. D. Landau. *J. Phys. USSR*, 5:71, 1941.
- [78] A. J. Leggett. Can a solid be "superfluid"? *Phys. Rev. Lett.*, 25(22):1543–1546, Nov 1970.
- [79] Cao Lie-zhao, D. F. Brewer, C. Girit, E. N. Smith, and J. D. Reppy. Flow and torsional oscillator measurements on liquid helium in restricted geometries under pressure. *Phys. Rev. B*, 33(1):106–117, Jan 1986.
- [80] X. Lin, A. C. Clark, and M. H. W. Chan. Probable heat capacity signature of the supersolid transition. *Nature*, 449(7165):1025–1028, 2007.
- [81] X. Lin, A. C. Clark, Z. G. Cheng, and M. H. W. Chan. Heat capacity peak in solid [<sup>4</sup>he]: Effects of disorder and [<sup>3</sup>he] impurities. *Physical Review Letters*, 102(12):125302, 2009.
- [82] F. London. *Superfluids*, volume 2. Wiley, 1954.
- [83] Fritz London. The lambda-phenomenon of liquid helium and the bose-einstein degeneracy. *Nature*, 141:643–644, 1938.
- [84] Mark W. Meisel. Supersolid 4he: an overview of past searches and future possibilities. *Physica B: Condensed Matter*, 178(1-4):121 – 128, 1992. Proceedings of the Korber Symposium on Superfluid 3He in Rotation.
- [85] N. Mulders, J. T. West, M. H. W. Chan, C. N. Koditwakku, C. A. Burns, and L. B. Lurio. Torsional oscillator and synchrotron x-ray experiments on solid [<sup>4</sup>he] in aerogel. *Physical Review Letters*, 101(16):165303, 2008.
- [86] Z. Nussinov, A. V. Balatsky, M. J. Graf, and S. A. Trugman. Origin of the decrease in the torsional-oscillator period of solid [<sup>4</sup>he]. *Physical Review B (Condensed Matter and Materials Physics)*, 76(1):014530, 2007.
- [87] Ian K. Ono, Corey S. O'Hern, D. J. Durian, Stephen A. Langer, Andrea J. Liu, and Sidney R. Nagel. Effective temperatures of a driven system near jamming. *Phys. Rev. Lett.*, 89(9):095703, Aug 2002.
- [88] M. A. Paalanen, D. J. Bishop, and H. W. Dail. Dislocation motion in hcp [<sup>4</sup>he]. *Physical Review Letters*, 46(10):664–667, 1981.

- [89] H. J. Paik. Superconducting tunable-diaphragm transducer for sensitive acceleration measurements. *J. Appl. Phys.*, (47):1168, 1976.
- [90] J. M. Parpia and J. D. Reppy. Critical velocities in superfluid  $he3$ . *Phys. Rev. Lett.*, 43(18):1332–1336, Oct 1979.
- [91] Oliver Penrose and Lars Onsager. Bose-einstein condensation and liquid helium. *Phys. Rev.*, 104(3):576–584, Nov 1956.
- [92] S. V. Pereverzev, A. Loshak, S. Backhaus, J. C. Davis, and R. E. Packard. Quantum oscillations between two weakly coupled reservoirs of superfluid  $3he$ . *Nature*, 388(6641):449–451, 07 1997.
- [93] W. A. Phillips. Tunneling states in amorphous solids. *J. Low Temp. Phys.*, 7:351, 1972.
- [94] F. Pobell. *Matter and Methods at Low Temperatures*. Springer, 2nd edition, 1996.
- [95] L. Pollet, M. Boninsegni, A. B. Kuklov, N. V. Prokof'ev, B. V. Svistunov, and M. Troyer. Superfluidity of grain boundaries in solid  $[sup 4]he$ . *Physical Review Letters*, 98(13):135301, 2007.
- [96] L. Pollet, M. Boninsegni, A. B. Kuklov, N. V. Prokof'ev, B. V. Svistunov, and M. Troyer. Local stress and superfluid properties of solid  $[sup 4]he$ . *Physical Review Letters*, 101(9):097202, 2008.
- [97] M. W. Ray and R. B. Hallock. Observation of unusual mass transport in solid hcp  $[sup 4]he$ . *Physical Review Letters*, 100(23):235301–4, 06 2008/06/13/.
- [98] L. Reatto. Bose-einstein condensation for a class of wave functions. *Phys. Rev.*, 183(1):334–338, Jul 1969.
- [99] John Reppy. *personal communication*.
- [100] Robert C. Richardson and Eric N. Smith, editors. *Experimental Techniques in Condensed Matter Physics at Low Temperatures*. Addison-Wesley, 1998.
- [101] Ann Sophie C. Rittner and John D. Reppy. Observation of classical rotational inertia and nonclassical supersolid signals in solid  $[sup 4]he$  below 250 mk. *Physical Review Letters*, 97(16):165301, 2006.

- [102] Ann Sophie C. Rittner and John D. Reppy. Disorder and the supersolid state of solid [<sup>4</sup>He]. *Physical Review Letters*, 98(17):175302, 2007.
- [103] Ann Sophie C. Rittner and John D. Reppy. Probing the upper limit of nonclassical rotational inertia in solid helium 4. *Physical Review Letters*, 101(15):155301, 2008.
- [104] D. Rosenberg, P. Nalbach, and D. D. Osheroff. Memory effects in amorphous solids below 20 mk. *Phys. Rev. Lett.*, 90(19):195501, May 2003.
- [105] S. Sasaki, R. Ishiguro, F. Caupin, H. J. Maris, and S. Balibar. Superfluidity of Grain Boundaries and Supersolid Behavior. *Science*, 313(5790):1098–1100, 2006.
- [106] Wayne M. Saslow. On superflow in solid *he4*. *Phys. Rev. B*, 71(9):092502, Mar 2005.
- [107] A. F. Schuch and R. L. Mills. Structure of the  $\gamma$  form of solid *he4*. *Phys. Rev. Lett.*, 8(12):469–470, Jun 1962.
- [108] A. F. Schuch and R. L. Mills. Structure of the  $\gamma$  form of solid *he4*. *Phys. Rev. Lett.*, 8(12):469–470, Jun 1962.
- [109] S. I. Shevchenko. *Soviet Journal of Low Temperature Physics*, 13:61, 1987.
- [110] Frank H. Stillinger. A topographic view of supercooled liquids and glass formation. *Science*, 267(5206):1935–1939, 3 1995/3/31.
- [111] G. C. Straty and E. D. Adams. Highly sensitive capacitive pressure gauge. *Review of Scientific Instruments*, 40(11):1393–1397, 1969.
- [112] D.R. Tilley and J. Tilley. *Superfluidity and Superconductivity*. Taylor and Francis, 1 edition, 1990.
- [113] L. Tisza. Transport phenomena in helium ii. *Nature*, 141:913, 1938.
- [114] I. A. Todoshchenko, H. Alles, J. Bueno, H. J. Junes, A. Ya. Parshin, and V. Tsepelin. Melting curve of [<sup>4</sup>He]: No sign of a supersolid transition down to 10 mk. *Physical Review Letters*, 97(16):165302, 2006.
- [115] John Toner. Quenched dislocation enhanced supersolid ordering. *Physical Review Letters*, 100(3):035302, 2008.

- [116] E. Varoquaux, W. Zimmerman Jr., and O. Avenel. *Excitations in Two-Dimensional and Three-Dimensional Quantum Fluids*. Plenum Press, 1991.
- [117] Yayu Wang, Lu Li, and N. P. Ong. Nernst effect in high- $T_c$  superconductors. *Physical Review B (Condensed Matter and Materials Physics)*, 73(2):024510, 2006.
- [118] R. Wanner and J. P. Franck. Volume dependence of the longitudinal sound velocity in hcp  $^4\text{He}$  single crystals. *Phys. Rev. Lett.*, 24(8):365–367, Feb 1970.
- [119] F. J. Webb, K. R. Wilkinson, and J. Wilks. *Proc. R. Soc. A*, 214:546, 1952.
- [120] J. T. West, X. Lin, Z. G. Cheng, and M. H. W. Chan. Supersolid behavior in confined geometry. *Physical Review Letters*, 102(18):185302, 2009.
- [121] J. Wilks. *The Properties of Liquid and Solid Helium*. Clarendon Press, Oxford, UK, 1967.
- [122] Jiansheng Wu and Philip Phillips. Minimal model for disorder-induced missing moment of inertia in solid  $^4\text{He}$ . *Physical Review B (Condensed Matter and Materials Physics)*, 78(1):014515, 2008.
- [123] K. Yamamoto, H. Nakashima, Y. Shibayama, and K. Shirahama. Anomalous suppression of superfluidity in  $^4\text{He}$  confined in a nanoporous glass. *Physical Review Letters*, 93(7):075302, 2004.
- [124] J. L. Yntema and W. G. Schneider. Compressibility of gases at high temperatures. iii. the second virial coefficient of helium in the temperature range 600[degree]c to 1200[degree]c. *The Journal of Chemical Physics*, 18(5):641–646, 1950.
- [125] C.-D. Yoo and Alan T. Dorsey. Theory of viscoelastic behavior of solid  $^4\text{He}$ . *Physical Review B (Condensed Matter and Materials Physics)*, 79(10):100504, 2009.
- [126] R. C. Zeller and R. O. Pohl. Thermal conductivity and specific heat of noncrystalline solids. *Phys. Rev. B*, 4(6):2029–2041, Sep 1971.